Discrete Element Modelling of packed rock beds for thermal storage applications

by

Rick Guillaume Nel
15033406

Thesis presented in partial fulfilment of the requirements for the degree of Master of Science in Mechanical Engineering in the Faculty of Engineering at Stellenbosch University

Department of Mechanical and Mechatronic Engineering,
University of Stellenbosch,
Private Bag X1, Matieland 7602, South Africa.

Supervisor: Dr. C. Coetzee

March 2013

Declaration

By submitting this thesis electronically, I declare that the entirety of the work contained therein is my own, original work, that I am the sole author thereof (save to the extent explicitly otherwise stated), that reproduction and publication thereof by Stellenbosch University will not infringe any third party rights and that I have not previously in its entirety or in part submitted it for obtaining any qualification.

Date: .....

Abstract

Discrete Element Modelling of packed rock beds for thermal storage applications

R.G. Nel

Department of Mechanical and Mechatronic Engineering,
University of Stellenbosch,
Private Bag X1, Matieland 7602, South Africa.

Thesis: MScEng (Mech)

March 2013

The increased necessity to obtain power from other sources than conventional fossil fuels has led to the growing interest in solar power. The problem with the proposed technology is that it can only provide power during the day and therefore requires some sort of storage system, if power is to be supplied throughout the day and night. A number of storage systems exist, but the one of particular interest for this research, is packed rock beds. Rock beds have the advantage that if designed right, they have the potential to be one of the most cost effective means of storing thermal energy for solar power plants. Discrete Element Models (DEM) of rock beds were therefore developed through both experimental and numerical procedures, by conducting a series of sensitivity, calibration and verification studies.

The developed models were then used to study various aspects associated with rock beds, which were either too impractical, impossible or too expensive to conduct through actual experimental work. This research focused specifically on the potential of constructing self-supporting tunnels within the rock beds in order to improve the air flow uniformity through the bed, while minimizing the pressure drop. It was observed that if the appropriate steps were followed, stable self-supporting tunnels could be formed. Valuable information such as the rock orientations resulting from different packing directions could also be

derived from the models and finally, a method to convert the DEM models into the appropriate format such that it could be imported into a CFD preprocessor for future CFD studies, was developed.

Uittreksel

Diskreet Element Modellering van verpakte klip beddens vir termiese storings toepassings

("Discrete Element Modelling of packed rock beds for thermal storage applications")

R.G. Nel

Departement Meganiese en Megatroniese Ingenieurswese,
Universiteit van Stellenbosch,
Privaatsak X1, Matieland 7602, Suid Afrika.

Tesis: MScIng (Meg)

Maart 2013

Die verhoogde noodsaaklikheid om energie te verkry uit ander bronne as konvensionele fossielbrandstowwe, het gelei tot die groeiende belangstelling in sonkrag energie. Die probleem met die voorgestelde tegnologie is dat dit net energie gedurende die dag kan voorsien en dus word daar 'n stoorstelsel benodig indien energie deur beide die dag en nag voorsien moet word. Tans bestaan daar wel 'n aantal van hierdie stoorstelsels, maar die een wat van besondere belang is in hierdie navorsing, is verpakte klip beddens. Klip beddens het die voordeel dat, indien dit reg ontwerp is, dit oor die potensiaal beskik om een van die mees koste-doeltreffende middels te wees vir die stoor van termiese energie vir sonkragstasies. Diskreet Element Modelle (DEM) van die klip beddens is ontwikkel deur gebruik te maak van beide experimentele en numeriese metodes waartydens 'n reeks sensitiwiteits-, kalibrasie- en verifiëring studies uitgevoer is.

Die ontwikkelde modelle is gebruik om verskeie aspekte van klip beddens te ondersoek, wat of te onprakties, onmoontlik of te duur is vanuit 'n eksperimentele oogpunt. Hierdie navorsing het spesifiek gefokus op die potensiaal om self-ondersteunende tonnels binne in die klip beddens te vorm, ten einde die

egaligheid van die lugvloei deur die bed te verbeter, terwyl die drukval geminimeer word. Daar is waargeneem dat stabiele self-ondersteunende tonnels wel gevorm kon word indien die toepaslike stappe gevolg is. Waardevolle inligting soos die klip oriëntasies wat as gevolg van die verskillende verpakkings rigtings onstaan kon ook vanuit die model verkry word. Ten slotte is 'n metode ontwikkel om die DEM modelle na die toepaslike formaat te omskep sodat dit ten einde gebruik kan word in numeriese vloeidinamika studies.

Dedications

I would like to thank the following people in particular for their input:

Dr. Corné Coetzee for his guidance, helpful advice and patience throughout this project.

My parents for their support and the opportunities they have given me.

My friends for all their support and who made my time at Stellenbosch unforgettable.

Mieke Louw, for all her support, encouragement and love.

Contents

List of Figures

List of Tables

Nomenclature

A_{cct}	Cross sectional area of confined compression test	$[\mathrm{m}^2]$
D	Tube diameter used to describe Janssen's theory	$[\mathrm{m}]$
E	Young's modulus (Modulus of elasticity)	$[\mathrm{Pa}]$
E'	Confined Young's modulus	$[\mathrm{MPa}]$
E_r	Total relative error	$[-]$
e	Voids ratio	$[-]$
e_r	Relative error between experimental and numerical values	$[-]$
F	Normal load	$[\mathrm{N}]$
H	Container height used to describe Janssen's theory	$[\mathrm{m}]$
K	Janssen's constant	$[-]$
K_c	Geometric constant for modulus of elasticity calculation	$[-]$
k_b	Bulk stiffness	$[\mathrm{MN/m}]$
k_n	Normal stiffness	$[\mathrm{MN/m}]$
k_s	Shear stiffness	$[\mathrm{MN/m}]$
L	Packing height before compression	$[\mathrm{m}]$
L''	Packing height after from compression	$[\mathrm{m}]$
m_b	Bulk mass	$[\mathrm{kg}]$
m_p	Particle mass	$[\mathrm{kg}]$

P	Load applied during particle compression test	[N]
P_L	Lateral pressure	[Pa]
P_r	Radial pressure	[Pa]
P_{sat}	Saturation pressure	[Pa]
P_u	Pressure resulting from frictional forces	[Pa]
P_z	Vertical pressure	[Pa]
R_{max}	Maximum particle radius	[m]
R_{min}	Minimum particle radius	[m]
r_{ini}	Initial particle radius prior to thermal expansion	[m]
r_{new}	Modified particle radius resulting from thermal expansion	[m]
V_b	Bulk volume	[m^3]
V_{ini}	Initial particle volume prior to thermal expansion	[m^3]
V_{new}	Modified particle volume resulting from thermal expansion	[m^3]
V_p	Particle volume	[m^3]
V_v	Voids volume	[m^3]
XY	Final distance between centre points of reference spheres	[m]
XY_{ini}	Initial distance between centre points of reference spheres	[m]
z	Vertical coordinate	[m]
z_{sat}	Saturation depth	[m]

Greek letters

α	Angle of repose	[°]
α_p	Radii of curvature resulting from particle deformation	[m]
α_T	Thermal expansion coefficient	[1/°C]

ε_z	Vertical strain	$[-]$
ε_x	Lateral strain in x-direction	$[-]$
ε_y	Lateral stain in y-direction	$[-]$
η	Porosity	$[-]$
ρ_b	Bulk density	$[\mathrm{kg/m^3}]$
ρ_{liq}	Density of liquid	$[\mathrm{kg/m^3}]$
ρ_p	Particle density	$[\mathrm{kg/m^3}]$
σ_s	Shear stress	$[\mathrm{Pa}]$
σ_x	Normal stress	$[\mathrm{Pa}]$
σ_z	Vertical stress	$[\mathrm{Pa}]$
$\ominus_{ini}$	Initial relative angle between the two reference spheres	$[^\circ]$
$\ominus$	Final relative angle between the two reference spheres	$[^\circ]$
μ	Friction coefficient	$[-]$
μ_{pp}	Particle to particle friction coefficient	$[-]$
μ_{pw}	Particle to wall friction coefficient	$[-]$
ϕ	Internal friction angle	$[^\circ]$
υ	Particle's Poisson's ratio	$[-]$
γ	Base plate inclination angle	$[^\circ]$
ξ	Critical damping ratio	$[-]$
$\Delta\varepsilon_z$	Change in vertical strain	$[-]$
$\Delta\sigma_s$	Change in shear stress	$[-]$
$\Delta\sigma_x$	Change in normal stress	$[-]$
$\Delta\sigma_z$	Change in vertical stress	$[-]$

ΔT	Change in temperature	$[-]$

Subscripts and superscripts

BD	Bulk density	$[-]$
$CFBW$	Normal contact force on the bottom wall	$[-]$
$CFSW$	Normal contact force on the side walls	$[-]$

Abbreviations

API	Application Programming Interface
CFD	Computational Fluid Dynamics
COR	Coefficient of Restitution
DEM	Discrete Element Modelling
PPF	Particle to Particle Friction Coefficient
PPW	Particle to Wall Friction Coefficient
STERG	Solar Thermal Energy Research Group
SUNSPOT	Stellenbosch UNiversity Solar POwer Thermodynamic
CDR	Critical Damping Ratio

1. Introduction

The increased necessity to obtain power from other sources than conventional fossil fuels has led to the growing interest in solar power. Not only is this technology improving, but large scale solar thermal power plants are being built in a number of countries around the world. Unfortunately there are countries, such as South Africa, which has some of the highest irradiation levels in the world (Allen, 2010), but is still not using it to its fullest potential. The reason for this might be the fact that solar power plants have high capital cost and require large areas of land. It is therefore crucial to investigate methods to reduce these factors and one such method is the SUNSPOT (Stellenbosch UNiversity Solar POwer Thermodynamic) cycle.

1.1. Background

The SUNSPOT cycle (Figure 1.1) is a thermal power generating plant, which is being evaluated and developed by the Department of Mechanical and Mechatronic Engineering at the University of Stellenbosch. It was proposed by Professor Deltev Kröger in 2008, because it is an efficient and appropriate means of generating electricity in South Africa (Kröger, 2011).

The working principle of the SUNSPOT cycle is as follow. A heliostat or mirror field concentrates solar radiation onto a central receiver heat exchanger, where compressed ambient air is heated to over 800 °C. The hot air will then flow through a combustion chamber, where additional heat can be added if fluctuations in the solar radiation, occurs and then through a turbine which drives a compressor and a generator. The compressor compresses the ambient air flowing through the receiver, while the generator supplies electric energy to the transmission system or grid. The outlet air of the turbine, which is approximately at 500 °C (Allen, 2010), is then forced to flow through a thermal storage unit consisting out of a packed rock bed. During the night or cloudy conditions, when the solar radiation levels are too low to produce enough heat, cold ambient air is blown through the packed rock bed in order to heat the air.

This heated air then flows through a finned tube boiler, where it evaporates water in order to produce steam. The steam then flows through a steam turbine, which drives a second generator in order to supply the electric energy to the transmission system or grid. Finally the steam leaving the secondary turbine rejects its heat to the environment by condensing in a cooling system (Allen, 2010).

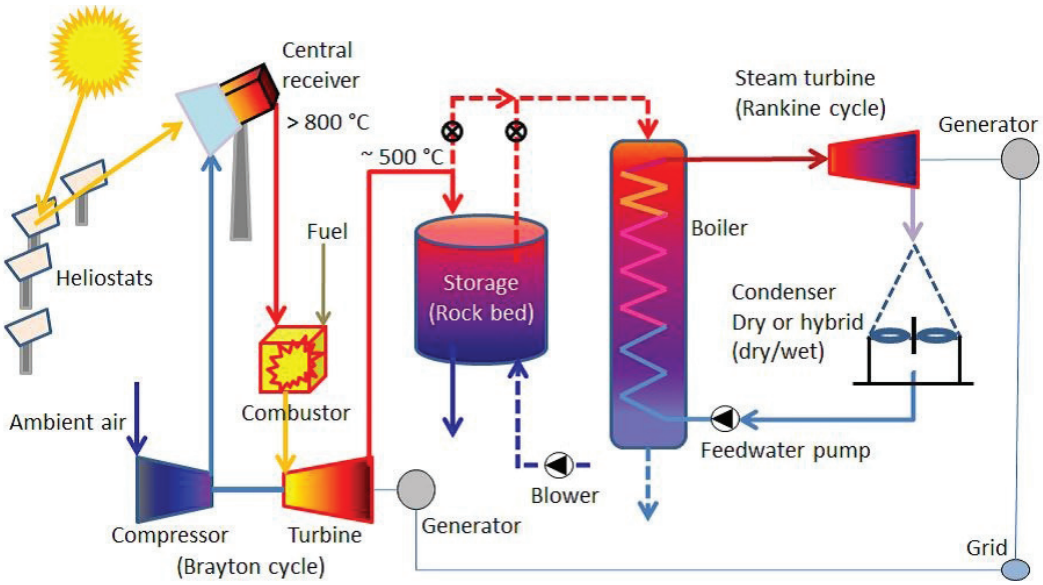

Figure 1.1: The SUNSPOT cycle (Allen, 2010)

Research on the SUNSPOT cycle is being done by the Solar Thermal Energy Research Group (STERG, 2012) and one of the primary research areas is the thermal storage unit. Although there are a number of other thermal storage possibilities, such as molten salts and various other phase change materials, they are usually relative expensive and have limited operating hours compared to large rock beds (Kröger, 2011). However, before any final decisions can be made with regard to the feasibility of using packed rock beds as a thermal storage medium for large scale applications, further research is still required, especially with respect to the pressure drop and air flow distribution through such large beds as well as the granular mechanics at both the bulk and particulate level and how they would affect the overall design of such a system.

1.2. Objectives and scope of this research

The main outcome of this study is to develop numerical models resembling packed rock beds and then to use these models to investigate various aspects associated with such rock beds, which are too impractical, impossible or too expensive to achieve through actual experimental work. The objectives of this research can therefore be summarized as follows:

- Develop numerical models of randomly packed beds consisting out of irregular shaped particles. Here it would be important to first understand how various factors influence the models and secondly the models would have to be verified to ensure their credibility.
- Investigate the possibility of constructing self-supporting tunnels within the rock beds, which could be used to improve the air flow distribution as well as reduce the pressure drop over the beds. For clarity, with self-supporting tunnels, it is implied that there will be no support structures or adhesive materials within the tunnel sections to prevent them from caving in and the only materials will be the rock particles themselves.
- Develop a means of converting the rock bed models into the appropriate geometric models such that they can be used for computational fluid dynamics studies (CFD). The CFD studies would not be considered in this thesis in that they form part of the research conducted by other members of the STERG. They will focus on the development of numeric pressure drop and heat transfer correlations. Any additional information, which would be required to conduct the CFD studies, such as the axial and/or radial porosity variations, for instance, should be identified and then derived from the developed rock bed models.
- Finally, investigate the random packing structure of a rock bed with specific reference to the orientation of the rock particles. The particle orientation influences the flow path of the air being pumped through the bed, which directly influences the pressure drop.

1.3. Motivation behind this research

Not only is it important to research into new thermal storage methods, but it is also crucial to investigate possible improvements in existing ones. The interest in packed rock beds as a thermal storage system has grown over the past few years and a great deal of experimental and theoretical research has

been done and is still being conducted in this area. However, there are still a number of aspects with respect to the operation and design of such systems, which requires further attention.

Two of these aspects, which are very important to the overall performance of the thermal storage system, are the pressure drop and air flow distribution through the rock bed. These two factors are dependent on one another in the sense that if the pressure drop is very low there is a good possibility that the flow distribution will be non-uniform. This would mean that some of the rocks may never come into contact with the hot air, which will result in a loss of storage capacity. On the other hand if the pressure drop is very high the flow distribution would most likely be uniform, but the large pressure drop will result in high operational costs due to the increased pumping power required to force the air through the bed (Hollands *et al.*, 1984).

According to the literature, little research has been done with regards to the flow distribution within packed beds, but there are numerous analytical models available to predict the pressure drop over such beds, of which some of the most common are the representative unit cell model (du Plessis and Woudberg, 2008) as well as the equations of Ergun (1952) and Singh *et al.* (2006). However, the use of CFD studies to analyze the flow distribution as well the pressure drop associated with packed beds has become more and more popular in the past few years. The only drawback is that most of these CFD studies only considered a small number of particles which were packed in structured manners such that they could easily be reconstructed in the CFD domain. If the interest therefore shifts to applications where large numbers of particles are randomly packed, such as in the thermal storage rock bed where it is impossible to directly measure the position of the rocks in order to create the CFD model, numerical methods such as the Discrete Element Method (DEM) could be incorporated. This coupled DEM-CFD approach has also been implemented by a number of researchers (Bai *et al.*, 2009; Eppinger *et al.*, 2011; Ookawara *et al.*, 2007) , but most of them focused on pure spherical beds. The literature contained very little research on coupled DEM-CFD models with irregular shaped particles.

Developing such models could therefore allow researchers to perform various new studies, which were previously too expensive, impractical or impossible to achieve through analytical or experimental methods. The numerical models therefore provide simulation tools which can be used to design, operate and improve packed bed storage systems, which is why the development and implementation of such models form the core of this thesis.

2. Literature review

2.1. Sensible heat storage in packed rock beds

There are three main types of thermal energy storage methods and they are sensible, latent and thermochemical heat storage. Unlike latent and thermochemical heat storage systems, where energy is stored or extracted by means of a phase change material or a chemical reaction respectively, sensible heat storage systems store or extract energy by heating or cooling a solid or liquid substance. There are a number of different substances, which can be used, but some of the most common are rock pebbles, refractory, water, molten salts and oils. The choice of substance depends mostly on the temperature level of the required application (Ataer, 2006), but the fact that this study is focused specifically on packed rock beds, means that only they will be considered further.

A typical packed bed storage system can either be designed for a horizontal or a vertical flow regime. In the case of a horizontal flow regime the storage system consists out of an insulated horizontal container, air inlet and outlet ports as well as loosely packed rock particles kept in place with the aid of vertical baffles and horizontal supports (Figure 2.1). The vertical baffles and horizontal supports not only help to create plenums on both ends, which help to distribute the flow over the bed faces, but also eliminate open channels at the top of the bed (SRCC, 2012). Unlike the vertical bed, the flow direction during the charging and discharging stages can be from any side as long as it is kept constant once it has been fixed.

In the case of a vertical flow regime (Figure 2.2) the storage system consists of an insulated container, loosely packed rock pebbles on top of a metal grate and an air inlet and outlet port. The metal grate is required to create a plenum underneath the rock bed, which is preferred to help distribute the flow over the bed face (SRCC, 2012). A plenum is also created at the top of the bed by simply elevating the roof section above the bed face.

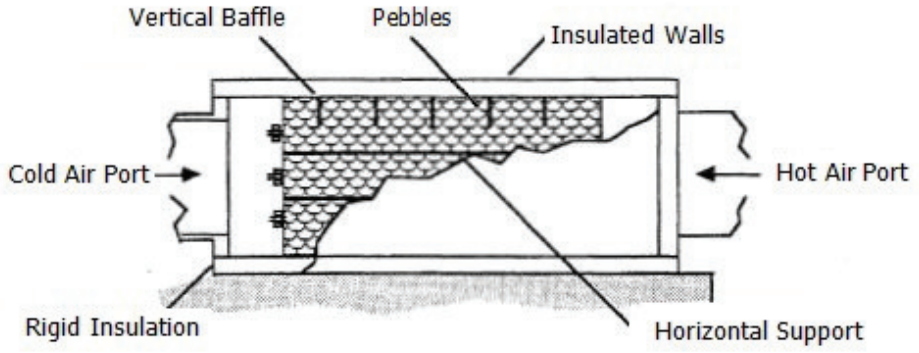

Figure 2.1: A typical horizontal rock bed system (SRCC, 2012)

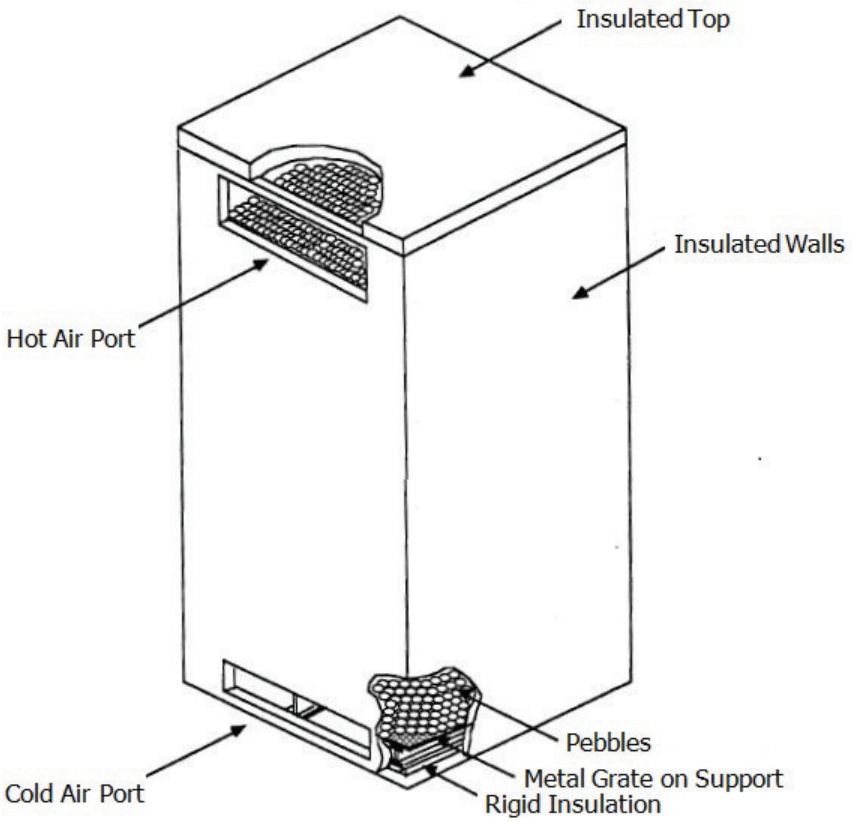

Figure 2.2: A typical vertical rock bed system (SRCC, 2012)

The flow direction during the charging stage is from top to bottom, where the warm air is introduced at the top and the cold air is removed from the bottom. The air will therefore transfer its heat to the rocks as it is forced downwards and will exit at more or less the same temperature as the rocks in the bottom layer of the bed. On the other hand, during the discharging stage the cold

air is introduced at the bottom of the bed and the hot air exits at the top at approximately the same temperature as the rocks in the top layer (Garg, 1987). These flow directions ensure that the forced and natural convection currents aid one another, such that a stable temperature distribution is achieved and that the natural convection currents do not de-stratify the bed. If the bed is de-stratified the instantaneous heat transfer rate between the rocks and the air will decrease, which results in an increase in the pumping power required to remove the same amount of heat from the bed as when compared to normal operating conditions (Allen, 2010).

The most economical and efficient particle size to use for sensible thermal storage systems is still subject to investigation, but according to studies done by Sanderson and Cunningham (1995*a*) a particle diameter greater than 13 mm should be used in order avoid high pumping power requirements due to excessive pressure losses. Similar results were obtained by Torab and Beasley (1987) who stated that a particle diameter larger than 12.7 mm should be used. However, the particles cannot be too large, since larger particles reduce the volumetric heat transfer coefficient as well as the amount of useful energy stored in the beds. This is due to better stratification occurring in beds with smaller particles, which result in a much steeper temperature wave (Figure 2.3) than what is found in beds with larger particles (Sanderson and Cunningham, 1995*b*).

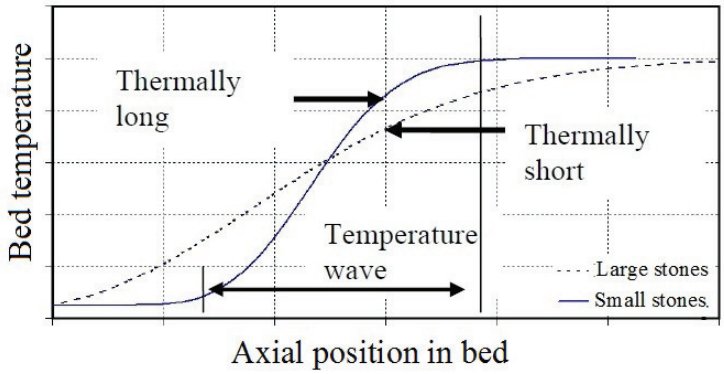

Figure 2.3: Effect of particle size on the absorption of heat within a packed bed (Sanderson and Cunningham, 1995*a*)

Another aspect which influences the amount of useful energy being stored in packed beds is the bed length and can be better understood through an explanation of thermally 'long' and thermally 'short' packings (Figure 2.3). The two differ in the sense that a thermally long packing can heat the medium to a constant temperature over time, since the bed length in the flow direction is sufficiently long, whereas in the case of a thermally short packing the temperature wave extends over the length of the bed reducing the temperature

to which the heat transfer fluid can be heated (Sanderson and Cunningham, 1995*a*).

A packed bed with large particles would therefore require longer bed lengths, for a given bed cross sectional area, compared to a bed with smaller particles. Allen (2010) obtained similar results in his study on the performance characteristics of packed bed thermal energy storage for solar thermal power plants. He estimated the required bed dimensions, suitable for the SUNSPOT concept, for three different rock sizes and these calculations were based on the following assumptions:

- An initial bed temperature of 25 °C
- A constant charging air temperature of the bed of 528 °C at the inlet
- A constant charging air mass flow rate of 300 kg/s
- Approximately 8 hours storage capacity

The final results are summarized in Table 2.1, which clearly shows the relation between the particle size and the required bed length. The table also gives an idea of the overall estimated rock bed size one can expect for a proposed solar power plant such as the SUNSPOT concept.

Table 2.1: Proposed packed bed dimensions based on a cross sectional area of 40 x 40 m (Allen, 2010)

Particle diameter (m)	**Required bed length (m)**	**Required bed volume (m^3)**
0.05	10.5	17,000
0.1	14.5	24,000
0.2	23	37,000

To conclude, some advantages and disadvantages of packed rock beds compared to other storage methods are as follow (Garg *et al.*, 1985).

Advantages:

- Higher storage zone temperatures can be achieved
- No heat exchangers are required
- Rocks are non-combustible, non-corrosive, non-toxic, easy to handle, abundant and have a low cost.
- The rocks act as both the storage medium and the heat transfer area

- Heat transfer rates between the air and the rocks are large due to the low effective heat conductance of the rock bed, the large heat transfer area and the small area of contact between the individual rocks.

Disadvantages:

- Require large storage volumes
- The system cannot charge and discharge at the same time
- Subject to a large pressure drop

2.2. Granular materials

Granular materials are simply large collections of discrete macroscopic particles, which can range from man-made objects such as pharmaceuticals (pills) to naturally formed materials such as seeds, rice, wheat, sand, rock pebbles and gravel. The particles making up a granular material are therefore large enough that they are ungoverned by temperature changes in the sense that they will not receive much kinetic energy when they are subject to a temperature increase. It is also possible to describe their motion by simply using classical physics instead of quantum physics, which are commonly used to describe the motion of atomic and subatomic particles. It is therefore relatively easy to predict and study the movement of individual particles within a granular material, once they are set in motion (Clark, 1999).

Granular materials also tend to respond in a unique manner when they are subjected to external forces in that their behaviour can resemble either one of the three states of matter (gas, liquid or solid). A granular material would for instance resemble a liquid when it is poured into a container, since it would flow under gravity. It would also resist a shear stress if it is confined within a container, unlike a liquid but similar to a solid and finally if a vibrational force is applied to a container filled with a granular material, the individual particles would move around and collide with one another, just as if it was a gas.

Another important aspect observed in granular materials is the formation of strong and weak force networks, which form due to the unique way in which forces are transmitted through a granular assembly. Figure 2.4 is a simple representation of a typical granular assembly and its resulting force network, which resulted either from an externally applied load or simply the weight of the individual particles. The interesting fact however, is that the majority

of the particles belong to weak networks, which carry loads much less than the average contact force within the assembly, whereas relatively few particles make up the strong networks. These strong networks, which are also called force chains are usually spatially distributed within the granular material and carry most of the load (Peters *et al.*, 2005).

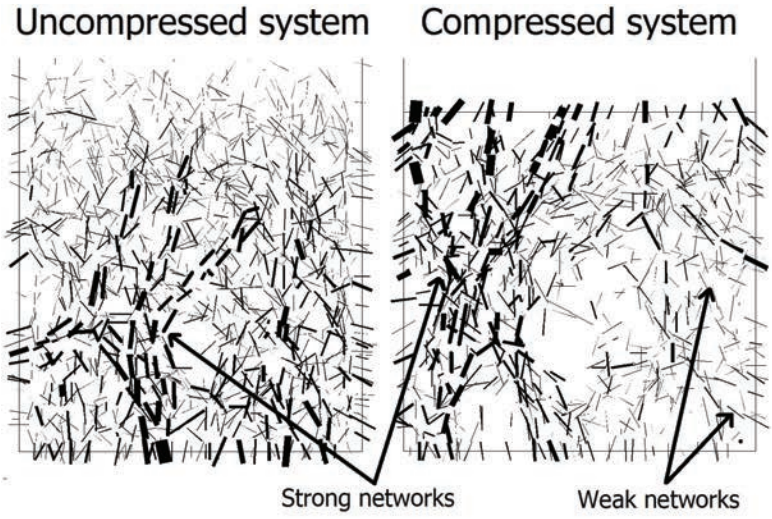

Figure 2.4: Force chain networks in granular packings

People working in the food, pharmaceutical and chemical industry as well as in the geotechnical, mining and agricultural engineering field are constantly faced with problems caused by granular materials during shipping, mixing and storage. These problems are cause by certain microstructural properties of granular materials, which are not found in solid and liquid materials. One such problem occurs during the discharge of storage containers, such as silos, where the openings suddenly get blocked (Figure 2.5).

According to the literature this is known as the arching effect and is cause by the development of a so-called disturbed region within the granular mass, which is capable of bearing its own weight as well the weight of the material above it. The disturbed region consists of a curved system of pressure forces or arch, springing from one supporting surface to another and develops due to changes in the mechanical properties of the granular mass (Csizmadia and Keppler, 2003).

Even though the arching effect is one of the primary causes of problems associated with the handling of granular materials, it can be utilized in a constructive way to build for example underground conduits and openings. In such scenarios the nature of the stress redistribution resulting from the arch formation accounts for the reduction in the overburden pressure felt by the underground

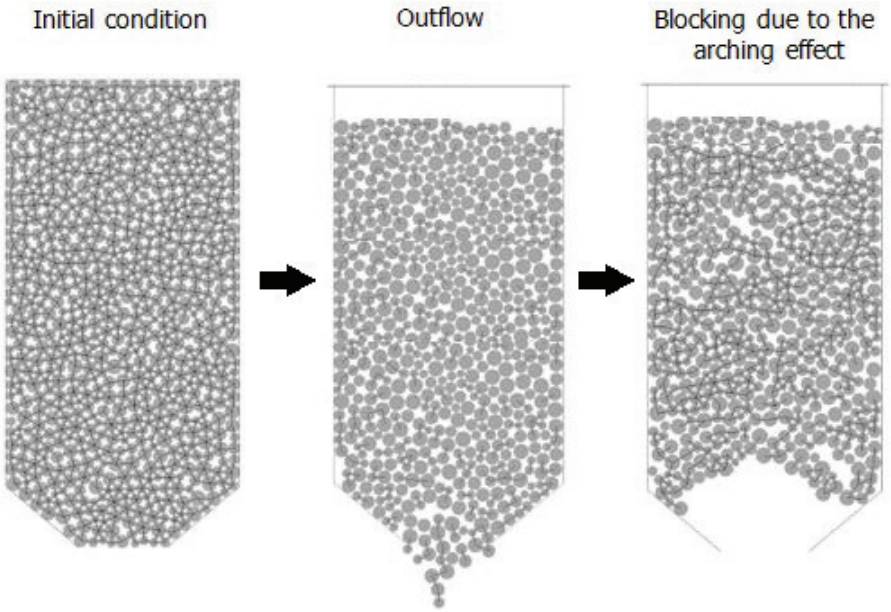

Figure 2.5: The arching effect in a silo storage container (Luting, 2011)

structure. The arching phenomena can, however, be disturbed through vibrational forces and should therefore be considered when underground structures are built through the utilization of the arching affect (Tien, 1996).

2.3. Numerical modelling of granular materials

Today a number of engineering applications are concerned with the behaviour of granular materials and the need to model such systems has increased significantly. These applications range from the processing of aggregate, ore and agricultural products with hoppers, chutes, dragline buckets, crushers and conveyer belts, typically found in the mining and food industry, to the processing of powders in the metallurgical and pharmaceutical industries as well as the breakage of rocks found as in the quarrying industry. Knowledge of the static and dynamic behaviour of granular materials can also be used in the design and development of the material handling equipment (hoppers, chutes, etc.) mentioned above (Horn, 2012).

Even though the amount of research which has been done on the behaviour of granular materials has increased considerably over the last few decades, it still remains a challenge to fully understand such systems due to their complex nature. These systems can be better understood, to some degree by means of a detailed study of the mechanical interactions between the individual particles

which make up the system. This micro-mechanical analysis can be performed either through analytical computations, experimentation or numerical simulations. The analytical approach is, however, restricted to systems subjected to simple loading conditions and containing only spherical particles of uniform size. Conducting experiments on the other hand can provide valuable information on various bulk responses associated with granular systems, but important micro mechanical properties such as contact forces remain inaccessible. Nevertheless, there have been instances where certain micro-mechanical properties have been studied through experiments, but these experiments are generally time-consuming and require expensive and complex equipment. Fortunately, due to the significant enhancements in computational resources since the nineties, the drawbacks associated with the analytical and experimental approaches can be avoided by means of numerical simulations, which have various financial and practical advantages (Fortin *et al.*, 2002).

There are two conventional methods to simulate granular systems. The first is through continuum mechanics where the material is typically modelled as a deformable continuous medium and the governing equations are solved by means of the finite element method (Frenning, 2008). This method is mostly suited for the modelling of static systems or where relatively small deformations occur (Horn, 2012) and where there is a small variation in the particle size (Dymond, 2007). This is primarily to avoid meshing and remeshing difficulties as well as mesh distortion, which can occur when large strains are encountered (Coetzee and Els, 2009). These problems can be avoided from a continuum perspective by implementing either the particle in cell method or advanced non-linear finite element techniques, but a more suitable approach would be to use the Discrete Element Method (DEM). DEM is the second conventional method commonly used to simulate granular material systems. It was originally developed by Cundall and Strack (1979) to model both dynamic and static systems consisting of particles with various shapes and sizes. It uses the same constitutive equations as the continuum method (Groger and Katterfeld, 2006), but considers the individual and interacting particles explicitly by determining the kinematic force as well as the resulting displacement on each particle for every time step (Mio *et al.*, 2009). Comprehensive information on the micro-mechanical properties of a granular system can therefore be obtained through DEM (Malone and Xu, 2008).

However, as appose to continuum mechanics, the amount of information that has to be obtained during each time step as well as the various calculations which have to be conducting during these steps strongly depend on the number of particles being modelled. Thus, if too many particles are considered, the model can become so computational intensive that it would be impractical/impossible to simulate. DEM is therefore mostly suited for models with relatively small numbers of particles ($<$ 500,000). A number of solutions to

reduce the computational resources required by DEM have been investigated though, and range from the use of parallel processing or advanced contact detection algorithms to increasing the time step by reducing the particle stiffness (Malone and Xu, 2008; Mio *et al.*, 2009).

2.4. Review of the Discrete Element Method

With DEM the interaction between particles is treated as a dynamic process in that the movements of individual particles are continuously traced (Coetzee and Els, 2009). These movements result due to disturbances caused by particle (ball) motion and body forces as well as disturbances cause by the geometric objects (walls) associated with the system. These disturbances can then propagate through the particle system and the rate of propagation depends on the physical properties associated with the system.

In general these disturbances are modelled in two stages. The first is to implement a suitable contact model which can determine all the forces acting on each particle within the system. A number of contact models have been developed such as the Walton-Braun and the Hertz-Mindlin models, which can model complex contact behaviour, but they are generally computational intensive. A more basic contact model which is normally the default contact model implemented in most of the commercially available DEM software due to its efficiency compared to other models, is the linear contact model. The linear contact model can be considered as a soft particle approach where the contact is modelled with a linear spring in both the normal, k_n, and the tangential direction, k_s (Figure 2.6). Particles in contact are thus allowed to overlap with one another and the contact forces are calculated by combining the amount of overlap between contacting particles with the spring stiffness values. The second stage is then to apply Newton's second law of motion such that the particle's acceleration can be calculated which can finally be integrated to first give the particle's velocity and then its displacement (Hanley *et al.*, 2011).

In addition, frictional slip is also introduced in the tangential direction through a friction coefficient as well as damping in the normal and tangential directions. The damping is accounted for by means of viscous dampers and the damping force is proportional to the contact velocity (Coetzee *et al.*, 2010). The end result is that the displacements and contact forces of the balls are determined at consecutive time steps by alternating between the application of the force-displacement law (through the contact model) and Newton's second law as shown in Figure 2.7.

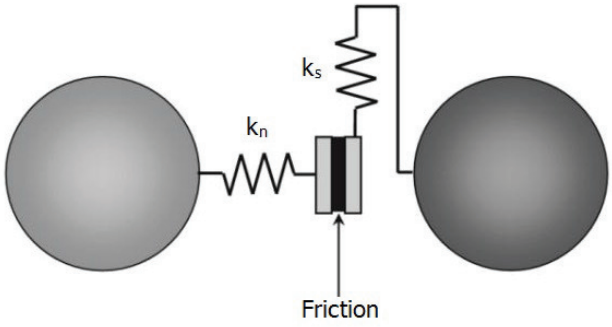

Figure 2.6: The Linear Contact DEM Model (Coetzee and Els, 2009)

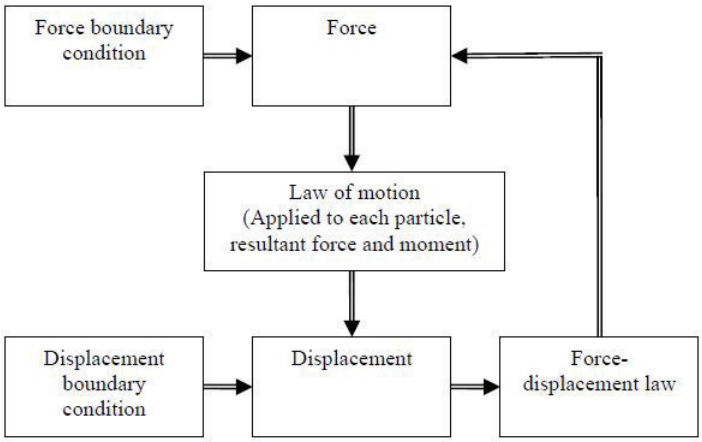

Figure 2.7: DEM calculation cycle (Zhanping You and Dai, 2006)

It should be stated that in the case of a ball-ball interaction, Newton's second law is applied to the balls to establish their relative motion, while the force-displacement law is applied at the ball contacts in order to update the contact forces. If there is a ball-wall interaction, only the force-displacement law is considered, because the presence of walls in the DEM serve as user specified boundary conditions and will remain fixed during model runs. It is also important to know that it is assumed that both the acceleration and the velocity of the balls remain constant during each time step and the time steps are so small that disturbances cannot propagate further than neighboring balls during a time step. This means that the forces on a specific ball are only due to the balls with which it is in contact with (Itasca, 2003).

DEM is mostly suited for the modelling of granular materials, but it can also be used for geo-materials. This is achieved by simply using cohesive forces to bond groups of discrete elements together in order to resemble the desired geo-material (Donze *et al.*, 2009).

2.5. Calibrating DEM models

DEM has been used by a number of researchers, but according to Chung and Ooi (2007), one crucial aspect which has not adequately been addressed is how their input parameters were selected or determined such that satisfactory quantitative predictions could be produced. In many cases, the input parameters were assumed without the proper justification and often not even measured.

It is therefore crucial that the correct input parameters are selected in order to ensure that the simulated bulk responses closely resemble the real life physical system. According to Curry *et al.* (2009), this can be achieved by correctly defining the material properties affecting the material behaviour at the particulate level (micro properties), in that they dictate the overall bulk behaviour. However, it is not always possible to directly measure these micro properties and even if in some cases it could be done, there is no guarantee that they would provide accurate results when applied in the simulations. A calibration process is therefore required, which can be performed by either implementing one of the following:

- Design of experiments (DOE) methods, which quantify the relation between dependent and independent variables by determining the effect of each factor on a specified response and singling out the most prominent factors. Regression models are then derived through the implementation of formal regression and variance analysis which provided empirical relations between the response and its factors. These empirical relations can then finally be used in an optimization scheme to obtain the correct set of micro properties (Hanley *et al.*, 2011).
- An iterative approach where each micro property is varied individually until a specified bulk response is obtained. This process is then repeated until all the required bulk responses can be simulated within acceptable accuracy levels (Horn, 2012).

Even though there are a number of disadvantages associated with the latter such as the time scales required to obtain a set of micro properties which might not even be optimal, due to the complex interaction between these properties (Hanley *et al.*, 2011), it was still selected as the calibration method for this research. This was purely based on the simplicity associated with this approached compared to the DOE methods as well as the vast computational resources made available for this research.

Irrespective of the method selected, the core of any calibration process is experimental work, whether it is to perform the actual calibration or just to verify the results from the calibration process. Numerous experimental tests have been developed specifically to quantify certain bulk responses associated with granular materials of which some of the most common are the confined compression test, the direct shear test, the rotating drum and the angle of repose.

3. Material properties

3.1. Introduction

In order to successfully model a granular system a detailed understanding of the system on both the micro (particle) and macro (bulk) level is required. An important part is therefore to identify and obtain all the required granular material properties such that the micro properties can be implemented into the DEM models in order to compare the resulting numerical bulk responses to that of the actual bulk properties obtained from experimental work.

The bulk material selected for this study was coarse crushed aggregate (Figure 3.1) with an average equivalent diameter of 32 mm (based on volume) obtained from the Portland quarry located in the Western Cape of South Africa. It was selected as it is the same type of rock which would be used for other rock bed thermal storage experiments being conducted by STERG.

Figure 3.1: Coarse crushed aggregate obtained from Portland quarry

This section, along with Appendix A, describes and summarizes how all the material properties required to model the rock beds with DEM, were measured through laboratory experiments or obtained from literature. It should be em-

phasized that a complete set of accurate micro material properties are not necessarily essential, since they will eventually be altered by the calibration process discussed in Section 4.4. The properties included in Appendix A are therefore purely for completeness.

3.2. Macro parameters

3.2.1. Bulk density, voids ratio and porosity

The bulk density, ρ_b, of a granular material closely resembles the particle density in the sense that they are calculated similarly, with the only difference being that the particle density is as the word states, specific to a particle, whereas the bulk density includes the gaps between the particles in the bulk sample. The bulk density can therefore be calculated by simply filling a specified container, of which the shape is known, with the bulk material up to a predetermined height in order to obtain the bulk volume, V_b. The container with the material is then weighed in order to obtain the bulk material mass, m_b, which is used together with the bulk volume (Equation 3.2.1) to finally give the bulk density (Head, 1989).

$$\rho_b = \frac{m_b}{V_b} \tag{3.2.1}$$

This should then be repeated for several samples such that an average bulk density can be obtained. Another parameter which goes hand in hand with the bulk density is the porosity, η, and is defined as the ratio between the voids volume and the bulk volume (Equation 3.2.2) (Head, 1989).

$$\eta = (\frac{V_v}{V_b}) \tag{3.2.2}$$

However, due to the time constraints associated with the project and the need for cumbersome measuring techniques to obtain the voids volumes, a different approach was pursued by estimating the porosity through the aid of the voids ratio, e, as follows (Horn, 2012):

$$\eta = \frac{e}{(e+1)} \tag{3.2.3}$$

The voids ratio, defined as the ratio of the volume of the voids, V_v, (gaps between the particles for a certain bulk volume) and the total solid volume, V_s (volume of the particles within the bulk volume, but without the gaps) can be estimated with Equation 3.2.4, which is simply dependent on the particle and bulk density (Head, 1989).

$$e = \frac{\rho_p}{\rho_b} - 1 \tag{3.2.4}$$

In order to determine the above mentioned bulk parameters it was first necessary to select an appropriate container with which the experiments would be conducted. It was decided to use a steel box with sides and a height equal to 0.3 m (Figure 3.2), since

- the wall to particle ratio will be large enough to potentially avoid any wall effects,
- the experiments would be easy to conduct,
- several experiments can be repeated for reliable results without taking too much time, and
- the number of particles within the experiment would not make the numerical models too computationally intensive to conduct.

Filling the steel box with the crushed aggregate is a very important process because the filling procedure can effect the overall behaviour of the bulk sample and it has to be done it such a way that it can be repeated as closely as possible in the numerical simulations. The filling process was executed by pouring the aggregate from an initial starting height and then gradually increasing the pouring height such that it more or less resembled the rainfall method used in DEM and discussed in Section 4.2.

The filling process was repeated until the experimental box was filled to the brim and the total mass of the material was obtained by measuring the weight

Figure 3.2: Steel container used to calculate the bulk density and porosity

of the material in each bucket before it was poured into the container. The bulk sample was then carefully levelled after which the bulk mass could be determined by sub-tracking the mass of the particles removed during the levelling. This bulk (solid) mass was then used together with the volume of the square experimental box to calculate the bulk density (Equation 3.2.1) and once the bulk density was known the rest of the parameters could be obtained through the use of Equations 3.2.3 and 3.2.4. This experiment was repeated three times to insure accuracy and reliability and the final results are summarized in Table 3.1.

Table 3.1: Summary of the experimental bulk density, voids ratio and porosity

Bulk parameters	**Run 1**	**Run 2**	**Run 3**	**Average**
Bulk Density (kg/m^3)	1360	1331	1379	1357
Porosity (%)	47.9	49.0	47.2	48.0
Voids Ratio	0.92	0.96	0.89	0.92

3.2.2. Contact forces on system walls

The relationship between the contact force on the bottom and side walls of a confined bulk material sample gives a good indication of how the forces within the sample are being transmitted to the system boundaries. It is a very important macro parameter to investigate since it depends on several micro parameters (Horabik and Rusinek, 2002) and can be obtained through a confined compression test similar to the one presented in Figure 3.3.

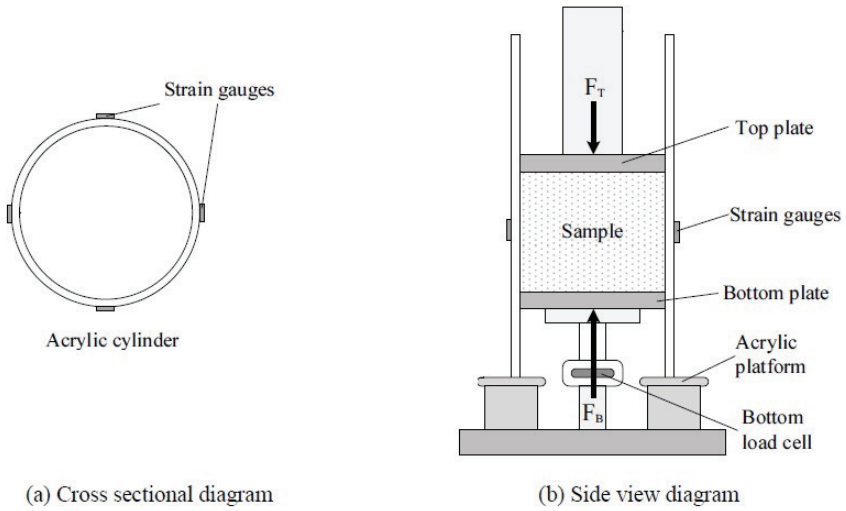

Figure 3.3: Schematic of a typical cylindrical confined compression test (Chung and Ooi, 2006)

This arrangement is typical for a cylindrical confined compression test where the bottom plate is free to move and is connected to a load cell in order to measure the vertical force resulting from the solid pressure of the bulk material sample. The lateral force on the other hand is measured by means of strain gauges connected to the outside of the cylindrical wall. A similar confined compression test setup was available (see Section 3.2.4), but unfortunately it was not designed with the purpose of measuring the contact forces on the bottom or side walls. Nevertheless, the square steel container used to determine the bulk density and porosity could be modified to measure the contact forces by simply connecting suitable load cells to the bottom and side walls as shown in Figure 3.4. Two 50 kN HBM S9 load cells were used per wall to ensure stability, but due to limited availability only one of the walls could be fitted at a time. Nonetheless, this meant that both the porosity and one of the wall forces (bottom or side) could be obtained from one experiment. Not only did this reduce the amount of time spend to conduct all the necessary experiments, the computational time required to conduct the numerical simulations was also reduced because several bulk responses (bulk density, porosity and boundary contact forces) could be obtained from a single simulation. The experiment was repeated three times and the final results are summarized in Table 3.2.

Table 3.2: Summary of the experimentally measured normal contact forces on the bottom and side walls

Bulk parameters	**Run 1**	**Run 2**	**Run 3**	**Average**
Bottom wall (N)	349	344	341	345
Side walls (N)	149	155	152	152

Figure 3.4: Square steel container modified to measure the normal contact forces on the bottom and side walls

The reason for the relatively large vertical to lateral pressure ratio, as compared to fluid mechanics, can be explained by means of the following. If one considers for instance that the steel container used in the above experiments was to be filled with a liquid, the resulting vertical, P_z, and lateral, P_L, pressures would be:

$$P_z = P_L = \rho_{liq} g H \tag{3.2.5}$$

where H is the height of the container, ρ_{liq} is the density of the liquid and g is the gravitational force. The vertical to lateral pressure ratio then simply reduces to 1.

For a granular material on the other hand, this is not the case in that the vertical to lateral pressure ratio would differ for different granular materials. This phenomenon can best be explained by means of Janssen's theory as follows (Di Felice and Scapinello, 2010): If a granular material is confined in a cylindrical vertical column (can be square or rectangular, but cylindrical is chosen for simplicity), the force balance in the vertical direction for any horizontal slice can be written as

$$\frac{dP_z}{dz} = \rho_b g - (\frac{4}{D} P_\mu) \tag{3.2.6}$$

where P_z is the average vertical solid pressure, z is the vertical coordinate which is positive in the downward direction, ρ_b is the bulk density of the sample, D is the hydraulic diameter of the horizontal slice and P_μ is the pressure resulting from the friction between the bulk material and the column wall. However, P_μ is also related to the radial pressure through the friction coefficient, μ, as follow:

$$P_\mu = \mu P_r \tag{3.2.7}$$

which in itself is related to the vertical pressure through a constant factor known as Janssen's constant (Equation 3.2.8):

$$P_r = K P_z \tag{3.2.8}$$

This assumed relationship between the radial and vertical pressure can then be used together with Equation 3.2.7 in order to rewrite Equation 3.2.6 as

$$\frac{dP_z}{dz} = \rho_b g - \frac{4}{D}(\mu K) P_z \tag{3.2.9}$$

which can finally be integrated to give:

$$P_z = P_{sat}[1 - e^{(-\frac{z}{z_{sat}})}] + P_0 e^{(-\frac{z}{z_{sat}})} \tag{3.2.10}$$

The boundary condition used to perform the integration corresponded to a pressure of P_0 at $z = 0$ (top of column). Nonetheless, in Equation 3.2.10, P_{sat} is simply the saturation pressure given by

$$P_{sat} = \frac{\rho_b g D}{4(\mu K)} \tag{3.2.11}$$

while z_{sat} is the saturation depth given by

$$z_{sat} = \frac{D}{4(\mu K)} \tag{3.2.12}$$

From Equation 3.2.10 it is clear that in the case of a zero pressure on the top of the sample, such as in the experiments conducted here, the vertical pressure varies linearly with depth, similar to a liquid (Figure 3.5). However, this only occurs for values smaller that the saturation depth and for larger depths the vertical pressure reaches an asymptotic value.

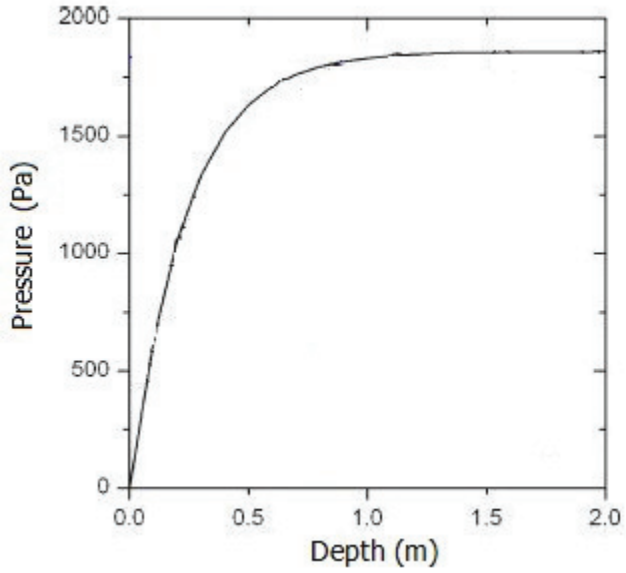

Figure 3.5: Graphical representation of Janssen's theory (Di Felice and Scapinello, 2010)

The reason for this asymptotic saturation pressure is due to the interlocking effect associated with granular materials and the more interlocking occurs the less forces are transmitted to the side walls resulting in a larger vertical to lateral pressure ratio compared to a liquid where there is no interlocking. In

addition, Equation 3.2.10, also reveals that the effect of an externally applied pressure on the top of the packing will decay exponentially with depth (Di Felice and Scapinello, 2010).

3.2.3. Internal friction angle and angle of repose

The internal friction angle is the macro parameter which characterizes the bulk material flow properties and can be used to quantify the bulk frictional properties of the material. The most widely used technique to estimate the internal friction angle is by means of a direct shear test. The test setup used to perform such a test usually consist of a bulk material sample contained in a steel container (cylindrical, square or rectangular in form) constructed from two halves (top and bottom). The sample is then confined by applying a specified, but constant normal load through a lid placed on top of the sample. Once the normal load is applied a second lateral load is applied to the bottom half such that the sample is sheared due to the relative movement between the top and bottom halves, as shown in Figure 3.6.

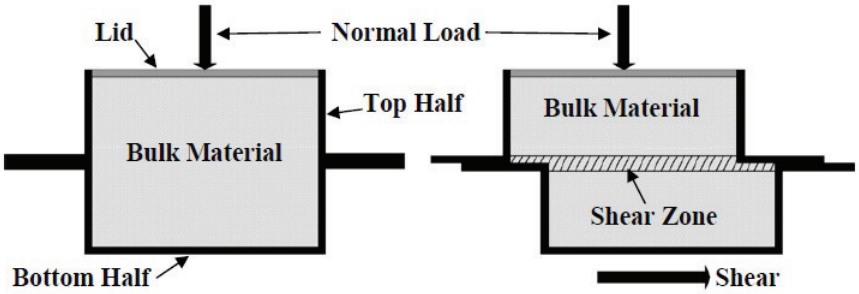

Figure 3.6: Schematic of a typical direct shear test (Horn, 2012)

The lateral load is finally increased until shear failure occurs in the sample at which point both the shear and normal stresses are recorded. The experiment is then repeated using different normal loads. The different shear stresses, σ_s, which result in shear failure can then be plotted against their corresponding normal stresses, σ_x (Figure 3.7), to obtained what is known as a Coulomb (or failure) envelope (Hartl and Ooi, 2008). A linear fit can then be applied to the data points, after which the gradient of the linear fit can be used to finally estimate the internal friction angle as follows:

$$\phi = tan^{-1}(\frac{\Delta\sigma_x}{\Delta\sigma_s}) \tag{3.2.13}$$

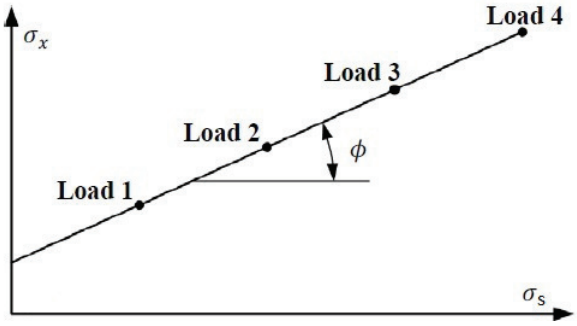

Figure 3.7: Coulomb envelope (Horn, 2012)

Unfortunately an operational direct shear box was not available at the time and it was necessary to take an alternative approach. It was therefore decided to implement the angle of repose test. The angle of repose of a bulk material sample is simply the angle between the free surface and the horizontal of a solid pile formed by one of the following processes. Discharging the material from a funnel or hopper, either onto a fixed bed or any flat surface such that a stable free-standing pile is formed or by lifting a bottomless container filled with the bulk material, such that the pile is formed (Figure 3.8). These methods are commonly known to form a static angle of repose. Alternatively, the sample can be allowed to form what is known as the dynamic angle of repose by rotating it in a cylinder or by tilting a container filled with the material until the material starts to avalanche (Figure 3.9) (Ileleji and Zhou, 2008).

The fact that there is a difference between the static and dynamic angle of repose as well as the dependence on various micro parameters such as friction, the particle shape and size distribution as well as the way in which the angle of repose test is executed, has led to numerous debates among researchers on the usefulness of the angle of repose test as a flow property (Zhou *et al.*, 2002). The reason being that because of all these factors which can influence the final outcome of the test, it is very challenging to accurately define and therefore interpret the results from such tests (Ileleji and Zhou, 2008). However, because it is relatively simple and inexpensive to obtain the angle of repose (static or dynamic), it is a useful test to obtain a basic understanding of the behaviour of a bulk material sample with regard to flow or frictional characteristics if a direct shear test cannot be conducted.

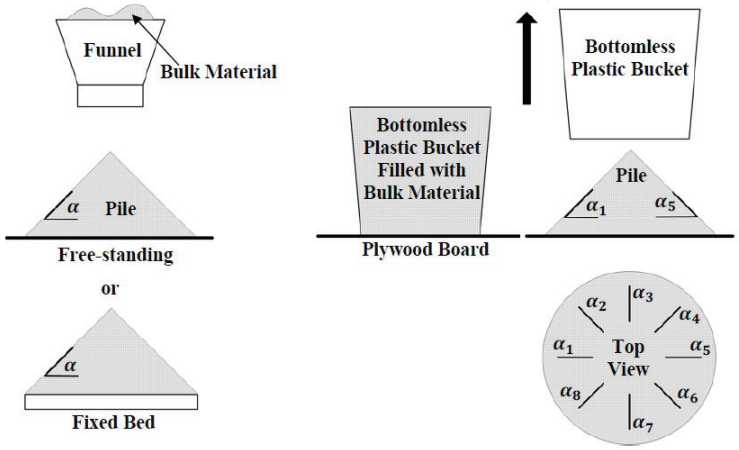

Figure 3.8: Schematics of static angles of repose (Horn, 2012)

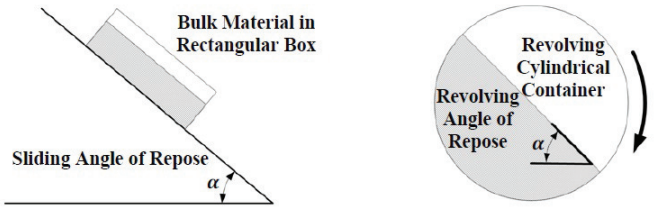

Figure 3.9: Schematic of dynamic angles of repose (Horn, 2012)

The angle of repose of the crushed aggregate was therefore determined by simply removing the sides of the steel container used to determine the porosity and contact forces, discussed in Sections 3.2.1 and 3.2.2, by allowing the material to form a pile, as shown in Figure 3.10.

Even though this approach differs slightly from the methods described above it still led to the same outcome and it ensured that several bulk responses, namely the bulk density, porosity, boundary contact forces and angle of repose could be estimated from one experimental setup and bulk material sample. This would also mean that the simulations could also be performed in the same sequence which is much more efficient that conducting them separately. Nevertheless, a number of surface angles were then measured, using a digital protractor and the experiment was repeated several times to obtain an average angle of repose of 35.6°. However, since the numerical angle of repose would have to be determined by means of visual inspection it was decided to alter the way in which the experimental angle of repose would be determined.

Several photos from different angles were therefore obtained and used together with a Matlab code, which could determine the angle of repose in a objective

Figure 3.10: Experimental method used to estimate the angle of repose

way (not always the case when using the digital protractor). The program would establish the coordinates corresponding to the free surface of the pile for a given range specified by the user, after which a polygon fit would be applied in order to finally obtain a linear fit. The angle between the horizontal surface and the linear fit could then be used to determine the angle of repose (Figure 3.11).

With this approach an average experimental angle of repose of 36.0° was obtained (Table 3.3), which closely resembled the angle obtained with the protractor and this added confidence in the use of this method to estimate the angle of repose during the numerical stages.

Table 3.3: Summary of the experimental angles of repose obtained

Bulk parameter	**Run 1**	**Run 2**	**Run 3**	**Average**
Angle of repose (°)	35.6	36.4	36.1	36.0

In addition another experiment was conducted by filling a bottomless plastic bucket, resting on a plywood board, with the bulk material. The bucket was then lifted manually and very slowly so as to form a pile as can be seen in Figure 3.12, which resulted in an angle of repose of 37.2°. This additional test was only conducted as a final check and would not be considered during the numerical stages, but it does show that the angle of repose is process dependent.

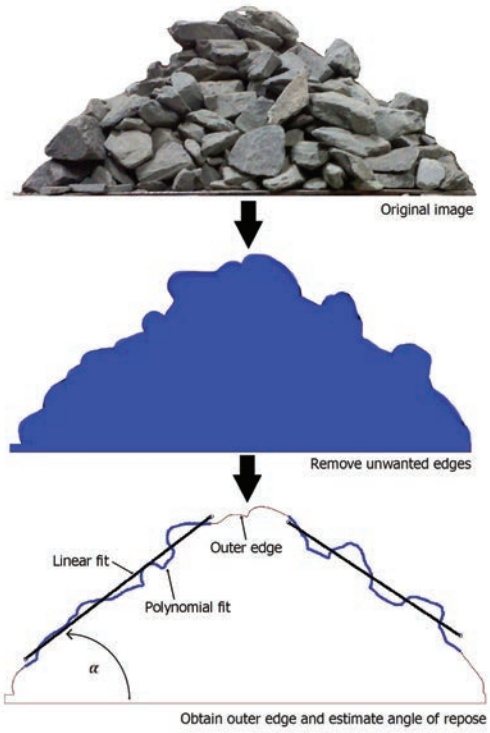

Figure 3.11: Calculating the angle of repose through image processing in Matlab

Figure 3.12: Additional experimental method to estimate the angle of repose

3.2.4. Bulk stiffness

The bulk stiffness, also known as the bulk elasticity, of a granular material packing is an indication of the macro stiffness characteristics of the sample and it is directly related to the confined Young's Modulus, which can be derived from the confined compression test (Horn, 2012). A schematic of a typical confined compression test can be seen in Figure 3.13, where the bulk material sample is contained within a cylindrical container (other container shapes such as a square box for instance can also be used, but the cylindrical one is the most commonly used method). A lid is also included so as to apply a normal load in the vertical direction. The sample will therefore experience a bulk strain in the vertical (longitudinal) direction, due to the applied normal force, but is restricted to undergo any bulk strains in the lateral directions.

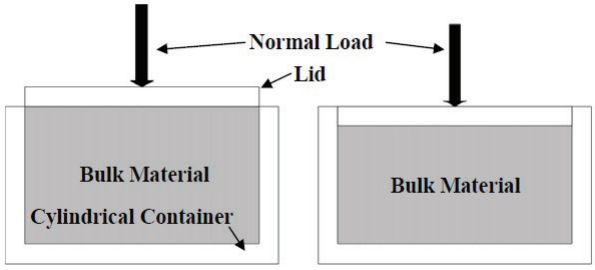

Figure 3.13: Simplified schematic of a typical cylindrical confined compression test (Horn, 2012)

A complete confined compression test can then be conducted by increasing the magnitude of the applied vertical load up to a certain maximum load and then reducing the load to zero. This loading and unloading process is known as a compression cycle and has to be repeated several times in order to obtain sufficient data. The normal load, F, and the displacement have to be recorded so that the bulk vertical stress, σ_z, and strain, ε_z, can be calculated with:

$$\sigma_z = \frac{F}{A_{cct}} \tag{3.2.14}$$

$$\varepsilon_z = \frac{L - L''}{L} \tag{3.2.15}$$

where A_{cct} is the cross sectional area of the lid, L is the initial packing height and L'' is the compressed height. The confined Young's Modulus, E', can then be obtained by simply dividing the change in the vertical stress by the change in the vertical strain, over a specified range, as follows:

$$E' = \frac{\Delta\sigma_z}{\Delta\varepsilon_z} \tag{3.2.16}$$

In order to establish the appropriate range for which the change in stress and strain will be determined, one can plot the bulk vertical stress against the bulk vertical strain in order to obtain a graph similar to Figure 3.14. From Figure 3.14 it is clear that the first compression cycle differs from the remaining compression cycles in that its loading part is more non-linear with a lower stiffness. This behaviour is a result of a sample which is not sufficiently compacted before the test is conducted and therefore is subject to a lot of inter-particle movements during the first compression cycle. Nevertheless, once the sample has been compacted and no subsequent inter-particle movements can take place, the linear relation between the stress and strain will be more or less constant for the remaining compression cycles, as can been seen in Figure 3.14. The slope of the loading parts of each compression cycle, excluding the first compression cycle, can then be used to calculate the confined Young's Modulus (Equation 3.2.16).

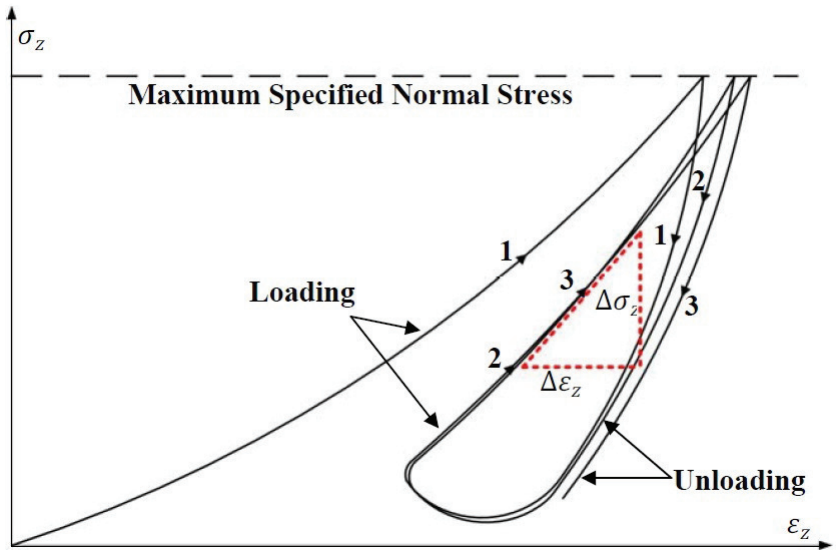

Figure 3.14: Typical compression cycles resulting from a confined compression test (Horn, 2012)

To better understand why these slopes are used to estimate the confined Young's Modulus one can consider the following. The confined Young's Modulus can be derived from the material's Young's Modulus, E, and Poisson's ratio, ν, as shown in Equation 3.2.17, if it is assumed that the material is an isotropic medium (Horn, 2012).

$$E^{'} = E[\frac{1-\nu}{(1+\nu)(1-2\nu)}] \tag{3.2.17}$$

However, if one considers the vertical or longitudinal stress in the sample, from a general solid mechanics point of view,

$$\sigma_z = \frac{\nu E}{(1+\nu)(1-2\nu)}(\varepsilon_x + \varepsilon_y + \varepsilon_z) + \frac{E}{1+\nu}(\varepsilon_z) \tag{3.2.18}$$

and taking $\varepsilon_x = \varepsilon_y = 0$ (no lateral strains), Equation 3.2.18 can be simplified to:

$$\sigma_z = E\varepsilon_z[\frac{1-\nu}{(1+\nu)(1-2\nu)}] \tag{3.2.19}$$

which can finally be substituted back into Equation 3.2.17 to give Equation 3.2.16. In addition, according to Horn (2012), once the confined Young's Modulus is known the bulk stiffness of the packing, k_b, can be estimated with

$$k_b = \frac{A_{cct}}{L}E' \tag{3.2.20}$$

An confined compression test was conducted by making use of the experimental setup presented in Figure 3.15, which was designed and constructed by Horn (2012). The setup consisted out of a cylindrical steel container with a diameter of 0.34 m, a height of 0.37 m, a cylindrical lid with a diameter of 0.33 m (such

that it can move vertically within the steel container), a 1.5 m long steel lever arm (used to increase the compression load) and a linkage mechanism which links the lever arm with the container lid through a 50 kN HBM S9 load cell as well as an HBM 20 cm LVDT. It should be noted that due to the placement of the load cell it will only measure the weight of the linkage mechanism and any additional weights connected to it, the weight of the lid on the other had has to be measured before hand, such that it can be added to the measurements from the load cell during the data processing of the experimental results.

Figure 3.15: Experimental confined compression setup

The container was filled by pouring the material from a fixed height, after which the sample was carefully levelled such that the initial bulk height corresponded to the height of the container wall. The container lid was then connected to the lever arm through the linkage mechanism and the lid was carefully lower until it slightly touched the packing. This was necessary such that the LVDT could be zeroed. The lid was then allowed to rest on the packing, which compressed the sample, due to the combined weight of the lid, linkage mechanism and lever arm. The displacement resulting from the compression was then recorded together with the normal load on the sample. The normal load was then increased incrementally, by adding 10 kg weights to the lever arm until a total of 50 kg was reached, each time recording the normal load as well as the displacement resulting from the compression. The process was then reversed by removing the 10 kg weights until only the lid, linkage

mechanism and lever arm was left, once again recording the normal load and displacement due to the unloading. This represented one compression cycle, which consisted out of a loading and an unloading phase and was repeated three times to complete the confined compression test. The entire experiment was also repeated three times to ensure repeatability.

The data obtained from the load cell and the LVDT could then be used together with Equations 3.2.14 and 3.2.15 to plot the bulk stress against the bulk strain (Figure 3.16).

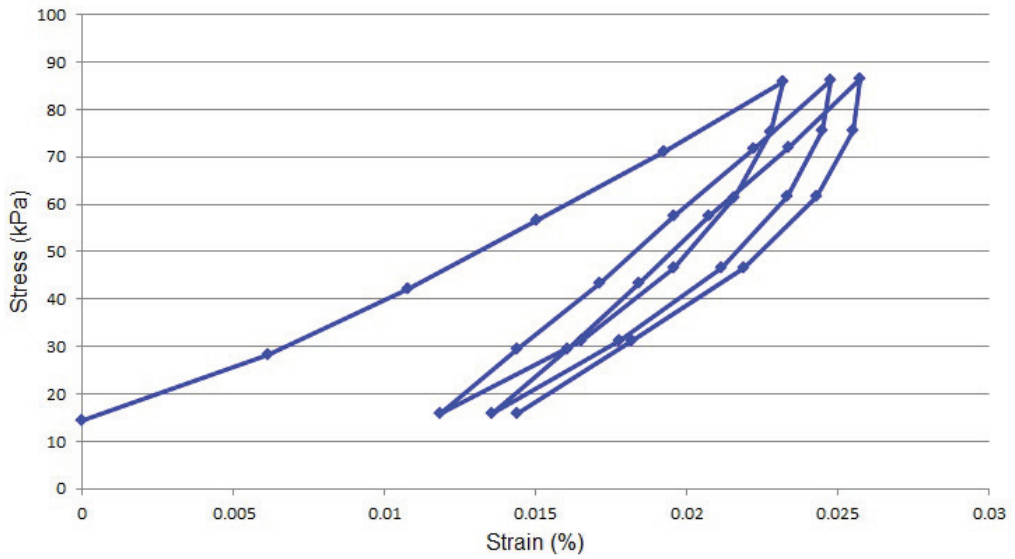

Figure 3.16: Typical stress-strain results from a experimental confined compression test (Horn, 2012)

Equation 3.2.16 was then used to determine the gradients for all the compression cycles, excluding the first one, in order to obtain the average confined Young's Modulus. With this approach the average confined Young's Modulus was estimated to be 5.853 MPa, which resulted in an average bulk stiffness of 1.436 MN/m (using Equation 3.2.20)(Table 3.4).

Table 3.4: Summary of the experimental confined Young's modulus and bulk stiffness

Bulk parameters	**Run 1**	**Run 2**	**Run 3**	**Average**
Confined Young's modulus (MPa)	5.721	6.210	5.627	5.853
Bulk stiffness (MN/m)	1.404	1.524	1.381	1.436

4. Development of DEM model

4.1. Introduction

It is important to understand that a computer model can only produce accurate and reliable results if the developer followed the correct procedure to plan, develop and execute the model. This section is therefore concerned with the proper application of the DEM software and will give an outline of the steps followed to model packed rock beds.

4.2. DEM implementation

The simulations were performed with the commercially available DEM package, PFC3D, developed by the Itasca consulting group in Minneapolis (Itasca, 2003). The typical approach with DEM modelling is to first create the system boundaries or in this case the walls resembling the cylindrical container used to conduct the confined compression test as well as those of the square bed used to conduct the rest of the experiments discussed in Section 3.2. Once these boundaries have been created the applicable wall properties can be set, after which the particles can be introduced into the model in one of two ways. The first is to specify the exact coordinates at which a particle should be created, while the second is to specify a region within which the particle will be created at any random location, commonly known as the rainfall method (Figure 4.1). The latter is typically used to create randomly packed beds similar to the ones considered in this study whereas the former is mostly suited for applications with more organized structures. Nevertheless, once the particles have been created, their micro properties can be set and gravity can be activated.

Two things should be noted with regard to the application of the micro properties, specifically with regard to the damping and stiffness properties. Both these properties can be introduced in PFC3D in the normal and shear directions. According to Malone and Xu (2008), the shear contact parameters can

be based on their normal counterparts if they are not available or difficult to measure and this was the approach adopted for this research. Once all the particle and wall properties have been applied the particles are allowed to settle under gravity and interact with any boundaries or external forces they come into contact with (Figure 4.1).

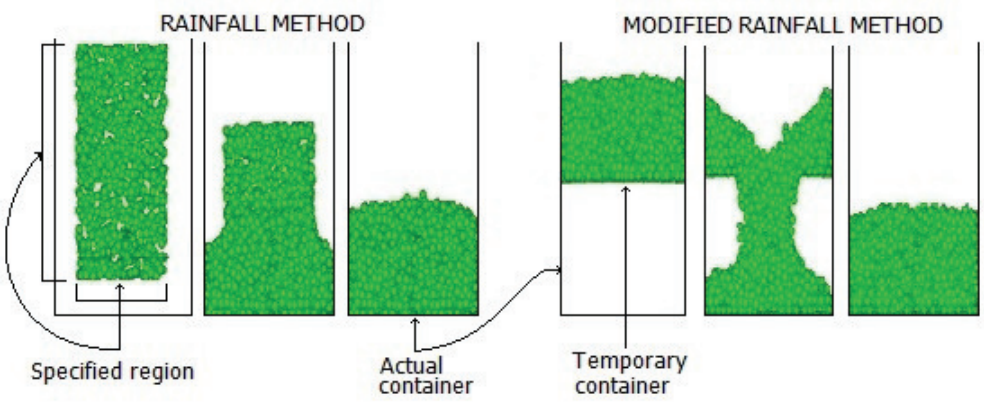

Figure 4.1: Different particle settlement schemes

One major drawback of PFC3D, and most of the other commercially available DEM software packages, is that they can only model spherical particles. If one is therefore interested in irregular shaped particles, such as the crushed aggregate used for this research, several spherical particles have to be clustered together in order to resemble the desired shape (Kruggel-Emden *et al.*, 2008). The spheres comprised in these clusters can overlap one another without generating additional contact forces and their centres remain at fix locations (Itasca, 2003). Even though research on the validity of the cluster approach is very limited, it is arguabily the most efficient and robust method to model irregular shaped particles with DEM, since the contact detection and force calculation are still based on simple algorithms (Kruggel-Emden *et al.*, 2008).

In PFC3D, the cluster method can be implemented by either bonding or clumping several particles together. The two methods only differ in the sense that the clumped particles are permanent and cannot be broken apart whereas the bonded assembly can be broken apart if the contact forces on the particle are large enough to overcome the bonding forces. The bonding method is therefore more suited when various particle breakage, failure or crack propagation studies are of importance. It can therefore be argued that the bonding method would have to be used when packed beds are modelled, since the contact forces within such beds could be large enough to break/fracture some of the rocks. However, the clump method was deemed to be more suitable for this research since:

- The bonded method treats each bond as an extra particle, increasing the computational time.
- The bonding forces required to accurately resemble the crushed aggregate were not available.
- A simplified rock breakage/failure study can still be conducted with the clumps by simply analysing the contact forces within the bed and using the results together with the relevant information from literature in order to estimate if some of the rock particles would have been subjected to breakage/fracture.

The clumping method could be implemented with the aid of a commercially available automatic clump generator called ASG3D (Cogency, 2012), as follows:

i) Import the surface mesh of each individually scanned particle, used to determine the shape and size distributions (see Appendix A.1), into ASG3D. The automatic clump generator would then randomly fill the surface mesh with a user defined number of spherical particles, after which the radii and centre positions of all the spheres would be optimized in order to minimize the volume error associated with the reconstructed clump (Figure 4.2).

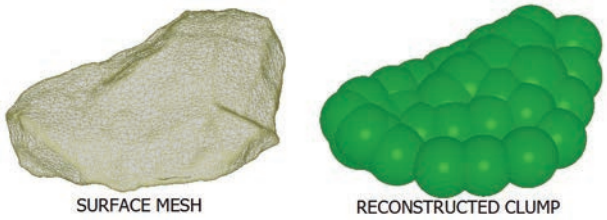

Figure 4.2: Rock reconstruction using automatic clump generator

Even though the volume error can be decreased by increasing the number of spheres, this would have a direct negative impact on the DEM computational time. Care should therefore be taken when deciding on the accuracy to which the clumps should be reconstructed. With this in mind each sample was reconstructed with 10, 35 and 75 spheres respectively and resulted in volume errors shown in Figure 4.3. It is clear that the respective volume errors decrease significantly as the number of spheres per clump increases. The most noticeable decrease corresponded to the clump representing the flat particles, simply because its minor axis is much smaller compared to the other two axes. This resulted in a

scenario where the spheres would have to become relatively large in order to completely fill the surface mesh, which in effect resulted in the high volume error associated with the clump. It was finally decided to approximate the shape of the rock particles with 35 spheres per clump, but this would only be an initial estimate in order to conduct the sensitivity study presented in Section 4.3.

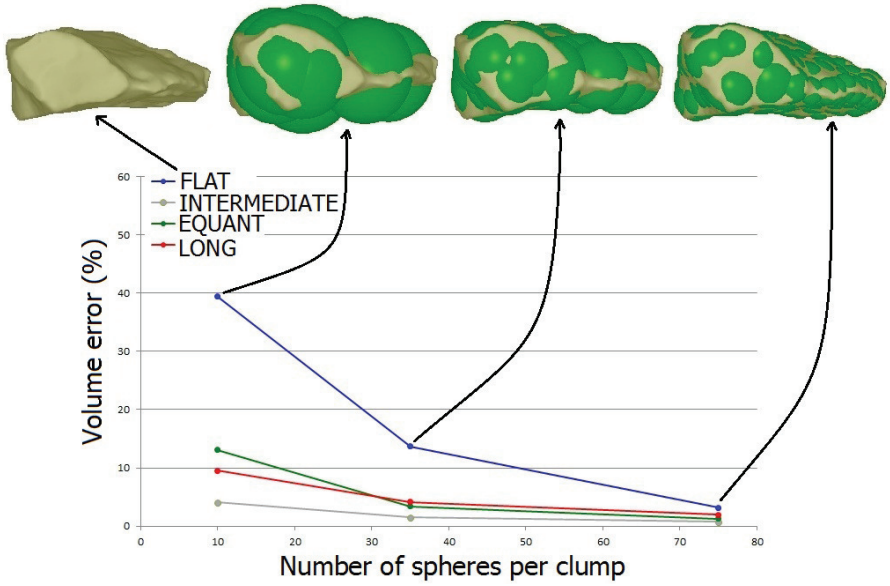

Figure 4.3: Volume errors associated with reconstructed rock particles

ii) A template containing the coordinates and the radii of all 35 spheres used in the reconstruction, as well as the volume of the reconstructed particle could then be exported from ASG3D for each of the scanned particles.

iii) The clumps could then be introduced into the DEM models by first generating a number of spheres representing the number of particles to be modelled, according to the rainfall method and with radii resembling the size distribution summarized in Table A.1.

iv) A representative template from each shape group was then used to replace the spheres created in the previous step with the respective clumps in order to introduce the shape distribution into the models. The clump logic in PFC3D does this by first mapping the center point of the clump over that of the sphere (orientation is random) and then to change the radii of the individual spheres making up the clump, such that the volume of the clump finally matches that of the initially generated sphere. One can therefore vary the size of the reconstructed clump by simply changing the volume of the sphere it replaces and/or the shape by using different templates.

4.3. DEM sensitivity study

A properly implemented sensitivity study would not only give the researcher a better understanding of the characteristics of the numerical models, but would also provide valuable insight into the effects of the micro properties on the various bulk properties that will ultimately form the basis on which the calibration process would be conducted. The sensitivity analysis focused on all the micro parameters obtained in Appendix A, by simulating the confined compression test as well as the rest of the experiments conducted with the square steel container, as follows.

- Steps followed to simulate the confined compression test

  i) Create container boundaries (a temporary container was created above the actual cylindrical container, as shown in Figure 4.1 in order to facilitate the filling process described in step iv).

  ii) Introduce 4000 clumps into the model by using the rainfall method and apply reference micro properties. This was the number of particles required to fill the cylindrical container to the desired height and was determined through a trail and error process.

  iii) Allow clumps to first settle into the temporary container located 0.1 m above the actual container, as shown in Figure 4.1.

  iv) Select a specific micro property, change it to desired value, while keeping the rest of the micro properties constant and allow the clumps to settle into the actual container. This filling process, named the modified rainfall method in this research, was necessary such that the actual filling process, where the rocks were poured into the cylindrical container from a height of approximately 0.4 to 0.5 m, could be simulated more closely.

  v) Once the clumps have settled the packing is levelled, after which a compression force is applied in a similar fashion as in the experiment, in order to finally derive the numerical bulk stiffness.

  vi) Steps iv and v were then repeated by varying the micro property under investigation over a range of different values as well as for different micro properties in order to attempt to understand how the bulk stiffness is affected by the various input parameters.

- Steps followed to simulate the rest of the bulk properties (corresponding to the square steel container)

  i) Create container boundaries

  ii) Introduce 800 clumps into the model by using the rainfall method and apply reference micro properties.

  iii) Select a specific micro property, change it to the desired value, while keeping the rest of micro properties constant and allow the clumps to settle into the container, similar to the rainfall method shown in Figure 4.1. Once the clumps have settled and the packing is levelled the porosity, bulk density and normal contact forces on the bottom and side walls can be derived (see Appendix B for more detail).

  iv) The angle of repose can then be obtained by removing the side walls one after the other, each time allowing the particles to first come to rest before the next wall is removed.

  v) Steps iii and iv were then repeated, by varying the micro property under investigation over a range of different values as well as for different micro properties in order to understand how the various bulk responses are affected by the input parameters.

The set of reference micro parameters used to conduct the sensitivity study is summarized in Table 4.1 and correspond to the experimentally obtained values, discussed in Appendix A. It should be stated that all the results from the sensitivity study were based on the average values obtained from repeating each simulation three times in order to ensure repeatability and the final results are summarized in Appendix C.

Table 4.1: Summary of the experimentally obtained micro properties

Micro parameters	**Value**
Particle to particle friction	0.72
Particle to wall friction	0.62
Particle density (kg/m^3)	2610
Particle stiffness (MN/m)	1.72
Critical damping ratio	0.8
Clump accuracy (Number of spheres per clump)	35

4.4. Model calibration

Before the calibration phase is discussed it is first necessary to understand the need for such a process and the best way to achieve this is to study the bulk responses obtained from the reference micro properties (Table 4.2).

Table 4.2: Bulk responses from reference micro properties

Bulk property	**Experimental**	**Numerical**	**% Variation**
Porosity (%)	48.0	52.2	8.64
Bulk density (kg/m^3)	1357	2117	56.02
Bulk stiffness (MN/m)	1.436	3.095	115.55
Angle of repose (°)	37.0	38.7	4.5
Normal contact force on bottom wall (N)	345	597	75.7
Normal contact force on side wall (N)	152	163	54.95

It is clear from the results in Table 4.2 that the experimentally obtained micro parameters cannot directly be implemented into the DEM models, without some sort of calibration process to ensure that the resulting bulk characteristics are indeed accurate. Even though some of the micro parameters such as the particle stiffness were simply taken from literature, which could explain the large variation between the numerical and experimental bulk stiffness, most of the properties were obtained through experimental methods and one would expect smaller variations. Section 2.5 highlighted the different calibration methods, but as was mentioned, a simple iterative approach would be followed due to the time constraints associated with this project. The overall procedure would be to vary a specific micro parameter over a range of values, while keeping the rest constant until its corresponding bulk responses correlate with that of the experimental values.

The calibration process started by first considering the clump accuracy, since it would have the most significant effect on the run times of all the remaining simulations. Therefore, based on the results from the sensitivity study it was decided to implement a clump accuracy of 10 spheres per clump. Not only would the run times be reduced from more or less a day (in the case of 35 spheres per clump) to only a few hours, the internal volume error associated with the spherical overlaps would also be reduced, while still obtaining accurate bulk responses.

The next step in the calibration process was focused on the particle density, which could be calibrated against the bulk density as well as the normal contact forces on the bottom and side walls. The respective bulk simulations were

therefore repeated for 6 different particle densities ranging from 500 kg/m^3 to 5000 kg/m^3 and the resulting bulk responses are presented in Figures 4.4 to 4.6.

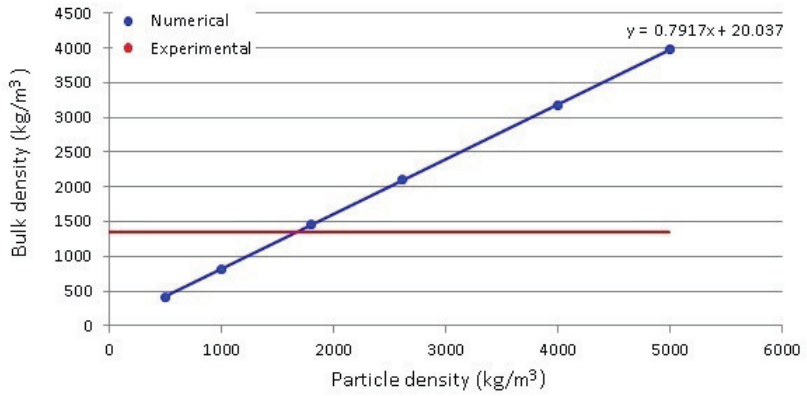

Figure 4.4: Calibrating the particle density against the bulk density

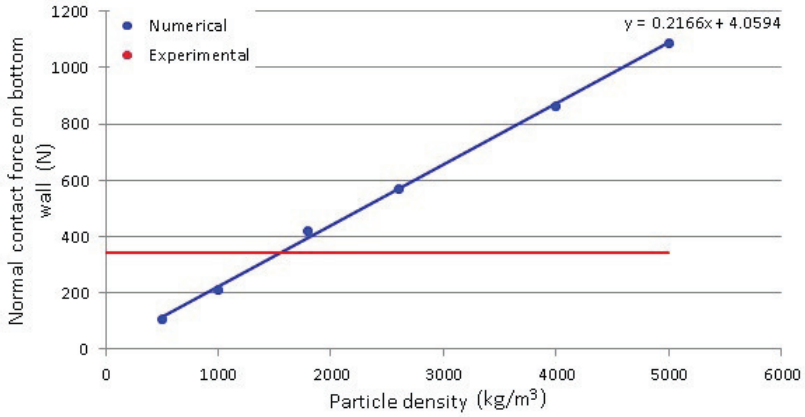

Figure 4.5: Calibrating the particle density against the normal contact force on the bottom wall

The particle density could not be calibrated by simply identifying the intersecting point between the numerical and experimental values , since there were three different intersecting points corresponding to the three bulk responses. A better approach was to derive appropriate regression models for each bulk response as a linear function of the particle density (Figures 4.4 to 4.6) and to use the regression models together with the Excel solver in order to obtain the particle density resulting in the smallest total relative error, E_r, where E_r is calculated as:

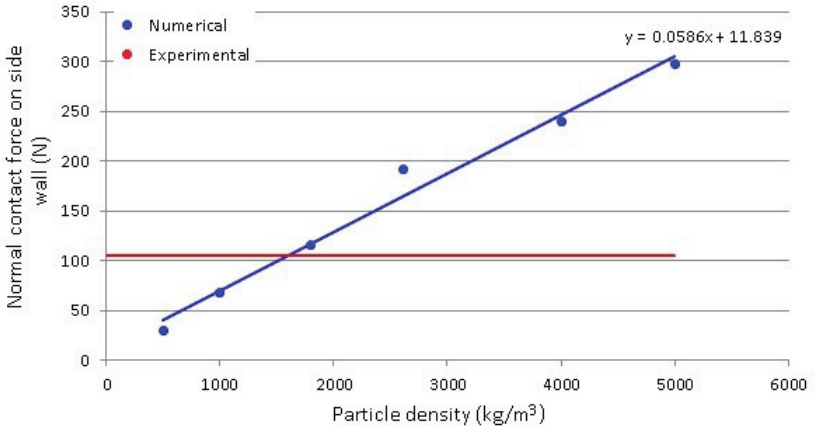

Figure 4.6: Calibrating the particle density against the normal contact force on the side walls

$$e_r = \frac{Experimental - Numerical}{Experimental}$$
$$E_r = \sqrt{(e_{r\_BD})^2 + (e_{r\_CFBW})^2 + (e_{r\_CFSW})^2} \qquad (4.4.1)$$

In Equation 4.4.1, e_r is simply the relative error between the experimental and numerical value for a specified bulk response, whereas e_{r_BD} is the relative error associated with the bulk density, e_{r_CFBW} is the relative error associated with the normal contact force on the bottom wall and e_{r_CFSW} is the relative error associated with the normal contact force on the side walls. Nevertheless, this approach resulted in a particle density of 1610 kg/m^3, which finally lead to a bulk density of 1286 (kg/m^3) as well as normal contact forces of 381 N and 117.3 N on the bottom and side walls, respectively.

The next micro parameter was the particle to particle friction (PPF), which had to be calibrated against all the bulk responses considered for this research, by repeating the respective simulations for 6 different PPF's ranging from 0.1 to 1.0. Similar to the particle density, a regression model approach was finally implemented to obtain an initially calibrated PPF of 0.9 resulting in a porosity of 47.5 %, a bulk density of 1283 kg/m^3, a bulk stiffness of 2.733 MN/m, an angle of repose of 39° and finally normal contact forces of 353.3 N and 102.9 N on the bottom and side walls, respectively. Both the initially calibrated particle density and the PPF were then implemented into the models, after which the simulations were repeated for 5 critical damping ratio's (CDR) ranging between 0 and 1.0. All the bulk responses, excluding the bulk stiffness were then considered in order to calibrate the CDR at a value of 0.275, which

resulted in a porosity of 46.5 %, a bulk density of 1313.3 kg/m^3, an angle of repose of 36.9° and finally normal contact forces of 359.5 N and 107.2 N on the bottom and side walls, respectively.

The following micro property was the particle to wall friction (PWF), which could be calibrated in the same manner as the CDR by considering all the bulk responses except the bulk stiffness. Once again this was purely due to the results form the sensitivity study which revealed that the bulk stiffness is not significantly affected by the PWF. An initially calibrated PWF of 0.85 was finally obtained and resulted in a porosity of 47.3 %, a bulk density of 1318.7 kg/m^3, an angle of repose of 36.1° and finally normal contact forces of 358.3 N and 109 N on the bottom and side walls, respectively.

The only un-calibrated micro property left was the particle stiffness, which could be calibrated against the bulk stiffness and normal contact forces by simulating 5 different particle stiffness' ranging from 0.172 MN/m to 9 MN/m. This resulted in an initially calibrated particle stiffness of 0.62 MN/m, which lead to the bulk responses shown in Table 4.3. Table 4.3 is a summary of the results from the first iteration of the calibration process and it is clear that even after just one iteration the relative errors associated with the numerically obtained bulk responses decreased significantly from those corresponding to the un-calibrated case shown in Table 4.2.

Table 4.3: Bulk responses from calibrated micro properties

Bulk responses	**Experimental**	**Numerical**	**% Variation**
Porosity (%)	48.0	46.8	2.55
Bulk density (kg/m^3)	1357	1311	3.38
Bulk stiffness (MN/m)	1.435	1.555	8.4
Angle of repose (°)	37.0	35.6	3.82
Normal contact force on bottom wall (N)	340	371	9
Normal contact force on side wall (N)	105	111	5.3

One could therefore repeat the process several times until the calibrated micro properties converge, which would ultimately result in an optimum set of micro properties. However, this would require numerous additional and time consuming simulations and since the relative errors for all the bulk responses were under 10 %, the calibration process was deemed finished. The calibrated micro properties summarized in Table 4.4 would therefore be implemented for the rest of the simulations conducted for this research.

Table 4.4: Calibrated micro properties

Micro properties	Value
Clump accuracy (Number of spheres per clump)	10
Shape and size distribution	see Table A.1
Particle to particle friction	0.9
Particle density (kg/m^3)	1610
Critical (viscous) damping ratio	0.23
Particle to wall friction	0.85
Particle stiffness (MN/m)	0.62

4.5. Model validation

In order to demonstrate the robustness of the calibrated micro properties, a separate validation study was conducted by simulating particle discharge from a hopper and comparing the results to laboratory experiments. The experimental hopper contained a rectangular outlet with two horizontal trapdoors, which could be pulled apart in order to control the outlet size (Figure 4.7).

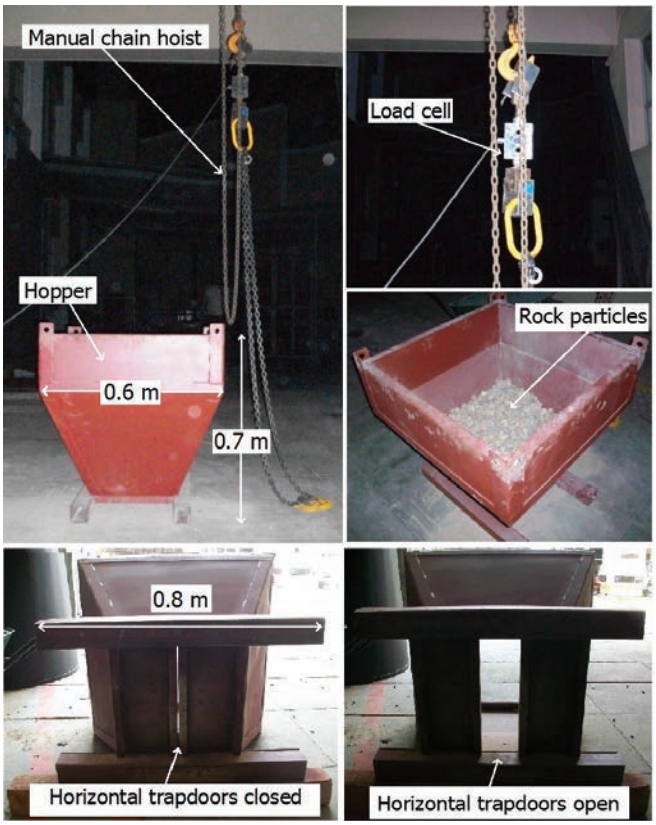

Figure 4.7: Experimental hopper used for model validation

The hopper was filled with approximately 122 kg of rock particles to ensure sufficient data could be collected during the experiments as well as to reduce the computational intensity of the numerical simulations. Once the hopper was filled, it was lifted to a height of 1 m through the aid of a manual chain hoist, which was connect to the hopper through a 50 kN HBM S9 load cell in order to measure the discharge rate. Three outlet sizes were considered by manually pulling the trapdoors 0.15 m, 0.25 m and 0.40 m apart and each scenario was repeated 3 times to ensure repeatability.

The average numerical and experimental discharge rates for an outlet opening of 0.15 m are shown in Figure 4.8. It can be seen that the calibrated micro properties did indeed result in an accurate discharge rate, since there was a good correlation between the numerical and experimental results. It should be noted that the hopper did not fully empty, since there was some material build up against the inside walls. The experimental results also showed some oscillating behaviour just after the trapdoors were opened, since the entire assembly resembles a suspended spring-mass system. In other words, the chain and load cell section acts as a displaced spring due to the weight of the hopper and rock particles. When the trapdoors are then opened the sudden reduction in the weight causes the spring (load cell and chain assembly) to displace upwards, after which gravity takes over to pull the hopper and therefore also the spring, down again. The process repeats itself resulting in the oscillations seen in the measured data, but each time the deflections become smaller and smaller, until the effect is finally damped out.

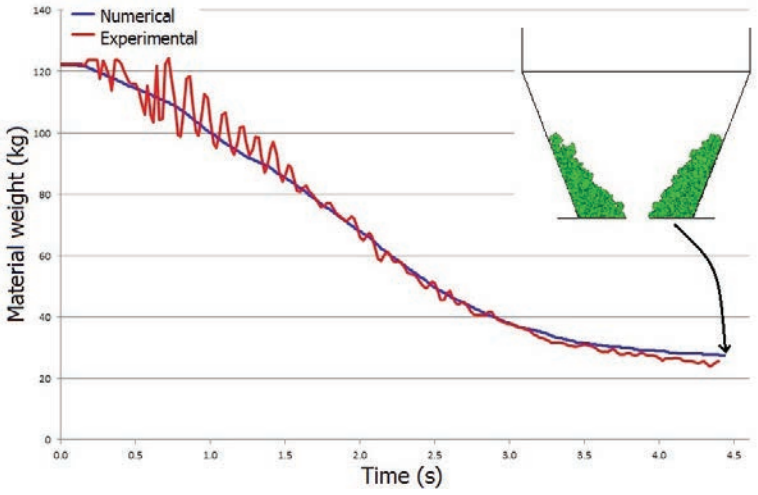

Figure 4.8: Numerical and experimental discharge rates for an outlet opening of 0.15 m

The numerical discharge rate for an outlet opening of 0.25 m also correlated well to that of the experimental results, as shown in Figure 4.9 and similar

to the 0.15 m case, the hopper did not fully empty due to material build up at the inside walls. Some external noise resulting from the spring-mass effect were once again present in the experimental data. Finally, for an outlet opening corresponding to 0.4 m the numerical and experimental results once again showed a good correlation as can be seen in Figure 4.10. Some external noise resulting from the spring-mass effect could be observed, similar to the previous two cases, but since the outlet was fully open no material build up could occur.

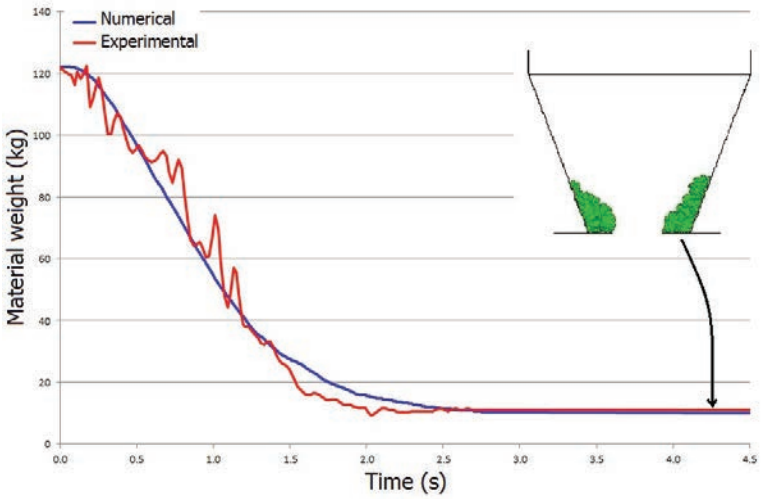

Figure 4.9: Numerical and experimental discharge rates for an outlet opening of 0.25 m

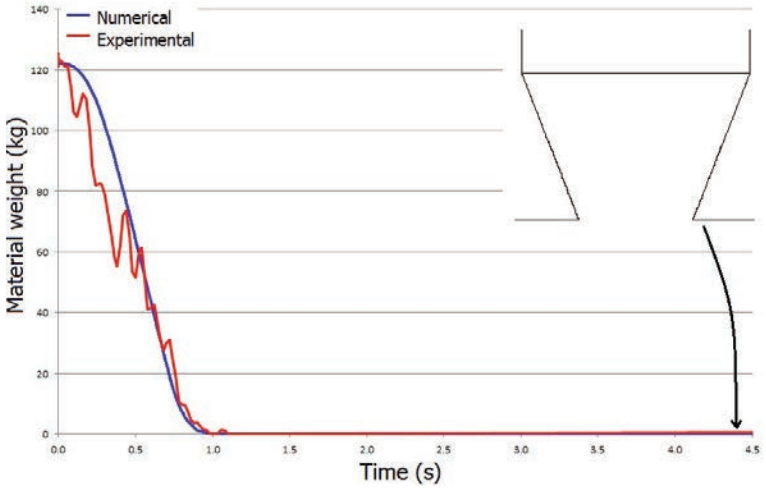

Figure 4.10: Numerical and experimental discharge rates for an outlet opening of 0.4 m

Even though there were some local variations between the numerical and experimental results, especially for the 0.4 m case where the discharge occurred in less than a second, the overall discharge rates for all the outlet openings were indeed accurate. Thus, from a practical perspective the numerical models did provide satisfactory results, which means that the selected set of input parameters are indeed robust and can therefore be implemented for various other numerical investigations.

5. DEM modelling of rock beds

5.1. Introduction

The second part of this research is aimed at the implementation of the developed models in order to investigate various aspects associated with packed rock beds, which are too impractical, expensive or impossible to achieve through actual experimental work. The first section focusses on the possibility of constructing self-supporting tunnels within packed rock beds to potentially improve the flow characteristics and high pressure drop factors commonly associated with such beds.

According to Schmidt and Willmott (1981) one of the main drawbacks of using packed beds for thermal storage applications is related to the large amount of energy required to pump the heat transfer fluid (air) through the bed, during the thermal charging and discharging cycles. It is therefore crucial to design such systems with the aim to reduce the pressure drop and therefore improve the potential of packed rock beds to be used as effective thermal storage systems. Numerous research as been done in this area such as the experimental studies conducted by Sign et al. on the effect of the particle shape and bed void fraction as well as the work done by Sagara and Nakahara (1991) on the effect of the particle size. However, this research is specifically interested in the construction of channels/tunnels within the bed to guide and distribute the airflow evenly through the bed, while reducing the pressure drop (Allen, 2010).

The problem with the proposed solution is that the tunnels would have to be able to withstand high thermal cycles (temperatures near 500 °C) without corroding, rusting or fracturing (Allen, 2010). This could have a significant effect on both the investment cost, since expensive materials would have to be used to construct the tunnels, as well as the operational and maintenance cost if the damaged sections have to be repaired or replaced. In an attempt to overcome this Kröger (2011) proposed the possibility of implementing self-supporting tunnels as an alternative method to implement the required tunnel network.

With self-supporting it is implied that the tunnels would be constructed entirely out of the rocks, without any adhesive materials or supporting structures and would therefore not be subject to mechanical degradation during operation. However, this is based on the assumption that the rocks themselves will be able to withstand the high thermal cycles without degrading. Allen (2010) performed a preliminary thermal mechanical stress analysis on possible rock candidates suitable for thermal storage applications and obtained some promising results. However, since this is outside the scope of this research it is assumed that the rock particles under investigation would be able to withstand the induced mechanical and thermal stresses without any degradation.

In order to study the potential of constructing self-supporting tunnels in rock beds, two very simple tunnel construction approaches were adopted. The one was to place a tube with a shape and size corresponding to the desired tunnel geometry, at the required location within the containment vessel, after which the rock particles are introduced and allowed to settle under gravity. The idea was that the tube would induce the formation of stable arches in the surrounding area, which would act as a naturally formed support structure once the tube is removed. Alternatively, the second approach resembled an actual excavation process were the particles would be removed from the bed with the aim to possibly induce the formation of stable tunnels.

With this in mind, only horizontal and vertical scenarios were considered, since they would typically be the most common to implemented and it was left for future research to investigate various other possible tunnel orientations. In addition, since practical size beds cannot be modelled at this stage and numerous different scenarios would have to be simulated and analysed, it was decided to mainly focus on relatively small scale beds. The conditions and scenarios considered for this research are therefore purely to identify some key aspects and draw some preliminary conclusions surrounding the dynamics of self-supporting tunnels in rock beds, with the overall aim to form a basis onto which future research can be built.

The remaining two sections on the other hand form part of separate research topics being conducted by other members of the STERG.

5.2. The potential of self-supporting horizontal tunnels

5.2.1. Bed layout 1

The baseline steps followed to model and study the horizontal tunnels considered for this research can be summarized as follows (Figure 5.1):

i) Create the system boundaries. For the purpose of this study a square container (0.3 x 0.3 x 0.3 m) similar to the one modelled and described in Section 3.2, was used, since it would not only allow numerous scenarios to be modelled within a practical time frame, but some of the results could even be validated by conducting the appropriate experiments.

ii) Place the desired tube in the middle of any two opposite side walls, at a height of 0.1 m measured from the container floor to the centre of the tube and such that it would stretch through the entire bed.

iii) Introduce the rock particles (shape and size distribution from Table A.1) through the rainfall method and allow them to settle under gravity.

iv) Remove the tube (a constant speed of 0.5 m/s was used throughout the study) and record the status of the resulting self-supporting tunnel with respect to its initial visibility, as well as the approximate position and number of collapsed particles. The state of initial visibility was based on visual judgement and could be categorized as being either fully visible, partially visible or zero visible. Furthermore, remove any collapsed particles from the tunnel and allow the bed to reach steady state.

v) The second tunnelling approach can then be performed by identifying and removing particles with centre points falling within a specified excavation zone, resembling a rectangular tube. For this study, the excavation zone had a height of 0.1 m, stretching upwards from the bottom of the container, an initial width of 0.015 m and it was located in the middle of two opposite side walls, stretching through the entire length of the bed. Nevertheless, once the particles are removed the bed is allowed to reach steady state, during which any additionally collapsed particles are removed from the excavation zone. The state of the excavated tunnel is then recorded, after which the width of the excavation zone is increased by 0.015 m and the process repeated, for several more steps. In addition, the following aspects should be highlighted with regard to the excavation process.

- The height of the excavation zone is kept constant to reduce the number of variables influencing the final results.
- Instead of individually removing the particles from the side or allowing them to discharge through small trapdoors at the bottom of the container, which would resemble practical excavation methods more closely, all the applicable particles are removed instantaneously. This was simply done to reduce the run times associated with the models, since each scenario would have to be repeated several times to ensure repeatability.

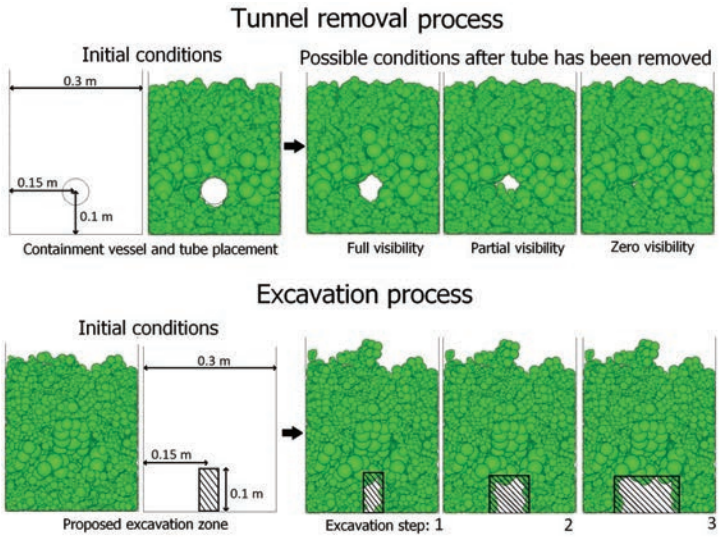

Figure 5.1: Steps followed to model and study the horizontal self-supporting tunnels under investigation (Note that the figures presented, correspond to bed layout 3 and not 1)

With the above steps in mind, three reference tubes were considered with diameters corresponding to 0.06 m (double the average hydraulic particle diameter), 0.03 m (equal to the average hydraulic particle diameter) and 0.015 m (halve the average hydraulic particle diameter), and for each tube five different rock beds were modelled, to ensure repeatability. The aim was to see if relatively stable tunnels could be obtained and at the same time to identify the approximate range of tunnel dimensions achievable. It should be noted that with "relatively stable" it is implied that the stability of the tunnel has not been tested against externally applied forces or even disturbances caused by thermal cycling.

Nevertheless, once the tubes were removed it was observed that in most instances the resulting tunnels corresponded to a state of zero initial visibility, with only one or two tunnels being partially visible (Figure 5.2). On the other

hand the location at which the particles collapsed also varied, with no noticeable trend, however the number of collapsed particles did seem to increase slightly as the tube diameter increased. The initially collapsed particles were then removed, after which it was observed that for some instances the resulting tunnels were still relatively stable, whereas others completely collapsed. It should be noted that for the tunnels constructed with the tube diameter of 0.015 m, no collapsed particles were removed, since from a practical perspective this is not possible. Furthermore, no distinction could be made between the different tube diameters considered, since all of them responded in a very random and unpredictable way. Finally, similar results were obtained for all the different beds modelled and the results were validated through experimental work (Appendix D). The observations made therefore clearly indicate that the specified conditions are not suitable for the formation of self-supporting tunnels.

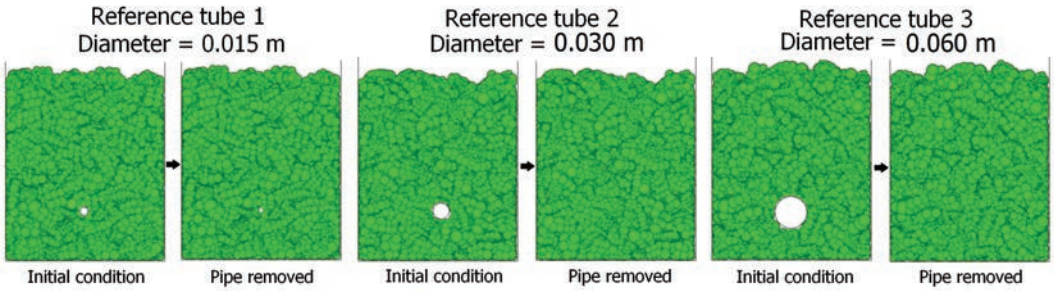

Figure 5.2: Horizontal tunnels resulting from the removal of the reference tubes

The excavation process was performed next, during which it was observed that for all the beds modelled the excavated tunnels would simply collapse and as the excavation continued the packing height would gradually decrease, until most of the particles had been removed (Figure 5.3). There were one or two instances where partial segments of an excavated tunnel remained (step 2), but these tunnels were very unstable and occurred at random instances during the excavation process. Similar results were obtained for all the beds considered and it can therefore be concluded that the proposed tunnelling method would not necessarily result in relatively stable self-supporting tunnels, suitable for practical applications.

In addition, during the experimental work, it was observed that most of the rocks comprising the tunnels were relatively loose, which resulted from the complex nature in which forces are transmitted within packed beds (Figure 5.4). In some cases the contact force networks are distributed randomly throughout the bed, resulting in unfavourable conditions for the formation of self-supporting tunnels. In other instances, arc formation occurs where the

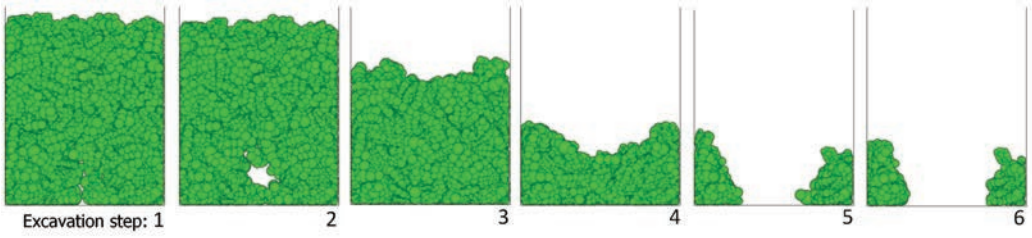

Figure 5.3: Horizontal tunnels resulting from the consecutive steps of the excavation process

particles underneath the arc are relative loose and can be removed to form a tunnel. However, if particles within the arc itself are removed the tunnel becomes unstable and can partially collapse (steps 1 to 2) or completely collapse (steps 2 to 3) if sufficient particles were removed (Figure 5.4).

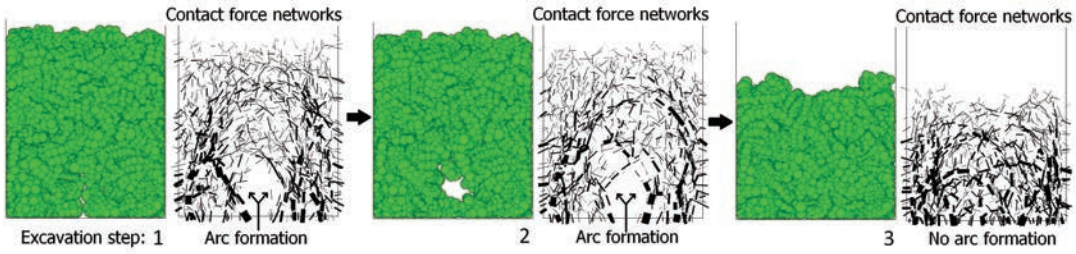

Figure 5.4: Contact force networks resulting from the excavation process

A study was therefore conducted by applying a compression force of 2500 N through a flat plate at the top of the rock beds (Figure 5.5) with the intention to reduce the number of loose particles within the tunnels, such that the tunnels could potentially become more stable. The results however, showed that the applied compression add no significant effect on the beds' ability to form self-supporting tunnels, since relatively similar results were obtained as compared to the uncompressed beds. This resulted from the fact that the compression force did not transmit evenly through the bed, but instead transmitted through several force chain networks distributed randomly throughout the bed. Only the rock particle comprising the contact force networks were therefore more compacted, while the rest of the particles remained relatively loose. This was verified through experimental work (Appendix D), during which it was observed that the rock particles within the tunnels were still relatively loose even when a compression force was applied. It should be noted that the experimental work only considered the tunnels resulting from the tube removal process.

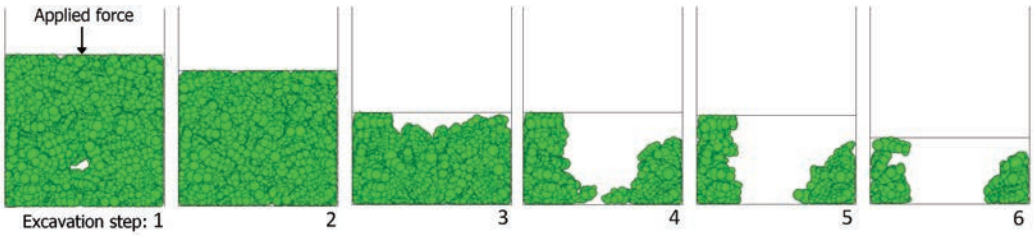

Figure 5.5: Horizontal tunnels resulting from an applied compression force, during the consecutive steps of the excavation process during

5.2.2. Bed layout 2

Since the previous conditions were unsuitable for the formation of self-supporting tunnels it was decided to increase the original particle size distribution (Table A.1) with a factor of 3.2 , in an attempt to obtain better results. The larger particle size distribution was based on actual rock samples, such that the required experimental work could be conducted and for the remainder of this study they would simply be referred to as the larger particles, whereas those modelled with the original size distribution would be referred to as the smaller particles.

The necessary steps were then performed with the larger rock particles, during which it was observed that there were tunnels which were partially visible or in one or two cases even fully visible (Figure 5.6). Nevertheless, most of the tunnels, specifically the ones constructed with the two larger tube diameters, still resulted in a state of zero initial visibility. On the other hand, the number of collapsed particles also seemed to increase as the tube diameter increased, however, relatively fewer particles collapsed as compared to the previous case. In addition, unlike for the previous bed layout, the initially collapsed particles were not removed to gain further insight into the relative stability of the respective tunnels, since this was not possible from a practical perspective. Instead, an additional set of simulations were conducted for a tube diameter of 0.09 m, such that the particles could be removed. Nevertheless, the results were once again too random and unpredictable, since some tunnels were relatively stable, while others continued to collapse.

The observations were also validated through experimental work, during which it was observed that the particles in the area surrounding the tunnels were slightly more compact with fewer loose particles present. A slight distinction could also be made between the different tube diameters considered, with the smaller tube resulting in more consistent results as compared to the larger tubes, but from a practical perspective the specified conditions were still regarded as being unsuitable for the formation of self-supporting tunnels.

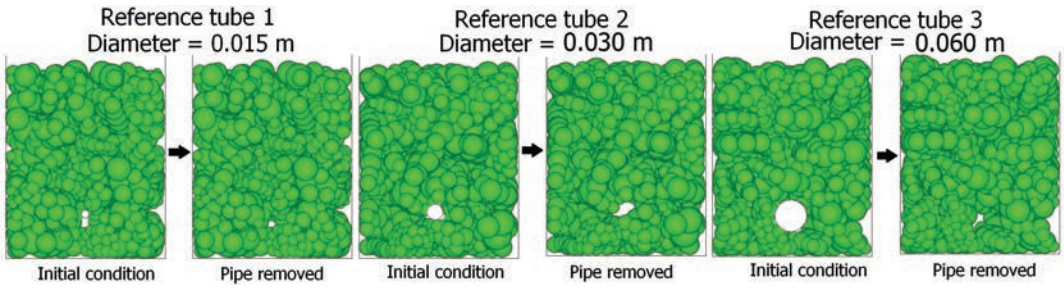

Figure 5.6: Horizontal tunnels resulting from the removal of the reference tubes for the larger particles

On the other hand, during the excavation process (Figure 5.7), it was observed that a significant number of relatively stable tunnels were obtained (steps 2 to 5), as compared to the previous case where the tunnels continuously collapsed. However, it should be noted that some of these tunnels only formed after a substantial number of particles collapsed, which was clearly visible in the sudden reduction in the bed's height as shown in steps 3 to 5. Nonetheless, similar results were obtained for all the different cases considered, with some beds capable of supporting relatively large self-supporting tunnels, whereas for other instances the tunnels collapsed to various degrees and at random steps during the excavation process.

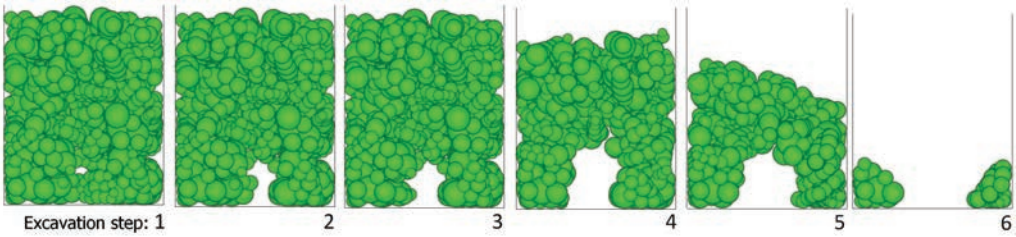

Figure 5.7: Horizontal tunnels resulting from the consecutive steps of the excavation process for the larger particles

Applying a constant compression force also had no consistent effect on the tunnel formation (Figure 5.8). For some instances the applied force aided the excavation process, since larger tunnel dimension could be achieved, compared to the uncompressed case, but in other instances the applied force had a negative impact on the tunnel formation. The experimental work once again showed that similar to the beds with the smaller particles, the compression force did not compress the bed evenly. Instead the particles in the force chain networks carried most of the compression force, leaving the rest of the particles relatively uninfluenced. It was finally concluded that even though a significant

number of relatively stable tunnels could be constructed under confined compression (hereafter regarded as being mechanically stable), there was still too much randomness and inconsistency associated with the results, in order for the conditions to be considered as suitable for self-supporting tunnels.

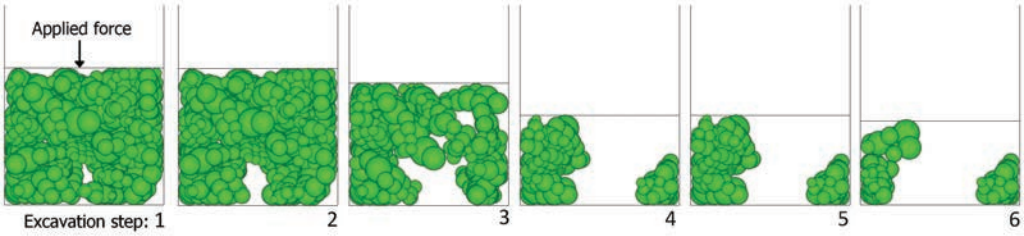

Figure 5.8: Horizontal tunnels resulting from an applied compression force, during the consecutive steps of the excavation process for the larger particles

5.2.3. Bed layout 3

In a final attempt to identify possible conditions suitable for the formation of self-supporting tunnels, it was decided to use the rock bed layout presented in Figure 5.9, which consisted out of three different particle layers, each with an approximate height of 0.1 m. The specified particle arrangement was selected specifically with the aim that some of the smaller particles in the top layers, would fall in the void spaces between the larger particles, potentially increasing the particle interlocking. In theory, the increased interlocking would then significantly reduce the number of loose particles associated with the middle rock layer, which according to the observation made during the previous investigation, was one of the major reasons why stable tunnels could not be constructed. Nevertheless, the investigation could be conducted by placing the reference tubes directly beneath the middle rock layer, during the construction of the bed, whereas the excavation process could simply be repeated as for the previous cases.

The results obtained by removing the respective tubes showed a significant improvement and were more consistent, as compared to the previous scenarios (Figure 5.10). The tunnels resulting from the 0.015 m tubes for instance were all fully visible, while most of the remainder of the tunnels were either also fully visible or partially visible, with only a few cases of zero visibility. Furthermore, the collapsed particles typically corresponded to some of the smaller particles from the upper layer, which suggests that an insufficient number of large particles were used to form the second layer. Care should therefore be taken during the bed construction, to ensure that the smaller rock particles fall effectively between the larger particles, without reaching the tubes. The

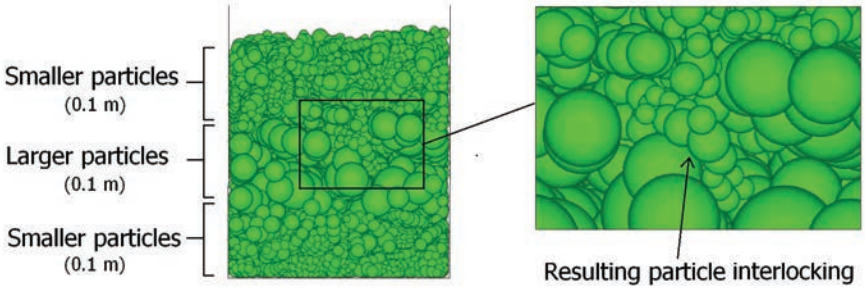

Figure 5.9: Proposed particle arrangement to improve conditions for the formation of self-supporting horizontal tunnels

initially collapsed particles were then removed after which it was observed that all the tunnels remained relatively stable. However, since there were instances where some of the bigger rocks collapsed, which could be impossible to remove in practice, it seemed that for the three different tube diameters considered only the 0.015 m case has the potential to form relatively stable tunnels. As an additional study the simulations were also repeated for tube diameters of 0.09 m and 0,12 m, respectively, such that any collapsed particles could be removed. It was observed that all the tunnels resulting from the 0.09 m tubes remained relatively stable, while those from the 0.12 m tubes displayed the same random and inconsistent behaviour as the previous scenarios. It was therefore concluded that the specified conditions did displayed the potential to consistently form relatively stable tunnels, but the exact tunnel dimensions achievable, are still not known.

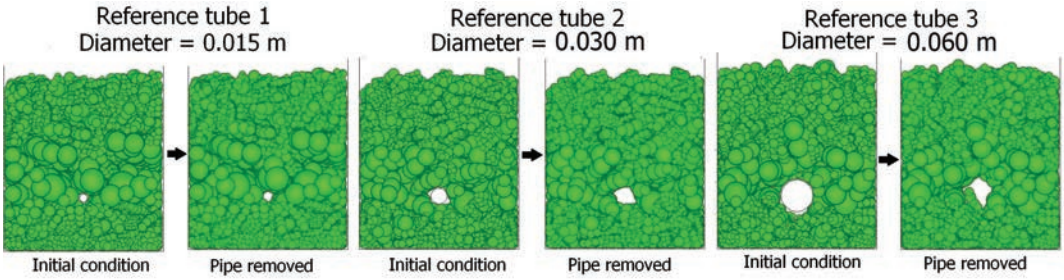

Figure 5.10: Horizontal tunnels resulting from the removal of the reference tubes for the proposed bed layout

Reasonably satisfactory results were also obtained from the excavation process, as shown in Figures 5.11 and E.1 (see Appendix E). Not only did relatively stable tunnels continue to form as the excavation process progressed (steps 2 to 4), but there was also a noticeable consistency in the shapes of the tunnels.

This was a clear indication that no significant particle collapse occurred during the excavation process. Instead, the width of the tunnels simply increased as the excavation zone increased, until the tunnel finally completely collapsed (steps 4 to 5). This was also evident in the bed height, which remained constant up to the final stages of the excavation process. It could therefore be concluded that relatively stable tunnels could also be formed through the proposed excavation process, but similar to the previous case the exact tunnel dimension were not known.

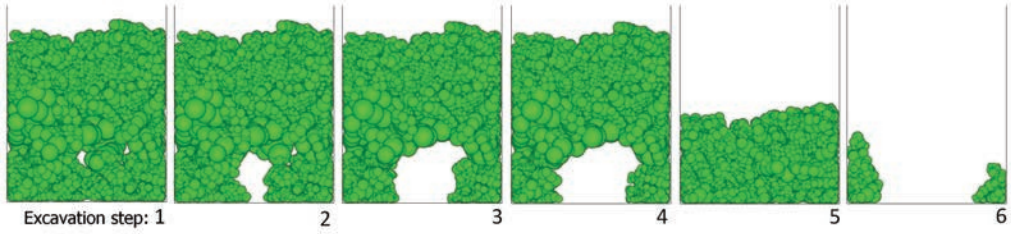

Figure 5.11: Horizontal tunnels resulting from the consecutive steps of the excavation process for the proposed bed layout

The effect of applying a compression forces was finally investigated, after which it was observed that in some instances larger tunnels could be formed (Figures 5.12 and E.2), since the excavation process continued for one or two additional steps before the tunnel collapsed (step 5 to 6). However, due to the randomness in which forces are transmitted through the beds one could not assume that larger tunnels would necessarily form if a compression force is applied. Instead, some additional research would first have to be conducted. Nevertheless, the added compression forces did not results in any additional particle collapse other that those corresponding to the final stages of the excavation process, which suggest that the respective tunnels are mechanically stable as well.

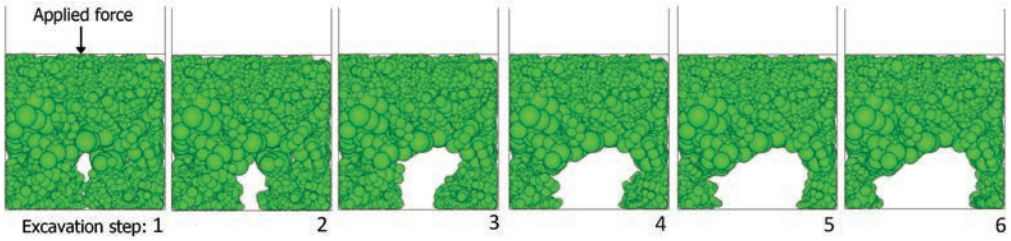

Figure 5.12: Horizontal tunnels resulting from an applied compression force, during the consecutive steps of the excavation process for the proposed bed layout

As a final investigation the stability of the tunnels were also tested under the conditions of thermal cycling, since the disturbances resulting from the continuous expansion and shrinkage of particles could be sufficient to induce

tunnel collapse. However, it should be noted that for practical reasons only a simplified thermal cycling process could be reproduced with the DEM, as described in Appendix F, but it is left for future research to develop more accurate and reliable models. The approach adopted here is therefore purely to gain some preliminary results into the stability of the proposed tunnels during thermal cycling. The five largest mechanically stable tunnels obtained with the excavation process were therefore thermally cycled, by conducting five consecutive charging and discharging phases, after which the state of the tunnels were analysed. It was observed that even though there were one or two instances of additional particle collapse, which could all be removed, all the tunnels remained stable (Figures 5.13 and E.3).

The respective contact force networks are also included, where the effect of the respective charging and discharging phases are clearly visible. During the charging phase the magnitude of the contact forces increase significantly, as a result of the particles expanding, whereas for the discharge phase the particles decrease in size, resulting in smaller contact forces. It should be noted that the magnitude of the contact forces at the end of the discharged phase are still higher than those corresponding to the initial conditions, since not all of the heat was removed during the discharge phase. Nevertheless, it can finally be concluded that the proposed tunnels do show the potential to be remain stable even during thermal cycling (hereafter after referred to as being thermally stable).

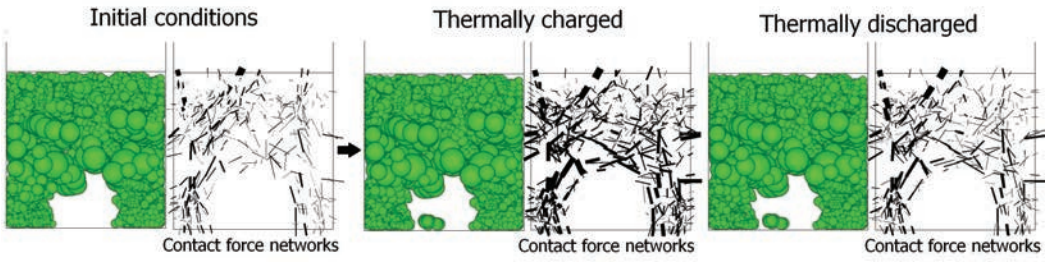

Figure 5.13: The effect of thermal cycling on the stability of the proposed horizontal tunnels

5.3. The potential of self-supporting vertical tunnels

5.3.1. Bed layout 1

The steps followed to model the vertical tunnels were similar to those used for the horizontal tunnels, but with the following adjustments (Figure 5.14):

- Instead of placing the tubes parallel to the the bottom of the container, they were placed at the centre of the the container, perpendicular to the container floor.
- The initial excavation zone (resembling a square tube) was located at the centre of the container, with sides equal to 0.015 m and a height stretching through the entire length of the bed. However, during the excavation process the sides were also increased incrementally by 0.015 m, similar to the horizontal case.

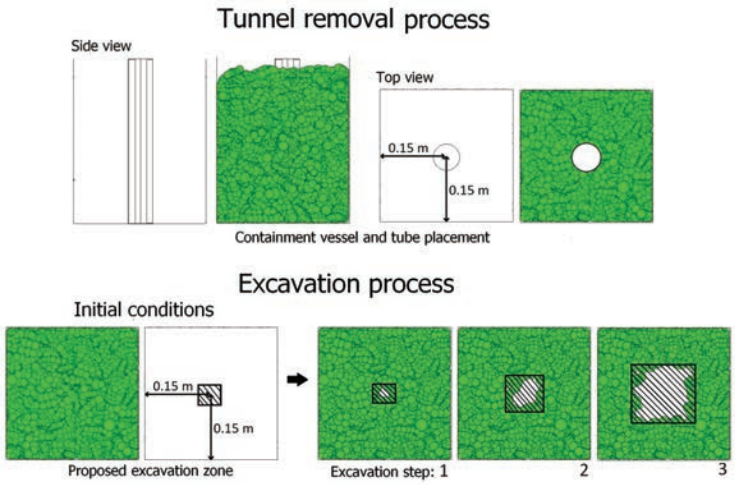

Figure 5.14: Steps followed to model and study the vertical self-supporting tunnels under investigation

Once the reference tubes were removed from the various packed beds modelled, it was observed that most of the resulting tunnels were either partially visible or they corresponded to a state of zero visibility (Figure 5.15), with only one or two tunnels being fully visible.

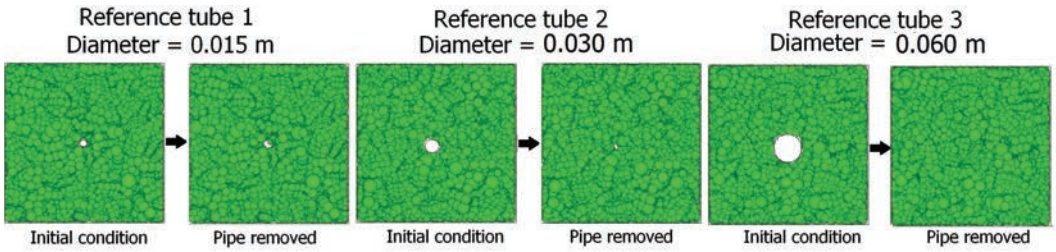

Figure 5.15: Vertical tunnels resulting from the removal of the reference tubes

On the other hand, the location of the collapsed particles varied between the bottom, middle and top section of the tunnels, while the number of collapsed particles seemed to increase as the tube diameter increased. There were however, no consistency in the number of collapsed particles for the five beds modelled for each tube and even after the collapsed particles were removed (excluding the ones resulting form the 0.015 m tubes, due to practical reasons), the results were still very random and unpredictable. Similar observations were made during the experimental work and it was therefore concluded that the specified conditions are not suitable for the formation of self-supporting tunnels, as was the case for the horizontal tunnels.

As expected, the tunnels resulting from the excavation process also continuously collapsed, until all the particles were more or less removed (Figure 5.16). The misleading results displayed in the top view (steps 4 to 6) should therefore not be mistaken as tunnels, instead, they correspond to stable angles of repose forming against the inside walls of the container. Nevertheless, there were instances, where partially visible tunnels could be observed (steps 1 and 2), but they occurred at random and only resulted from the first, and in one or two other cases, the second steps of the excavation process.

The random and peculiar behaviour could once again most likely be related to the way in which arc formation occurs within packed beds (Figure 5.17). In some instances, the particle removal process resulted in suitable conditions for the formation of self-supporting tunnels (steps 1 and 2), since arches formed with the potential to resist any lateral forces resulting from the particles within the beds. On the other hand, when some of the particles comprising the arches were removed, the tunnels became unstable and simply collapsed (steps 2 to 3).

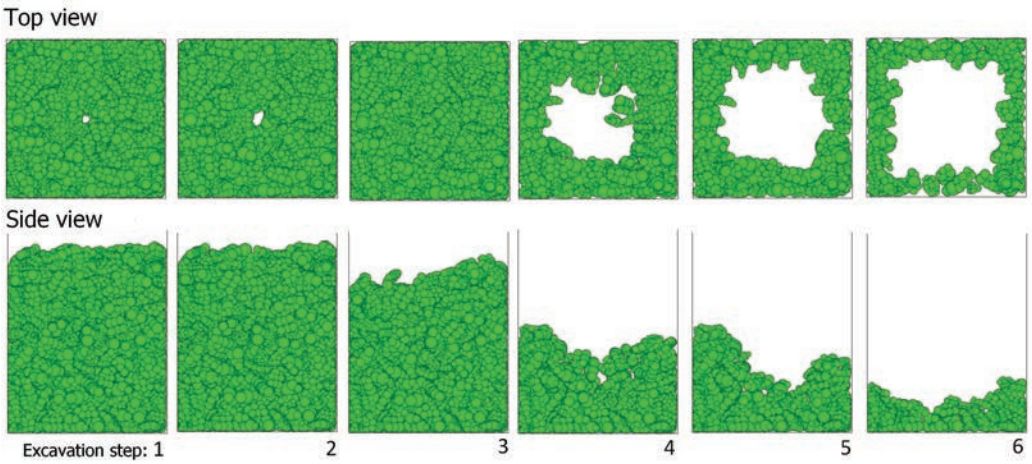

Figure 5.16: Vertical tunnels resulting from the consecutive steps of the excavation process

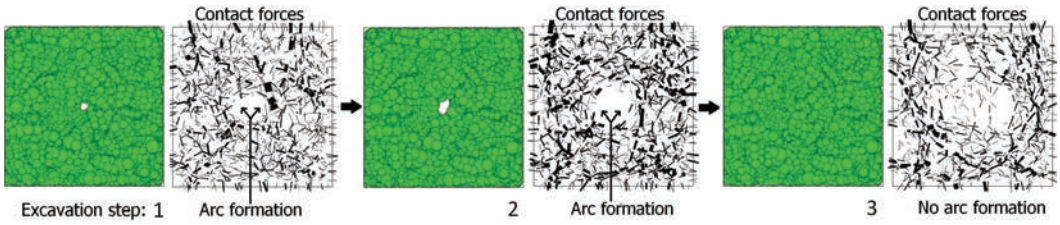

Figure 5.17: Contact force networks resulting from the excavation process

Applying a compression forces also had no consistent effect on the final results (Figure 5.18), since most of the tunnels were relatively uninfluenced. Even though there were one or two instances during which slightly larger tunnels were obtained (steps 1 to 2), as compared to the uncompressed case, the results were still too random and unreliable from a practical perspective.

5.3.2. Bed layout 2

Following the same procedure as for the horizontal case, attention then shifted to that of the larger rock particles, where the tunnels resulting from the removal of the reference tubes, showed a significant improvement compared to beds with the smaller particles (Figure 5.19). It was observed that the number of collapsed particles decreased, while at the same time more tunnels were fully or partially visible. The results were verified by conducting the appropriate experiments, but unsurprisingly due to the fact that a sufficient number of collapsed particles was still present and occurred for all the tube diameters

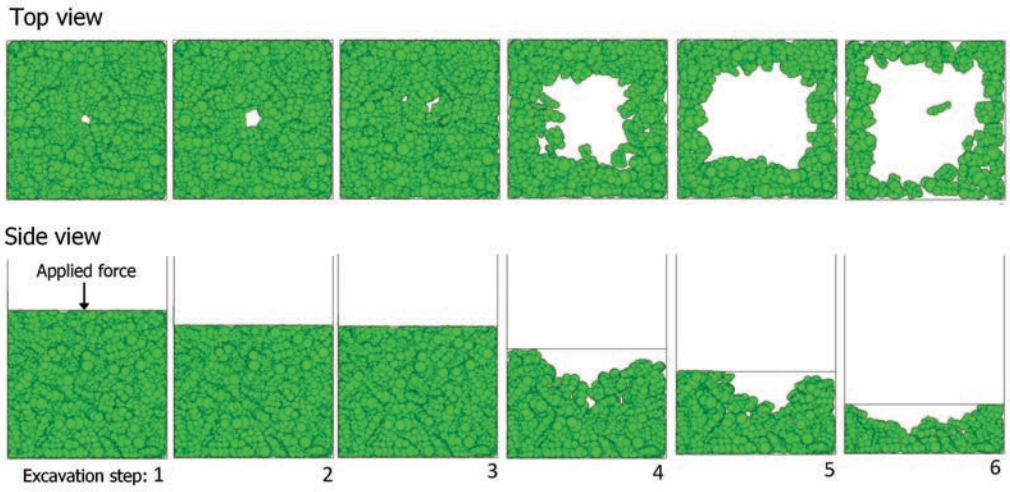

Figure 5.18: Vertical tunnels resulting from an applied compression force, during the consecutive steps of the excavation process

considered, the conditions were regarded as unsuitable for the formation of self-supporting tunnels.

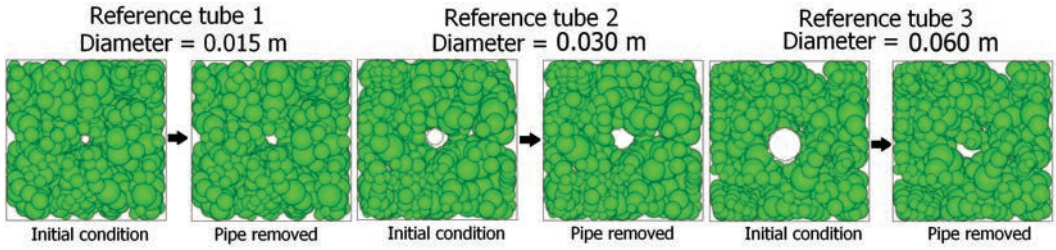

Figure 5.19: Vertical tunnels resulting from the removal of the reference tubes for the larger particles

The excavation process on the other hand, also gave rise to significantly more and larger stable tunnels, as compared to the beds with the smaller rock particle (Figure 5.20), however, they were once again some inconsistencies within the results. The most noticeable, corresponded to that of the respective tunnel shapes obtained, since for some instances there was a significant change in the shape of the tunnels (steps 2 to 3). This simply resulted from the fact that the particles are relatively large, compared to the tunnel dimensions, and the removal of only a single one could therefore significantly alter the shape of the tunnel.

Furthermore, one or two instances resulted in larger mechanically stable tunnels (Figure 5.21) when a constant compression force was applied (step 1), but

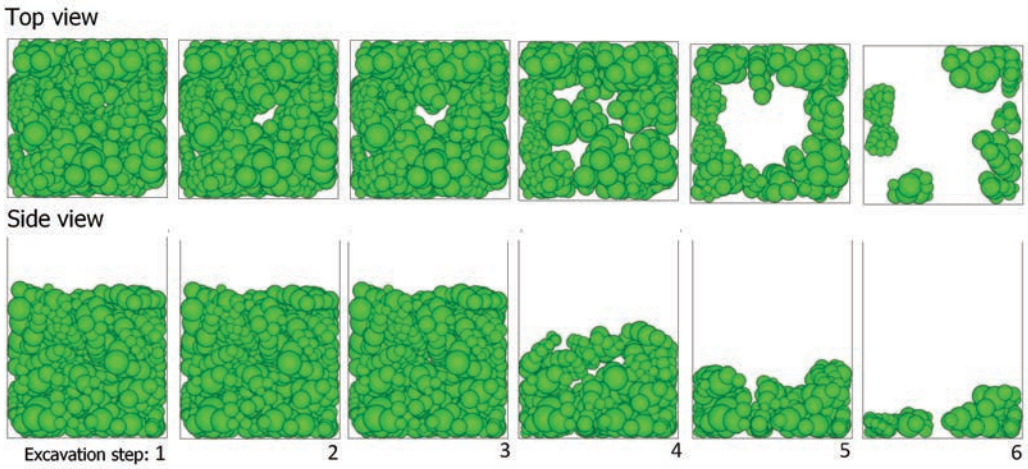

Figure 5.20: Vertical tunnels resulting from the consecutive steps of the excavation process for the larger particles

as was the case for all the previous scenarios, the effect was not consistent among all the different rock beds modelled. The larger particles were therefore regarded as being unsuitable for the formation of self-supporting tunnels, under the specified conditions.

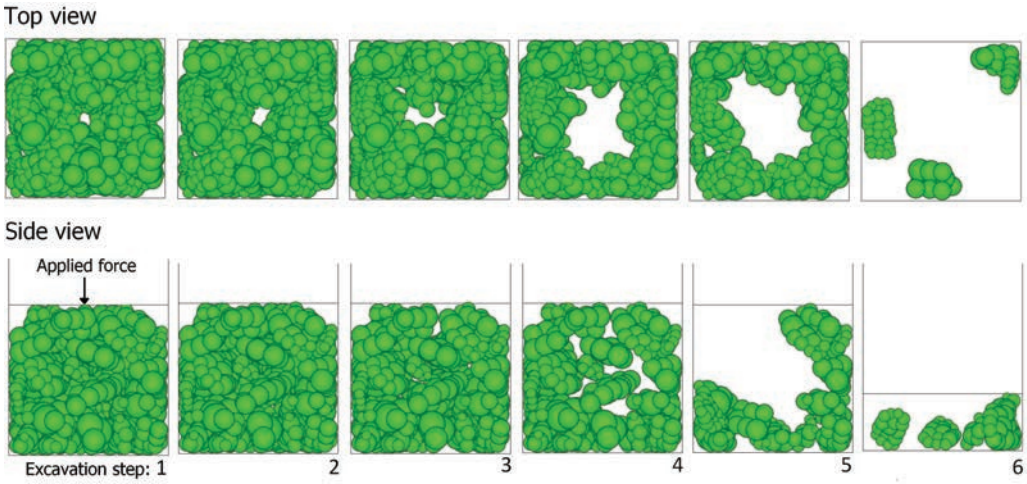

Figure 5.21: Vertical tunnels resulting from an applied compression force, during the consecutive steps of the excavation process for the larger particles

5.3.3. Bed layout 3

Since none of the above conditions resulted in satisfactory results, it was decided to increase the particle interlocking similar to the horizontal case, by

using the bed layout proposed in Figure 5.22. The bed could be constructed by allowing the large particles to settle at the centre of the container within a tube annulus, while the smaller particles are allowed to settled around the outside diameter of the tube annulus. The inner diameter then simply corresponds to the desired reference tube, whereas the outer diameter is selected accordingly to ensure that sufficient large particles could settled around the reference tube. Nevertheless, the outer diameter could then be removed, by carefully pulling it vertically upwards, to allow the smaller particles to displace into the voids spaces between the larger particles.

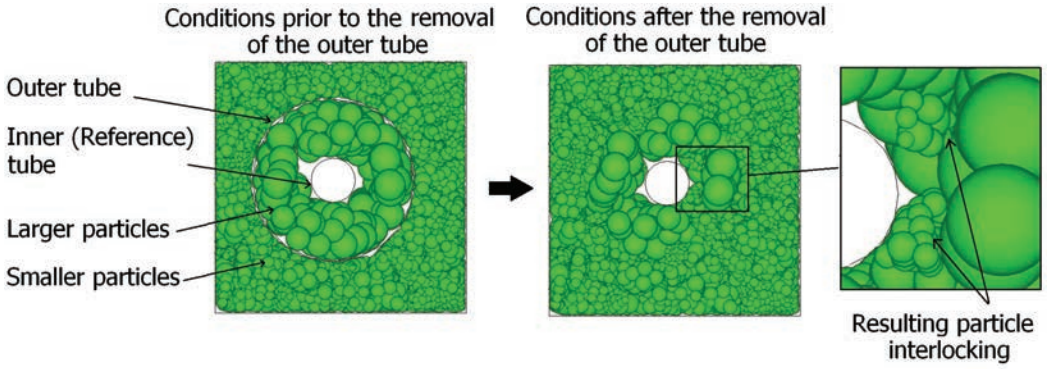

Figure 5.22: Proposed particle arrangement to improve the conditions for the formation of vertical self-supporting tunnels

The results obtained by removing the respective reference tubes showed a significant improvement and were more consistent, as compared to the previous scenarios (Figure 5.23). All the resulting tunnels for instance were mostly fully visible, with only a few being partially visible. Nevertheless, care should be taken during the bed construction to ensure that the smaller rock particles fall effectively between the larger particles, without reaching the tubes, since there were one or two instances were some of the smaller particles moved to within the tunnel, partially blocking it. This was also evident in the fact that some of the larger particles comprising the tunnels, shifted slightly inwards, which suggest that insufficient interlocking occurred between the respective smaller and larger particles. Similar observations were also made during the experimental work.

As an additional study the simulations were also repeated for tube diameters of 0.09 m and 0,12 m, respectively, to gain further insight into the maximum tunnel dimensions achievable (Figures 5.24 and E.4). It should be noted that for practical reasons the container dimensions had to be increased (0.4 x 0.4 x 0.3 m) to be able to perform the specified simulations, however, for visual purposes all the images were scaled to be the same size. During this process it was observed that relatively stable tunnels could be obtained from both the 0.09

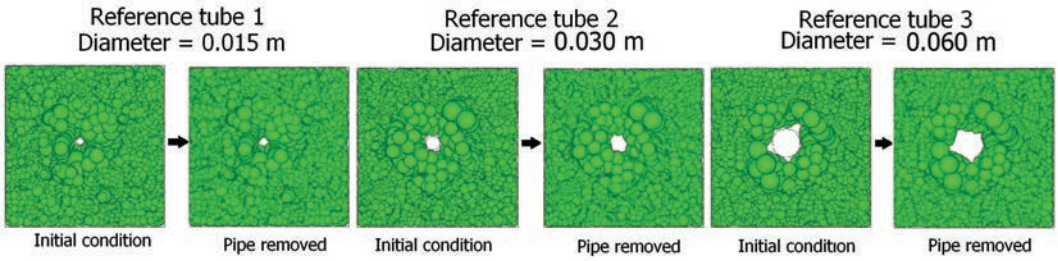

Figure 5.23: Vertical tunnels resulting from the removal of the reference tubes for the proposed bed layout

m and 0.12 m diameter tubes (step 4 and 5) and only a partial amount of particles collapsed, as is evident in the packing height which remained relatively constant. However, one of the tunnels resulting from the 0.12 m tubes did completely collapse, which implies that there is some uncertainty associated with the tunnels resulting from relatively large tube diameters.

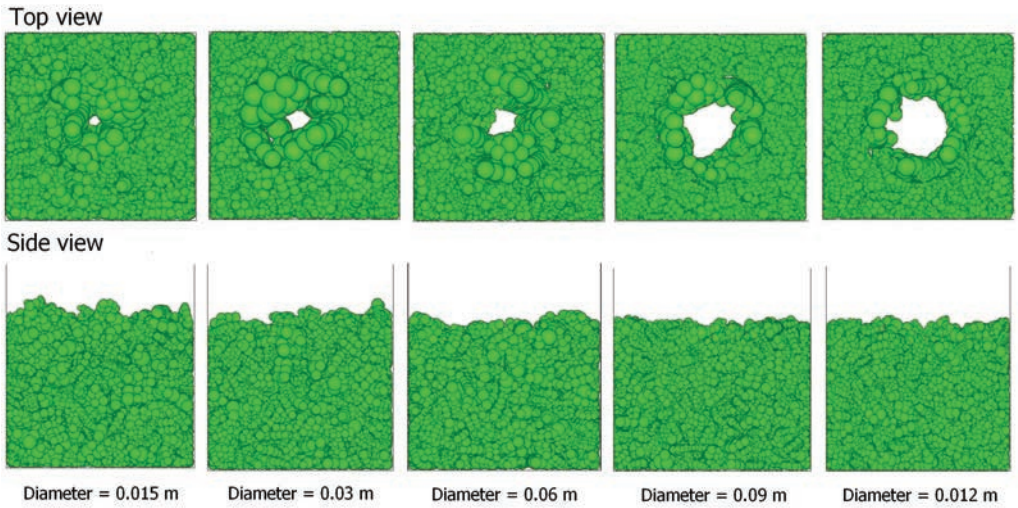

Figure 5.24: Vertical tunnels resulting from the consecutive steps of the excavation process for the proposed bed layout

Applying a compression forces also had no significant effect on the final results (Figures 5.25 and E.5), since no additional particle collapse occurred for most of the tunnels, especially the ones resulting from the reference tubes. Some of the larger tunnels on the other hand, did partially collapse, but after the collapsed particles were removed, the tunnels remained stable. It could therefore finally be concluded that the specified conditions did display the potential to consistently form mechanical stable tunnels, however the exact tunnel dimensions achievable, are still not known.

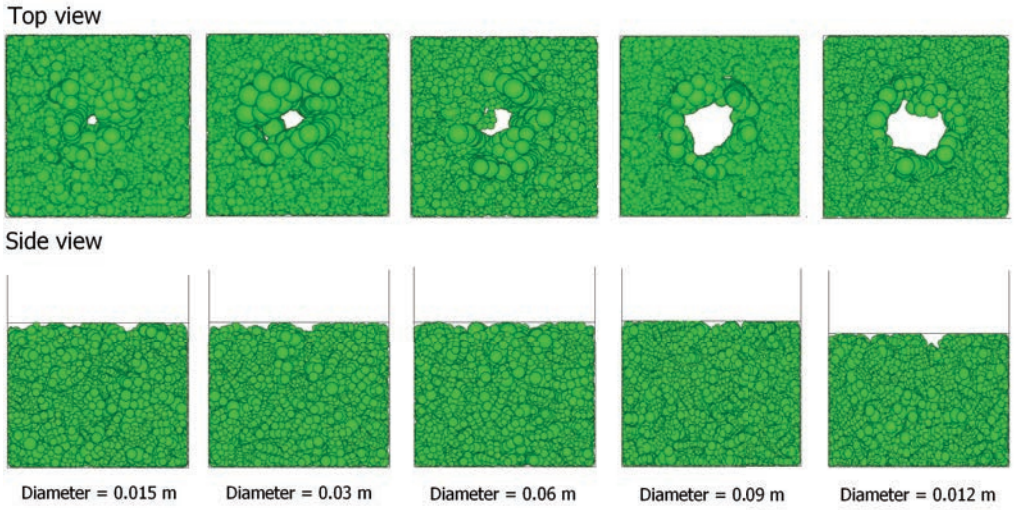

Figure 5.25: Vertical tunnels resulting from an applied compression force, during the consecutive steps of the excavation process during for the proposed bed layout

It should be noted, that unlike the horizontal case the excavation process could not be performed on the proposed bed layout, due to practical reasons and for that reason the thermal cycling analysis was performed on the five largest tunnels obtained through the tube removal process (Figures 5.26 and E.6). It was observed the even though there were instance were the tunnels completely collapsed, most of them remained thermally stable. One should also take into account that the five largest tunnels from the pipe removal process was selected for the thermal cycling analysis and if some of the smaller tunnels would have been used, possibly no tunnel collapse would have occurred. Nonetheless, it can finally be concluded that the vertical self-supporting tunnels showed the potential to remain stable during thermal cycling.

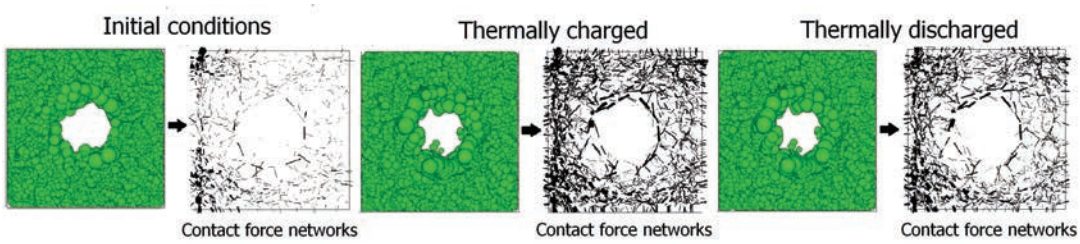

Figure 5.26: The effect of thermal cycling on the stability of the proposed vertical tunnels

5.4. Complementary work for CFD studies

5.4.1. Converting DEM models for use in CFD domain

According to Bai *et al.* (2009), the most traditional way to design packed beds for thermal storage applications is through a trail an error approach where critical variables such as the pressure drop and heat transfer characteristics are predicted by using empirical correlations. However, these correlations are mostly based on homogeneous assumptions and therefore local variations, which could have a significant influence, are not considered. Local changes in the porosity for instance, could lead to large variations in the predicted head loss along the bed, due to the variations in the velocity profile. Similarly, a small error in the porosity could also result in a significant error in the pressure drop predictions.

An alternative solution would therefore be to conduct specific pilot plant test, similar to the work conducted by Allen (2010), in order to modify the empirical correlations by changing their constants and input parameters until the desired results are obtained. The problem associated with such an approach is simply related to the time and resources required to conduct sufficient tests, especially if relatively large scale test are considered. In order to avoid these time consuming and expensive experimental approaches, three dimensional flow simulations can be performed. However, to be able to perform such a detailed CFD simulation on a packed bed, requires an accurate geometric model of the bed's packing structure. The most widely used method to obtain such a geometric model is by developing it with DEM and then to import the model into a suitable CFD preprocessor in order to create the mesh for the CFD calculations.

As mentioned before, this coupled DEM-CFD approach has been used by a number of researchers, but one crucial aspect which has not adequately been addressed is how the developed geometric models can be converted into the appropraite format such that they can be preprocessed for the CFD simulations. To overcome this issue, a method is proposed to reconstruct the geometric model in a computer aided design program, specifically the commercially available Autodesk Inventor Professional, such that it can be converted into a STEP file format suitable for most CFD preprocessors. This was achieved by making use of Autodesk Inventor's application programming interface (API) to create a program which could perform similar types of operations as when Autodesk Inventor is used interactively. One such operation is the simple process of drawing a circle with a specified radius and location and then to revolve the circle into a sphere. The advantage of performing this through the API is that the process can be performed automatically and be repeated

for several thousand spheres. The DEM models, consisting entirely of spheres could therefore easily be recreated in Autodesk Inventor and then exported as a STEP file (Figure 5.27).

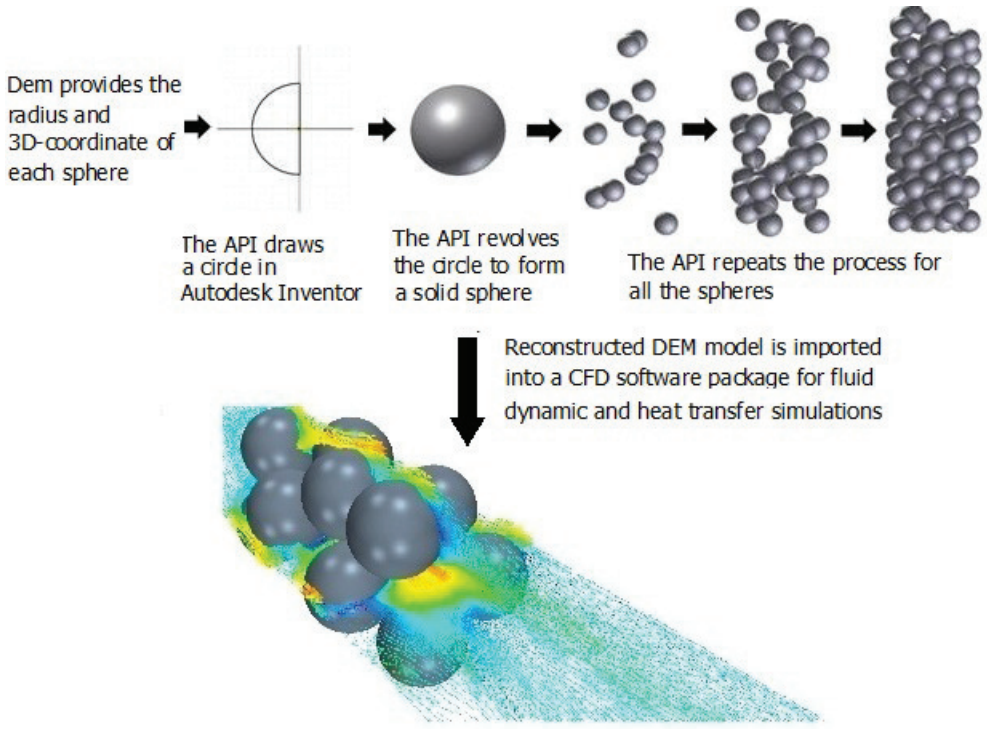

Figure 5.27: Reconstructing the developed DEM models in Autodesk Inventor

One limitation associated with the API program is the time required to perform the reconstruction, which increases exponentially as a function of the number of spheres (Figure 5.28). Large packed beds would therefore become impractical to reconstruct with this approach and alternative methods should be investigated. One possible alternative could be to create the STEP files in a more direct fashion, without the need to first reconstruct the entire bed in Autodesk Inventor and should therefore be considered for future research.

5.4.2. Estimating the axial and radial porosity profiles of packed rock beds

There are two main approaches to perform CFD simulations on the geometries of randomly packed beds, namely the realistic approach and the porous approach (Wu *et al.*, 2010). In the former approach each particle comprising the packed bed is modelled explicitly, whereas for the latter the bed is seen

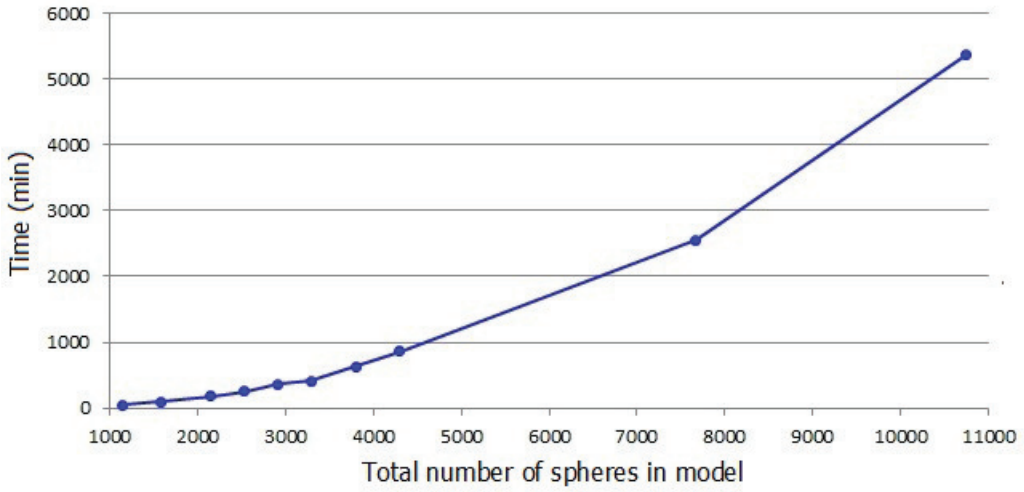

Figure 5.28: Time required to construct a bed with the API as a function of the number of spheres within the bed

as a solid matrix with an interconnected void (Nield and Bejan, 2006). There are a number of advantages and disadvantages associated with both of these methods, as discussed by Wu *et al.* (2010), but the one of particular interest is the significant increase in the number of cells and computational time required to conduct a CFD simulation with the realistic approach, as compared to that of the porous approach. This becomes more significant when large scale applications, such as the proposed thermal storage rock bed for the SUNSPOT cycle, has to be modelled. The porous approach is therefore a suitable alternative, but one area of concern is its inability to simulate the anisotropic thermal-hydraulic characteristics within the packing, such as the temperature variations around the particles, the vortices in the void spaces as well as the flow separation in these void spaces (Wu *et al.*, 2010), which could all have a significant influence on final pressure drop and heat transfer predictions.

Attempts should therefore be made to improve the porous approach in order to obtain more reliable and accurate results. According to Zavottoni *et al.* (2011), one such method is to replace the concept of a constant porosity profile, commonly implemented with the porous approach, with one resembling the actual bed more closely. Zavottoni *et al.* (2011) therefore conducted CFD simulations of a truncated cone shaped thermal storage vessel, filled with 25 m^3 of steatite rocks with an average particle diameter of 0.03 m, by using the porous approach. Three different axial porosity profiles (constant, linear and quadratic) where applied to the porous model and the resulting pressure drop and heat transfer characteristics were determined. Table 5.1 is a summary of the various pressure drop predictions, whereas Figure 5.29 is a summary of experimental and numerically obtained temperature measurements at 6 different

locations within the bed (P1 to P6).

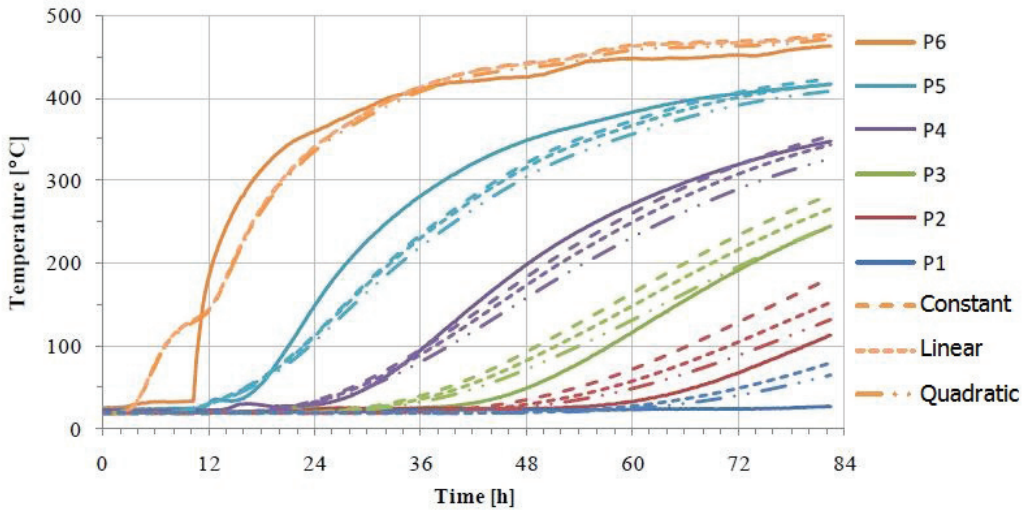

Figure 5.29: Experimental and numerical temperatures obtained for the thermal storage system investigated by Zavottoni *et al.* (2011)

Table 5.1: Experimental and numerical pressure drop values obtained for the thermal storage system investigated by Zavottoni *et al.* (2011)

Porosity profile	**CFD (Pa)**	**Computed analytically (Pa)**	**Experimental value (Pa)**
Constant	18.07	19.62	30.16
Linear	22.77	22.67	
Quadratic	26.74	25.97	

The results clearly show significant improvements for the predicted temperatures, resulting from the improved porosity profiles, especially for the quadratic case. Similar results were obtained for the pressure drop predictions, where the relative error reduced from approximately 40 % for a constant porosity profile to 10 % for the quadratic case. Even thought the errors associated with the predicted pressure drop and heat transfer characteristics could be reduced by replacing the constant axial porosity profile in the porous approach with a more realistic profile, there was still room for improvement. This was purely based on the fact that Zavottoni *et al.* (2011) implemented approximate porosity profiles (linear and quadratic) instead of the actual porosity profile of the packing. The porosity profile in the radial direction resulting from the wall effects were also not considered during the analysis. The most reasonable explanation is most likely that the actual radial and axial porosity profiles were impossible or to impractical to obtain or estimate.

This research therefore focussed on the development of a method to estimate the actual porosity profiles and can be summarized as follows (Figure 5.30):

i) The first step is to model the packed bed under investigation with DEM and then to use the necessary information to reconstruct the bed in Autodesk Inventor with the aid of the developed API, discussed in Section 5.4.1.

ii) Once the packing has been reconstructed, a separate solid model of the bed has to be created manually, within Autodesk Inventor.

iii) The two models can then be assembled over one another in order to analyse the interference, which can be extruded from the solid model in order to obtain a porous model containing all the void spaces associated with the packed bed.

iv) The porous model should then be divided into the appropriate axial and/or radial segments, such that their volumes can be estimated and finally be used together with the solid volumes of the segments, to derive the axial and/or radial porosity profiles. It should be noted that both the solid and voids volumes of the individual segments can be estimated with a build-in function in Autodesk Inventor and the porosity profiles shown in Figure 5.30 are only for visualization purposes and do not necessarily resemble the actual porosity profiles of the specified bed.

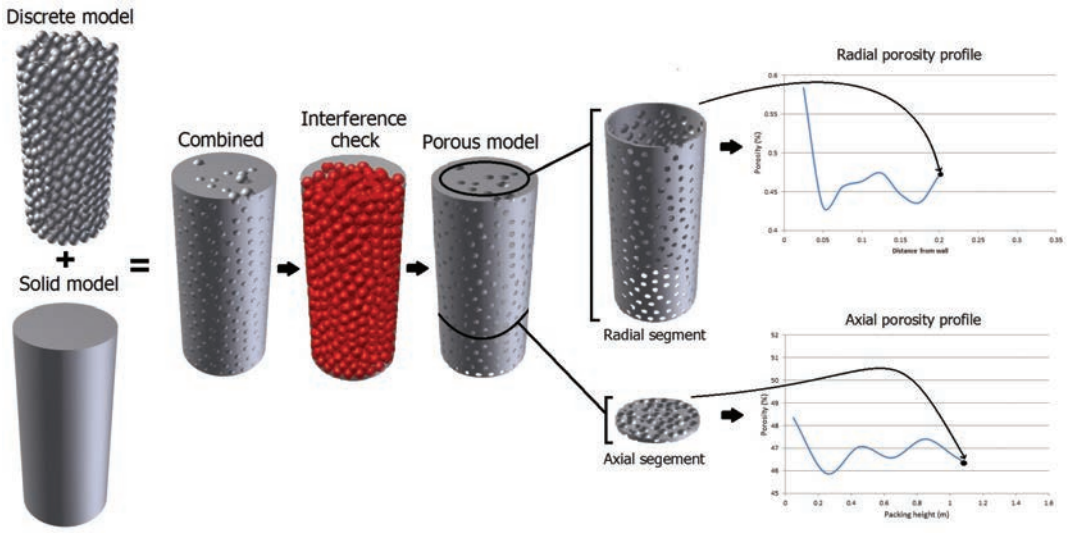

Figure 5.30: Estimating the actual porosity profiles with the aid of Autodesk Inventor

The drawback of the proposed method is the amount of manual work required to divided the porous model into the required segments, which can be very time consuming, since the accuracy of the porosity profiles depend on the size and therefore the number of segments. Future research should therefore focus on the development of a API that can perform these manual task automatically.

5.5. Complementary work for pressure drop studies

An important factor to consider when designing and constructing packed rock beds for thermal storage application is the packing direction of the rock bed. Allen *et al.* (2012) conducted various wind tunnel tests on a small scale packed bed filled with crushed rocks, where the pressure drop over the bed was measured for two different packing styles (Figure 5.31). The first corresponded to a scenario where the rocks where poured in through the lid in a cross flow direction relative to the flow direction, whereas the second resembled a co-current flow scenario where the rocks were poured in through the flow inlet. This was achieved by temporarily removing the test section from the wind tunnel, placing it onto its flow outlet and removing the mesh grid. The different packing directions clearly resulted in different friction factors, where the measured friction factor for the co-current packing was approximately 50 % higher than that obtained for the cross-flow packing.

Due to the lack of information regarding the rock orientations resulting from the different packing directions, the following assumption had to be made. During packing, the fist rock layers tend to align themselves in such a manner that their larger areas are parallel to the surface of the test section floor. The subsequent layers tend to behave in a similar fashion, but since the surfaces onto which they land become more and more irregular the parallel alignment effect becomes less visible. This could explain why the cross-flow direction resulted in a lower friction factor as compared to the co-current flow direction. In the cross-flow case the flow direction is less obstructed than the co-current case since the larger areas of the rock particles are aligned parallel to the flow direction, whereas for the co-current flow direction they are perpendicular.

This research therefore focused on using DEM to verify the assumptions made by Allen *et al.* (2012) as well as to aid the future design and construction of packed rock beds with regard to the packing direction. As a result, a method to calculate the rock orientations for the developed numerical models was developed and can be summarized as follow:

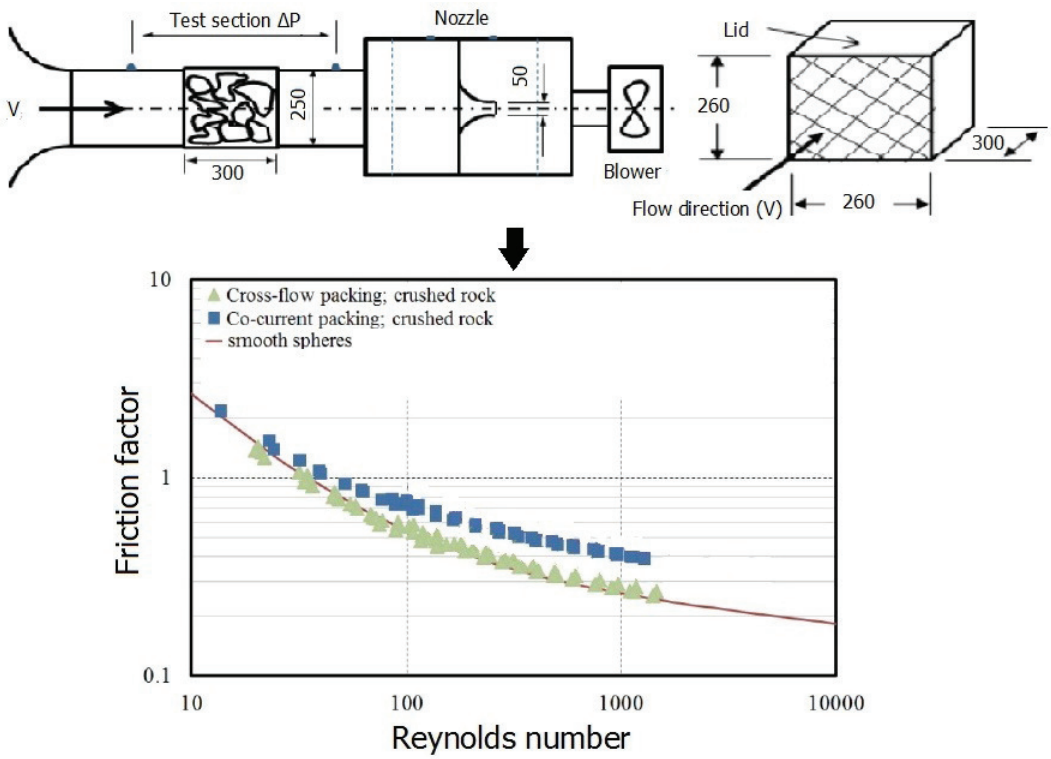

Figure 5.31: Pressure drop predictions for cross-flow and co-current flow packing directions (Allen *et al.*, 2012)

i) Identify the major orthogonal axis of each of the four clump templates implemented in the numerical models (Future research could focus on the rest of the orthogonal axes for a more detailed analysis, but for the present study it was deemed unnecessary).

ii) For each clump identify two reference spheres, lying in the direction of the major orthogonal axis (Figure 5.32).

iii) Conduct a PFC3D simulation with several identical particles by allowing them to settle onto a flat surface with their major axis parallel to the surface. Once the particles have settled, the reference spheres should be identified in order to calculate the initial relative angles associated with the simulated clumps. These angles result due to the geometric locations of the reference spheres and need to be compensated for during the final rock orientation analysis. It is important to execute this step with several particles from each clump, so that an average initial relative angle can be obtained in order to compensate for the randomness in which the clumps can settle. The initial relative angles, Θ_{ini}, can then be estimated with the aid of Equations 5.5.1 and 5.5.2, as shown in Figure 5.33.

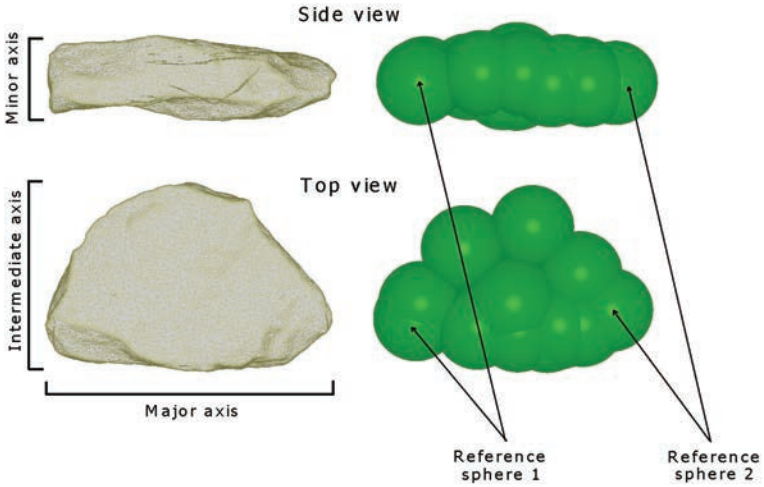

Figure 5.32: Orthogonal axes and reference spheres corresponding to the flat clump group

$$XY_{ini} = \sqrt{(x_{11} - x_{22})^2 + (y_{11} - y_{22})^2} \tag{5.5.1}$$

$$\Theta_{ini} = tan^{-1}(\frac{z_{11} - z_{22}}{XY_{ini}}) \tag{5.5.2}$$

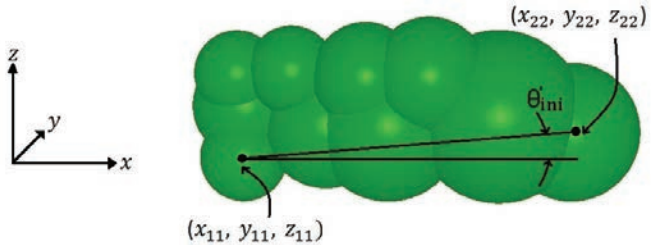

Figure 5.33: Calculating the initial reference angle corresponding to the elongated clump group

iv) With the average initial relative angles known, the actual rock orientations within a simulated rock bed can be obtained, by using Equations 5.5.3 and 5.5.4, with the parameters shown in Figure 5.34. It should be noted

that a Matlab program was developed to facilitate this process, since several hundred clumps would have to be analysed.

$$XY = \sqrt{(x_1 - x_2)^2 + (y_1 - y_2)^2} \tag{5.5.3}$$

$$\Theta = \begin{cases} tan^{-1}(\frac{z_1 - z_2}{XY}) - \Theta'_{ini} & \text{if } z_2 > z_1 \\ tan^{-1}(\frac{z_1 - z_2}{XY}) + \Theta'_{ini} & \text{if } z_2 < z_1 \end{cases} \tag{5.5.4}$$

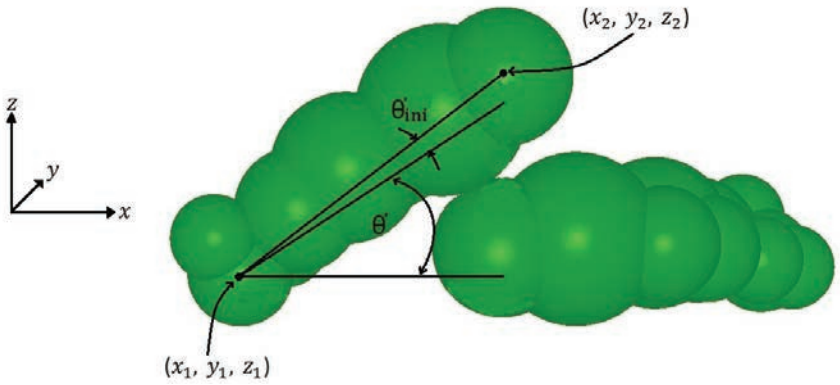

Figure 5.34: Calculating the final relative angle corresponding to the elongated clump

The rock orientations within the small scale packed bed tested by Allen *et al.* (2012) could therefore be estimated, since it consisted out of the same rock particles used for this research. The results shown in Figure 5.35 are for the local averages corresponding to 0.01 m heigh segments, measured from the bottom of the test section, as well as the global average.

It can be seen that the rocks in the first layer do indeed align relatively parallel with respect to the bottom of the test section at an average angle of approximately 7.5°. However, as expected, the alignment angle increases slightly for the second and third layers due to the irregular surface onto which the particles settled, while the alignment angle for the rest of the upper layers seemed to oscillate around an average value of 24.5°. This global average of 24.5° therefore clearly justifies the assumptions made by Allen *et al.* (2012), since the overall rock aligned was relatively parallel with respect to the bottom of the

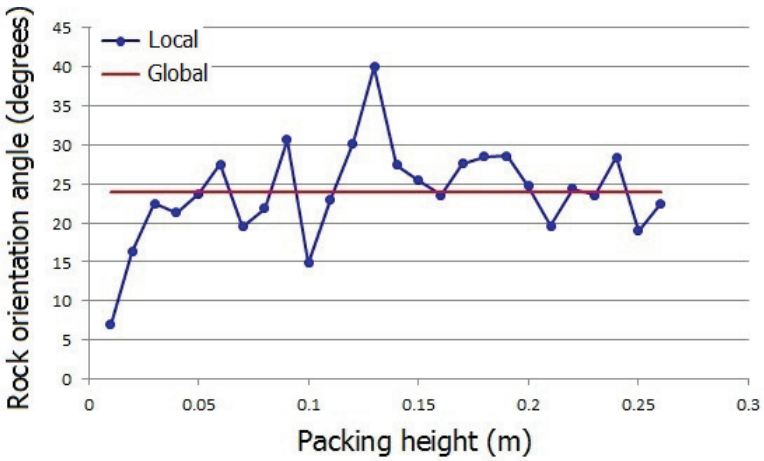

Figure 5.35: Estimated local and global rock orientations for the packed bed investigated by Allen *et al.* (2012)

test section. The fact that the DEM could provide the necessary information in order to predict the rock orientations also further emphasizes the power and flexibility of the method to be implemented as a numerical design tool for packed rock beds.

6. Conclusions

The interest in the field of solar energy power plants has grown over the past few years and numerous studies have been, and are still being done, to develop more efficient power plants. One such plant is the proposed SUNSPOT cycle which has the potential to reduce the capital cost as well as the required land space and is therefore an efficient and appropriate means of generating electricity, especially in South Africa. Research on the SUNSPOT cycle is being done by STERG and one of the primary research areas is the thermal storage unit. Previous studies have been conducted on the use of packed rock beds as the storage medium and promising results were obtained. However, further research is still required to aid in the final design, construction and operation of such thermal storage systems.

The main outcome of this study was therefore to develop numerical models resembling packed beds and then to use these models in order to investigate various aspects associated with such rock beds, which are too impractical, expensive or impossible to achieve through actual experimental work.

DEM models resembling packed rock beds were therefore developed through a series of sensitivity, calibration and verification studies. Prior to these studies, a range of experimental procedures first had to be conducted in order to obtain all the particle and bulk material properties required to perform the simulations. However, not all of the particle properties could be obtained due to the absences of sophisticated experimental equipment and tecniques, but since the particle properties would be altered during the calibration process this did not pose a problem and only initial estimates were therefore required. During the sensitivity study the experimental procedures used to obtain the bulk material properties were simulated by using a range of different material properties. As a result the relationship between the input parameters and numerical bulk responses were obtained and used to conduct a calibration process. This was achieved through an iterative process where the input parameters were varied one at a time, until all the simulated bulk responses were within acceptable limits (< 10 %) compared to the measured values. The calibrated input parameters were then verified by simulating particle discharge from a hopper and

a good correlation was obtained between the experimental and DEM results.

The DEM models were then used to study the potential of constructing self-supporting tunnels in rock beds with the aim to improve the flow uniformity of air through the bed, while minimizing the pressure drop. Two simplified tunnel construction techniques were implemented and both the horizontal and vertical directions were considered. It was observed that with the initial particle size distribution the tunnel formation and stability was too random from a practical perspective. Even when the particle size distribution was increased, the results were still too random and unpredictable. However, when the two particle size distributions were combined in a specified manner, more reliable and consistent results were obtained, with numerous stable tunnels forming.

In addition, applying a constant compression force had no consistent or even significant effect on the final results for all the different scenarios considered. nevertheless, it did show that the stable tunnels obtained by combining the two particle size distributions, remained stable even under confined compression. Furthermore, these same tunnels were also tested against disturbances from thermal cycling, by adapting the DEM models to compensate for thermal expansion effects. It was observed that even after five consecutive thermal cycles, for temperatures ranging up to 640 °C most of the tunnels remained stable. The exact tunnel dimensions achievable are, however, not known at this stage, but the results were sufficient to conclude that if the appropriate steps are taken, there is a potential to form stable self-supporting tunnels in rock beds.

To aid in additional research conducted by STERG, the packing structures of the rock beds were investigated, with specific reference to the rock orientations. This was to verify the assumption made by Allen *et al.* (2012), that the rocks tend to align in such a manner that their larger areas are relatively parallel to the bed floor. This resulted in a reduced pressure drop factor when the bed was charged trough the side, as compared to charging it through the top. A method to derive the respective rock orientations from the models was therefore devised ant the average rock orientation was found to be approximately 24.5°. Not only could the assumptions made by Allen *et al.* (2012) be verified, but the DEM models also showed their potential to aid the future design and construction of packed rock beds. Different packing methods can therefore be simulated and analysed before an actual bed is constructed.

DEM was also used to develop accurate geometric models suitable for the use in CFD studies. However, the appropriate software to convert the DEM models into a format suitable for a CFD preprocessor was not available. A program was therefore developed in Autodesk Inventor's application programming interface, which could reconstruct the DEM models in Autodesk Inventor. The reconstructed models could then simply be exported as STEP files, suitable

for most CFD preprocessors.

It can finally be concluded that the developed DEM models and procedures showed great potential to be implemented as numerical tools to aid in the design, construction and operation of rock bed thermal storage systems.

Appendices

A. Micro properties

A.1. Shape and size distribution

Fifty random rock samples were collected from the bulk material sample and subdivided into four distinct classes by means of visual inspection, similar to the approach used by Latham *et al.* (2008). The four classes (Figure A.1) can be described as follow:

- Equant, consist of particles which are close to cubical.
- Long, consist of particles which have two orthogonal axes that are relatively similar in magnitude and one that is much larger.
- Flat, consist of particles which have one orthogonal axis that is much shorter compared to the other two.
- Intermediate, consist of all the particles which did not resemble any of the above mentioned descriptions.

Figure A.1: The four classes used to describe the shape distribution

Once the different shapes were identified it was necessary to determine the size distribution of the rock samples. According to the literature this can be achieved in a number of ways. In some cases authors used simple sieving processes whereas others implemented more advance techniques by using laser light diffraction and image processing software (Vigneau *et al.*, 2000). However, due to the nature in which the particles will be reconstructed in the numerical models (see Section 4.2) it was decided to use a size distribution based on volume. The minimum and maximum volumes of the particles within each shape group would therefore be obtained and implemented as the size distribution corresponding to that specific group.

The volume of a irregular shaped particle can be obtained in one of two ways. The first is to place the particle into a measuring cylinder filled with a known volume of water and then to measure the change in volume, which resembles the volume of the particle. One should note that the time over which the experiment is conducted should be kept to a minimum such that the particle does not absorb any water, as this would lead to inaccurate measurements. The second method is to obtain a 3D scan of the particle and use the appropriate software to numerically calculate the volume. This method is rarely used since the volume displacement method is much easier and less expensive, however, it was still selected due to the following reasons:

- The volume displacement method is subject to human error especially if small individual particles (rocks) are used, since the volume of water displaced is very difficult to measure accurately.
- 3D scans of the rock particles are required to reconstruct the particles in the numerical models (see Section 4.2).
- The 3D scanner and all the post processing software were readily available.

The fifty particles mentioned above were therefore scanned with a NextEngine 3D scanner (NextEngine, 2000), which would emit a sweep of laser lines onto the surface of the rock particle. These laser lines are only visible to the scanner and once they hit the rock particle they reflect back and are recorded. These data points are then used to construct a set of non-overlapping triangles which make up a surface mesh resembling the scanned particle. A motor driven rotary table also rotates the particle to specified angular positions such that overlapping surfaces can be scanned (Figure A.2).

The 3D image processing software ScanStudio HD (NextEngine, 2000) was then used to automatically construct the final 3D images from the individual scans, after which they were imported into Rapidworks (NextEngine, 2000)

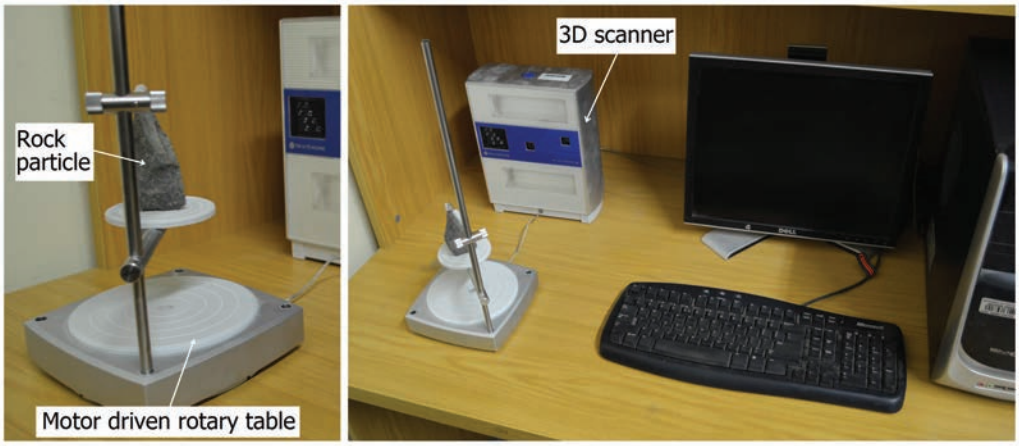

Figure A.2: NextEngine 3D scanner

where the surface geometry could be meshed with tetrahedra. The volumes of all the individual tetrahedra within the volumetric mesh of each particle could then be summed to give the total volume of the scanned particle (Latham *et al.*, 2008). Once all the particles were scanned and processed the equivalent minimum, R_{min}, and maximum, R_{max}, particle diameters (based on volume) could be identified for each group. The proposed shape and size distribution of the crushed aggregate is summarized in Table A.1

Table A.1: Proposed particle shape and size distribution of crushed aggregate under investigation

Group decription	**Number of particles**	**Percentage from overall sample**	**R_{min} (mm)**	**R_{max} (mm)**
Equant	8	0.16	10.40	16.99
Long	10	0.2	13.94	21.15
Flat	12	0.24	9.76	19.26
Intermediate	20	0.4	10.39	21.27

A.2. Particle density

In order to directly estimate the particle density, ρ_p, one is simply required to divide the mass of a particle, m_p, by its volume, V_p (Equation A.2.1) and to ensure reliability this should be repeated for several particles such that an average particle density is obtained.

$$\rho_p = \frac{m_p}{V_p} \tag{A.2.1}$$

The mass of each particle could easily be obtained with the aid of an electronic scale (accuracy of 0.1 g), whereas the volumes on the other hand were obtained from the 3D scans used for the shape and size distribution, discussed above. This approach resulted in an average particle density of 2610 kg/m^3.

A.3. Particle and boundary friction coefficients

According to Johnstone (2010), most of the research done on the particle to particle as well as the particle to boundary friction coefficients are primarily focussed on spherical or near spherical particles. The literature on measuring the friction coefficients for irregular shaped particles, such as the crushed aggregate used in this study, are therefore limited. However, based on the work done by Horn (2012) on the calibration of material properties for the use in DEM models, the particle to particle friction coefficient of a granular material can be estimated as follows:

$$u_{pp} = tan\alpha \tag{A.3.1}$$

where α is the angle of repose (see Section 3.2.3). Horn (2012) obtained an experimental angle of repose of 40°, which if it was used together with Equation A.3.1 would have resulted in a particle to particle friction coefficient of 0.84. This closely corresponded to the calibrated value of 0.86, based on shear box experiments and simulations. Nonetheless, with this approach and an angle of repose corresponding to 36° (see Section 3.2.3), the particle to particle friction coefficient for this study was estimate to be 0.73. It should be emphasized that this is only an estimation, but is still acceptable in that all the micro parameters would eventually be calibrated.

The particle to boundary friction coefficient on the other hand can also be estimated from what is known as a sliding friction tester, devised by Chung and Ooi (2006). In such a test several of the granular particles are glued to a flat base plate and then placed onto a test plate (boundary material under consideration) such that the glued particles are between the two plates. The

test plate is then slowly lifted at one end, while the opposite end is allowed to rotate until the base plate with the glued particles start to slide, at which time the inclination angle, γ, is recorded (Figure A.3). The particle to boundary friction coefficient can then finally be estimated using:

$$u_{pw} = tan\gamma \tag{A.3.2}$$

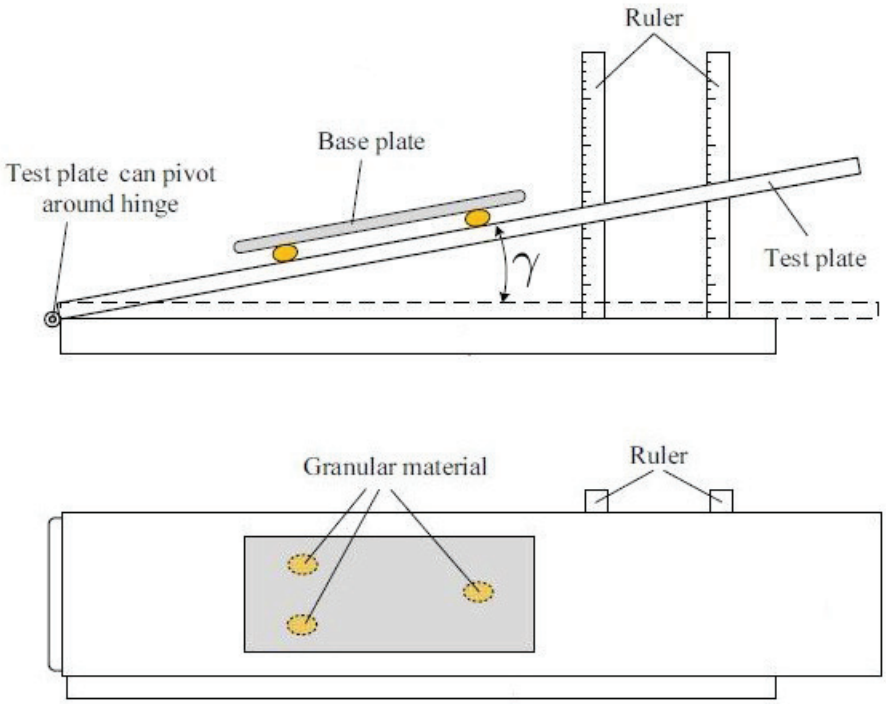

Figure A.3: Sliding friction tester (Chung and Ooi, 2006)

The particle to boundary friction coefficient can therefore be estimated for any boundary material by simply changing the test plate to resemble the required boundary material. For this study only a coated mild steel plate was used since the crushed aggregate would only come into contact with such surfaces during all the experiments. Several separate sliding friction test were conducted to obtain an average particle to boundary friction coefficient of 0.62.

A.4. Particle and boundary stiffness coefficients

The stiffness of a body is a measure of the amount of deformation in the body resulting from an externally applied load and can be determined in a number of ways. The most common method to determine the particle stiffness of a granular material sample is by using Equation A.4.1, together with the results obtained form an ASAE Standard single particle compression test with a spherical indenter (Figure A.4).

$$E = \frac{0.338 K_c^{\frac{3}{2}} \cdot P(1-\nu^2)}{\alpha_p^{\frac{3}{2}}} \cdot (\frac{4}{d})^{\frac{1}{2}} \tag{A.4.1}$$

In Equation A.4.1, E is the modulus of elasticity, describing the stiffness characteristics of the particle, K_c is a geometric constant dependent on the principal radii of curvature corresponding to the indenter and the particle, P is the load applied on the particle through the indenter, ν is the particle's Poisson's ratio, α_p is the deformation of the particle (or in other words the radii of curvature obtained with the aid of a 3D scanner) and d is the diameter of the spherical indenter (Shelef and Mohsenin, 1969).

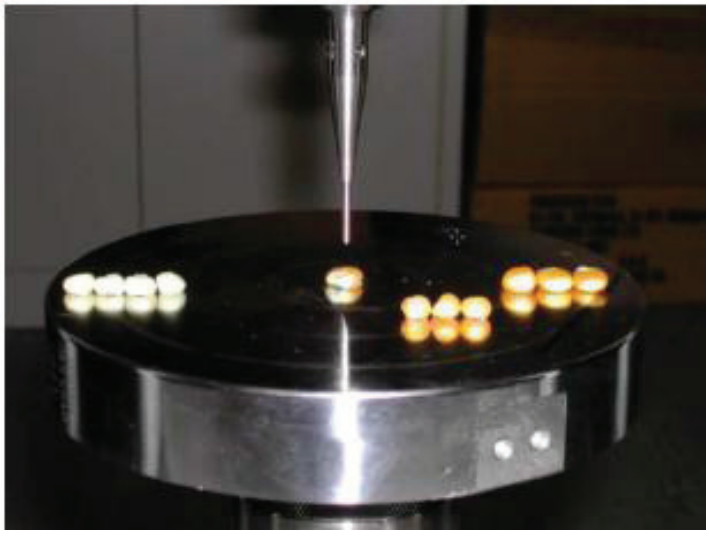

Figure A.4: Particle compression test(Chung and Ooi, 2006)

However, Chung and Ooi (2006) discovered that this approach only provides accurate results when the particles used in the test have relatively flat surfaces, but when the particles are rounder, the spherical indenter would slip and subsequently bent. Fortunately the crushed aggregate used in this study had relatively flat surfaces suitable for the indenter test, but such a test setup was not available at the time and could not be obtained due to time constraints.

It is important to always try and obtain all the relevant parameters through experiments, but whenever it is not possible one can simply estimate the unknown parameter/s, because they will eventually be calibrated. It was therefore decided to implement an initial particle stiffness of 1.75 MN/m, similar to that of the crushed aggregate used by Horn (2012). The stiffness of the mild steel (boundary material) used to construct the experimental setups on the other hand can also be obtained with the indenter test, but fortunately this information is already widely available in the literature. A stiffness of 200 GPa was therefore obtained from Quimby (2012) and implemented for all the boundaries.

A.5. Coefficient of restitution (COR)

The COR is simply a measure of the energy dissipation associated with a particle during a collision and can according to Teufelsbauer *et al.* (2009) mathematically be presented as the ratio of the impact velocity, prior to the collisions to the rebound velocity after the collision. The COR therefore quantifies the amount of energy that is lost during an impact due to the elastic deformations (Imre *et al.*, 2008) and it is closely related to the critical damping ratio (Teufelsbauer *et al.*, 2009), ξ, since:

- If $\xi = 1$ the system/particle would be critically damped resulting in a perfectly inelastic impact.
- if $\xi = 0$ the system/particle would be undamped resulting in a totally elastic impact.
- If $0 < \xi < 1$ the system/particle would be underdamped resulting in a partially elastic impact.

Information on the critical damping ratio of granular materials is very scarce when compared to that of the COR, but it is an important parameter to obtain when using PFC3D, since it is the primary means of introducing damping into the models. Fortunately, if the critical damping ratio cannot be obtained one

can estimate it through the use of Equation A.5.1 (only if $0 < \xi < 1$):

$$\xi = \frac{ln(COR)}{\sqrt{ln^2(COR) + \Pi^2}} \tag{A.5.1}$$

The COR can be obtained either from literature or by using a drop test where the particle would be dropped from a specified height onto an impact plate, during which a high speed camera records the entire process. The data from the camera can then be analysed to calculate the impact and rebound velocity. However, this only works well for relatively round particles . Nonetheless, due to the absences of a high speed camera the test could not be conducted and the literature had to be consulted. Based on the average COR calculated from a range of rock particles studied by Imre *et al.* (2008), a value of 0.85 was obtained as the COR for the crushed aggregate used in this study and the critical damping ratio was finally estimated to be 0.052 (Equation A.5.1).

B. Methods used to derive bulk responses from DEM models

All the numerical bulk responses could be calculated in the same manner as the experimental values by simply exporting the relevant information from the DEM models. However, due to the limitations of the clump logic implemented in PFC3D, as discussed in Appendix C.6, the porosity add to be calculated in an alternative way. In other words, one could not simply combine the volumes of all the spheres within each respective clump and multiply that with the density to obtain the mass, in order to finally use it together with the bulk volume to estimate the porosity. The particle density would first have to be calibrated before this approach could be used and since this was not the case, the following alternative methods were considered:

- Reconstruct the models in Autodesk Inventor and implement the same method used to calculate the actual porosity profiles, as discussed in Section 5.4.2. The only difference being that instead of dividing the bed into several small segments, the entire bed is seen as one big segment. The drawback associated with this approach is the time required to obtain the final results, but it would provide very accurate results.
- The second method was more of an approximate approach, but had the advantage that it was much less time intensive than the previous case. To understand the logic behind this method it is important to refer back to Section 4.2 on the particle generation scheme, were a set of initial spheres are first generated, after which the clumps are introduced. The initial solid volume of the model can therefore easily be obtained by simply combining the individual volumes of the initial spheres, since each clump would be scaled such that its volume would match that of the sphere it replaces. The model can then be levelled at the desired height and the deleted volume subtracted from the initial solid volume, in order to obtain the final solid volume, such that the porosity can be obtained. It was therefore only necessary to determine the deleted volume. Since the number of spheres deleted during the levelling were known, it was

assumed that the number of deleted clumps corresponded to the number of deleted spheres divided by the number of spheres used per clump. The total deleted volume could then be approximated by multiplying the volume of the average initial sphere of the particle generation scheme with the number of deleted clumps. The method was then calibrated against the Autodesk Inventor approach by slightly adjusting the radius of the initial sphere until satisfactory results were obtained. The method was finally tested on several other modelled beds and validated against the results from the Autodesk Inventor approach.

As expected, the approximate method described above was implemented to obtain the numerical porosity, simply due to the numerous simulations performed for both the sensitivity study and calibration process.

C. Results from sensitivity study

C.1. Influence of the particle to particle friction (PPF)

As shown in Figures C.2 to C.6, the PPF had an effect on all the bulk responses investigated for this research and is probably the most important micro property associated with granular materials. Even though each bulk property was affected to various degrees they all seemed to only be affected for PPF's ranging between 0 and 0.7. This saturation of bulk responses for high particle to particle friction coefficients were also observed by (Thornton, 2000) with regard to the voids ratio, the average coordination number (average number of contacts per particle) and the internal friction angle.

To better understand this response one should consider the mechanics of friction in a bit more detail. If one considers the scenario presented in Figure C.1, where an object is placed onto a frictional surface and an external force is applied in order to displace the object. The object will only come into motion if the externally applied force becomes large enough to overcome the static friction force, which is dependent on the normal force of the object as well as the static friction coefficient between the object and the surface.

The same occurs within a granular packing, where the particles will only become fully mobilized if the magnitude and direction of the contact forces are large enough to overcome the opposing frictional forces. This results in what is known as inter-particle slip and it is the driving force behind the changes seen in the bulk responses. This explains why the PPF only influences the bulk parameters over the range of 0 and 0.7. For PPF's below 0.7 the amount of inter-particle slip varied, whereas for PPF's above 0.7 there were no inter-particle slip and the bulk responses remained relatively unchanged.

Looking at the individual bulk properties more closely the following responses were observed. In the case of the porosity, an increase in the PPF resulted in an increase in the porosity and visa versa (Figure C.2). This was expected since

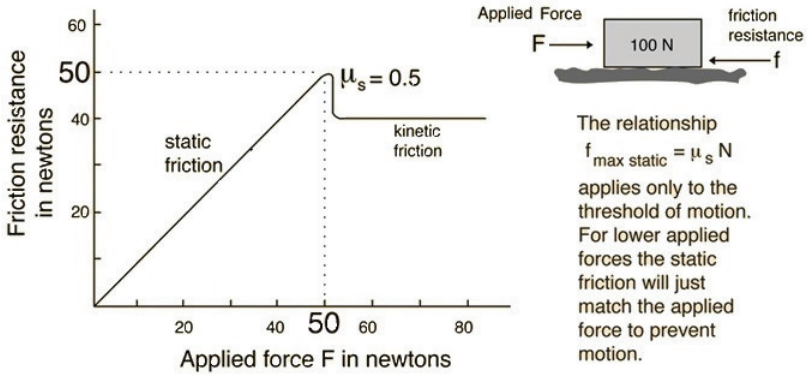

Figure C.1: The mechanics of friction (Nave, 2012)

the porosity is primarily dependent on the voids volume and as the assembly becomes more resistant to inter-particle slip, due to the increase in the PPF, a less dense packing is formed, which inevitably leads to a higher voids volume or in other words a higher porosity.

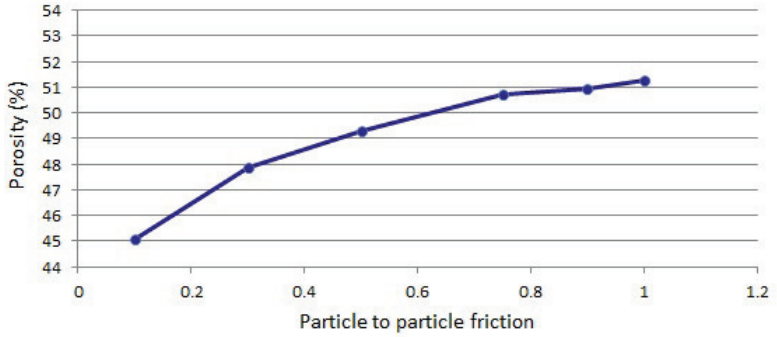

Figure C.2: The effect of the particle to particle friction on the porosity

Even though it is not that clear this interlocking effect also affected the bulk density as shown in Figure C.3, where a higher PPF resulted in fewer cases of inter-particle slip and therefore a less dense packing. The bulk volume therefore increases for an increase in the PPF and since the bulk mass remains constant the bulk density has to decrease accordingly.

It was observed that the bulk stiffness increased for an increase in the PPF, as can be seen in Figure C.4. The material therefore became more resistant to bulk deformation, which once again relates back to the amount of inter-particle slip. This effect could also be seen in the normal contact forces (Figure C.5), since the normal force on the side walls decreased slightly as the PPF increased, resulting in a slight increase in the normal force on the bottom wall. The granular material will therefore show more fluid like characteristics at low

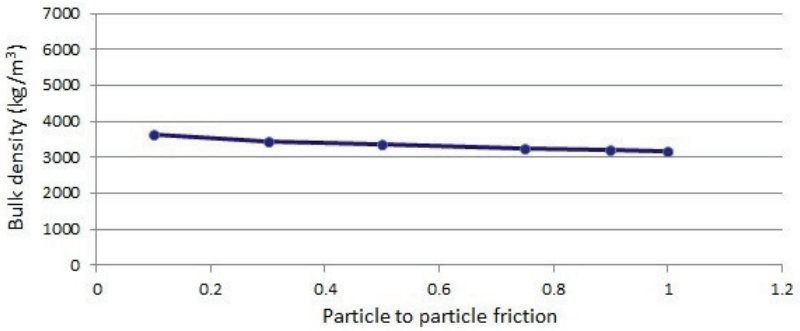

Figure C.3: The effect of the particle to particle friction on the bulk density

PPF's whereas for higher PPF's it would become more solid like. Chung and Ooi (2007) observed the same characteristics for their work on corn grains and glass beads.

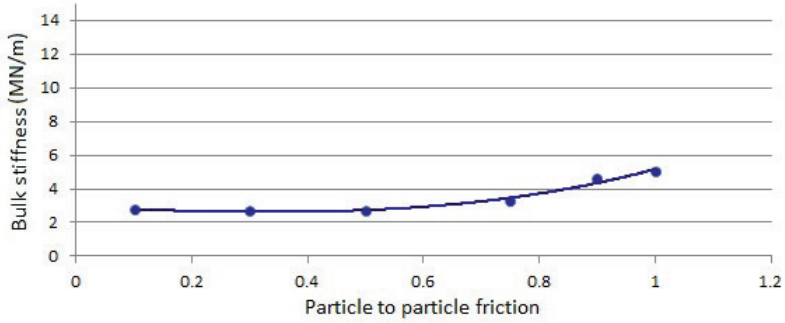

Figure C.4: The effect of the particle to particle friction on the bulk stiffness

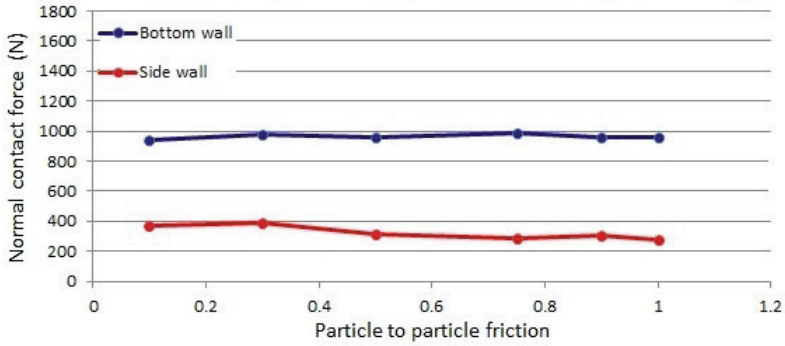

Figure C.5: The effect of the particle to particle friction on the normal contact forces on the bottom and side walls

This fluid to solid like behaviour of the granular material could also be seen in the angle of repose (Figure C.6). For low PPF's relatively small angles were

formed due to the fluid like characteristics, but for higher PPF's the material would become more stable or solid like, resulting in much steeper slopes. This was again due to the materials ability to limit the number of particles becoming fully mobilized at higher PPF's . Similar results were obtained by Muthuswamy and Tordesillas (2006).

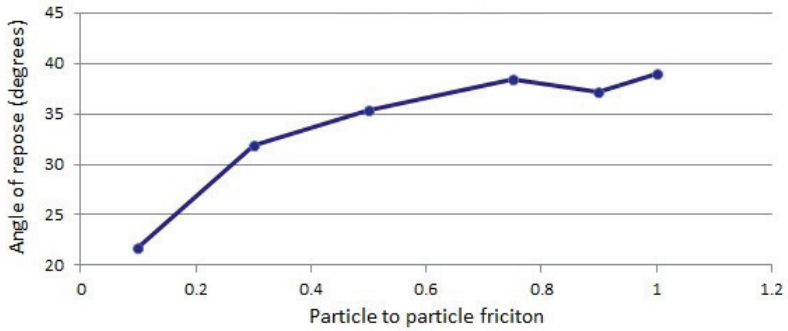

Figure C.6: The effect of the particle to particle friction on the angle of repose

C.2. Influence of the particle density

As expected, the particle density had a very strong influence on the bulk density as well as the normal contact forces on the bottom and side walls, as shown in Figures C.7 and C.8. An increase in the particle density for instance, would increase the bulk mass of the system, resulting in larger normal contact forces on the system boundaries and if the bulk volume remains constant, as was the case, the bulk density would have to increase as well (the relations were also found to be very linear).

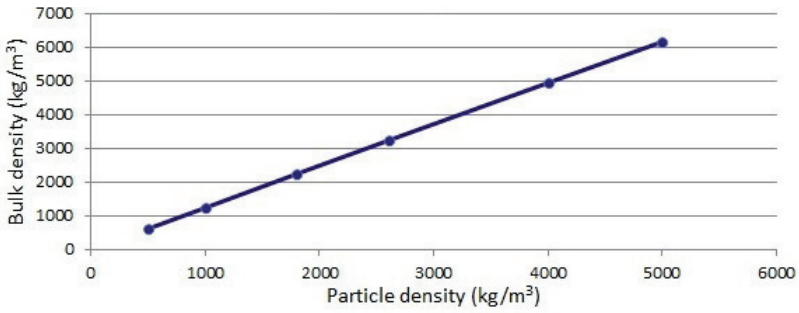

Figure C.7: The effect of the particle density on the bulk density

Even though one would expect the density to affect the porosity, Figure C.9 clearly shows that this was not the case for the conditions simulated in this

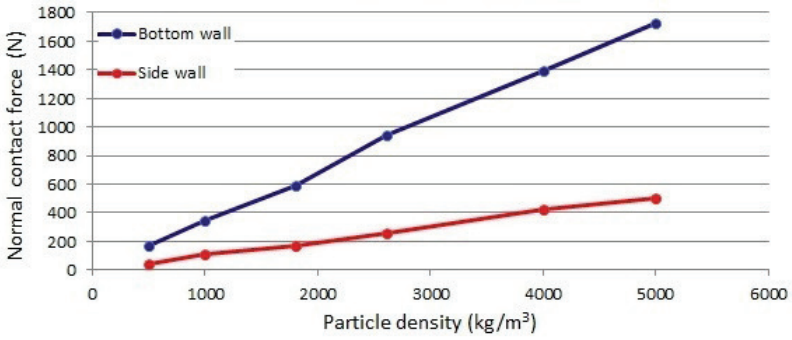

Figure C.8: The effect of the particle density on the normal contact forces on the bottom and side walls

study. One possible explanation most likely relates back to the mobilized friction discussed in Appendix C.1. At high densities it is expected that the increased contact forces within the bed would cause more particles do reach maximum mobilized friction, resulting in more inter-particle slip, which in itself causes the packing to become more dense. The reduction in the voids volume then translates directly into a reduction in the porosity. However, since this was not the case, the relatively high reference PPF used during these specific simulations, probably limited the amount of inter-particle slip. Horn (2012) obtained similar results where it was observed that the effect of the PPF and the particle density on the bulk responses investigated, were significantly higher when the two micro properties were varied simultaneously.

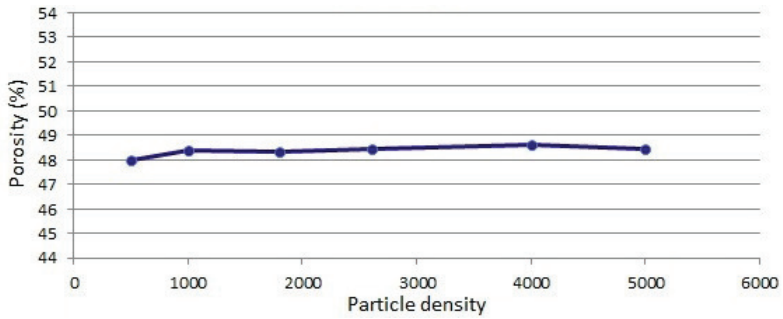

Figure C.9: The effect of the particle density on the porosity

As far as the bulk stiffness (Figure C.10) and angle of repose (Figure C.11) is concerned, changing the particle density had no significant influence and similar results were obtained by Johnstone (2010). To conclude, it was also observed that a change in the particle density had a significant effect on the computational times of the simulations. This was because the stable integration time step, is dependent on the particle density (Itasca, 2003). This meant

that for higher particle densities, larger time step are used, resulting in shorter computational times.

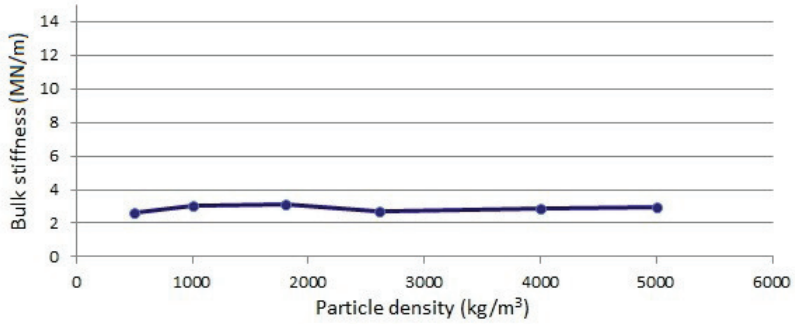

Figure C.10: The effect of the particle density on the bulk stiffness

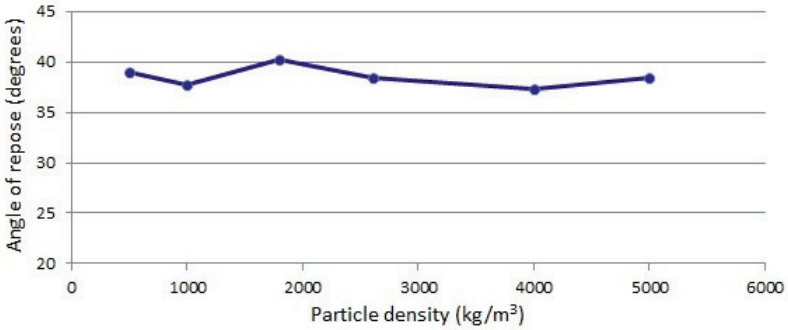

Figure C.11: The effect of the particle density on the angle of repose

C.3. Influence of the particle stiffness

The only two bulk parameters affected by the particle stiffness were the bulk stiffness and the normal contact forces on the system boundaries (Figure C.12 and C.13) and the relations were found to be very linear. The rest of the bulk responses on the other hand were not influenced by the particle stiffness (Figures C.14 to C.16).

Even though the particle stiffness had little influence on the overall bulk characteristics of the granular material it did have a significant influence on the computational times, similar to the particle density. The only difference being that as the particle stiffness increases, the size of the time step decreases, resulting in longer computational times. According to Chung and Ooi (2007), numerous researchers tend to reduce the particle stiffness in order to gain

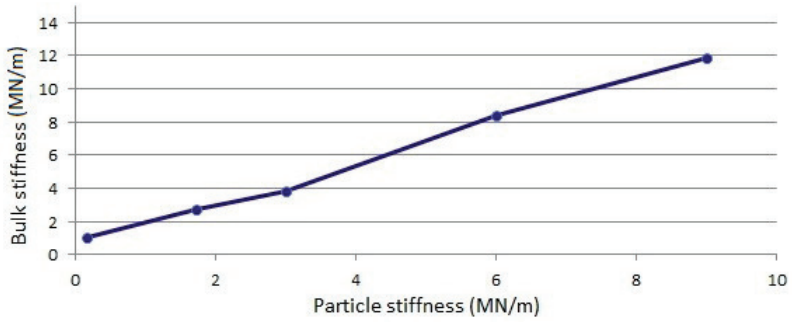

Figure C.12: The effect of the particle stiffness on the bulk stiffness

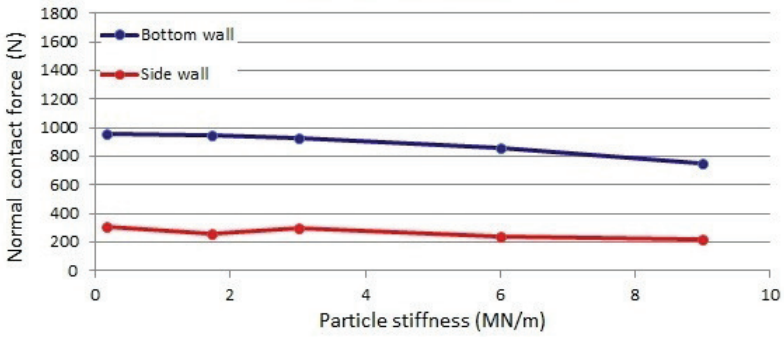

Figure C.13: The effect of the particle stiffness on the normal contact forces on the bottom and side walls

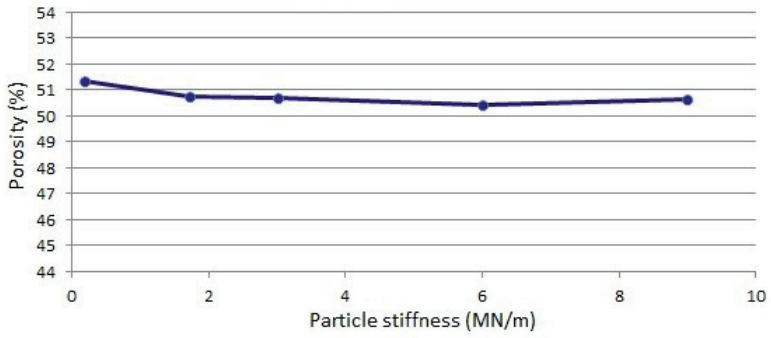

Figure C.14: The effect of the particle density on the porosity

computational advantage, while still obtaining accurate and reliable bulk responses. This approach was not implemented in this research, simply because computational resources were not a problem, however, when larger models are considers for future work it could prove to be very useful.

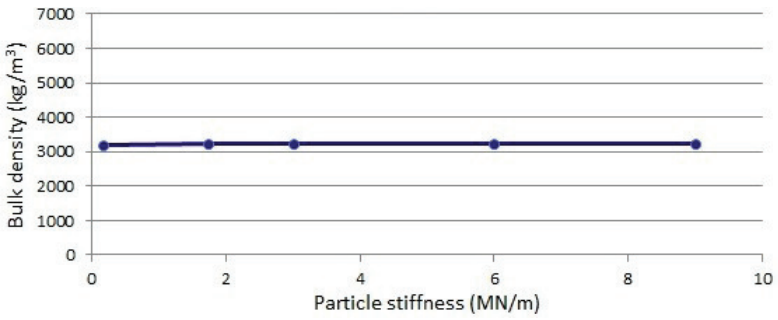

Figure C.15: The effect of the particle stiffness on the bulk density

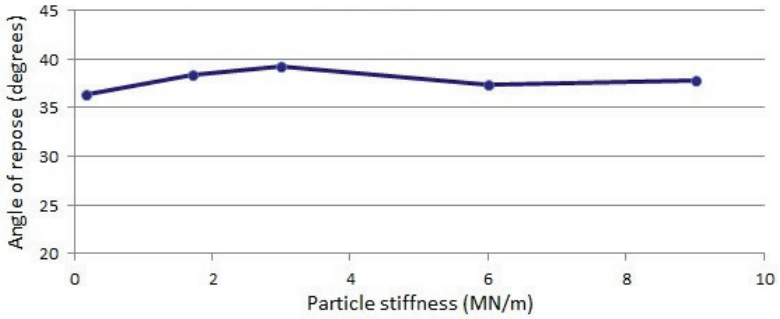

Figure C.16: The effect of the particle stiffness on the angle of repose

C.4. Influence of the particle to wall friction (PWF)

According to Johnstone (2010), the PWF is very scenario specific and is highly dependent on the degree of mobilized friction, similar to the PPF. The difference between the two is simply that for the PWF the slip is not between two particles, but rather between a particle and a wall (boundary of system). This explains why the porosity and therefore also the bulk density behaved as shown in Figures C.17 and C.18.

At high PWF's only a few particles have been fully mobilized at the boundaries resulting in a less dens packing, whereas for relatively low PWF's the particles tend to slip at the wall, resulting in a more dens packing. When compared to the PPF, the PWF does not have a significant influence on the porosity, since the size of the container was selected in such a manner that the wall effect would be eliminated to some degree. One would therefore expect the effect of the PWF compared to the PPF to become more significant, if the container size is decreased, since the ratio between the number of particle being mobilized within the packing, compared to that at at the system boundaries, will decrease.

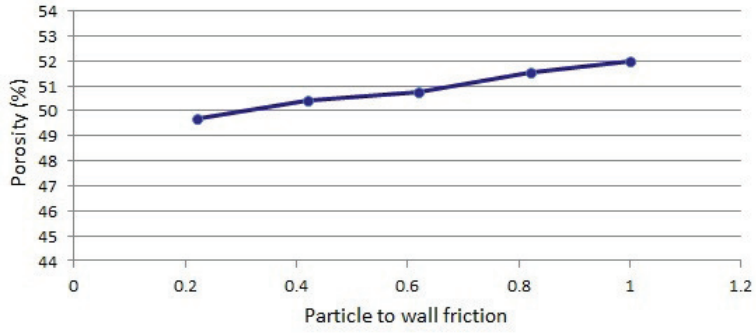

Figure C.17: The effect of the particle to wall friction on the porosity

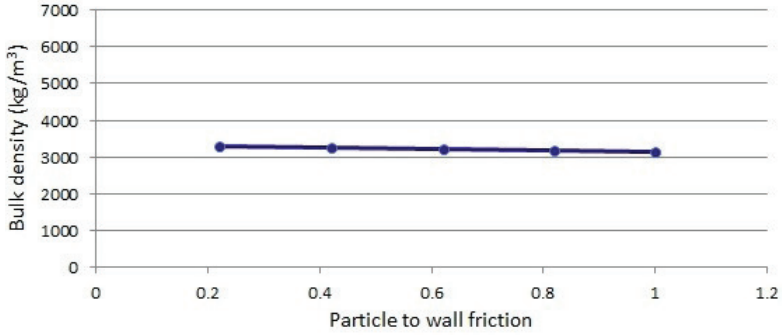

Figure C.18: The effect of the particle to wall friction on the bulk density

On the other hand, the PWF influenced the bulk stiffness characteristics of the packing in an unexpected way, as shown in Figure C.19 (taking into consideration the scale of the y axis), since it seemed as if the packing became stiffer as the PWF increased. This can be explained from the fact that as the packing is compressed the higher PWF limits the number of particles being mobilized at the walls, which then resist the downwards motion of the compression lid. The same also occurs for the decompression cycle were the expansion of the material is restrained by the increased frictional forces at the outer walls of the container. The container simulated for the confined compression test was, however, relatively large, which is why the effect of the PWF did not seem so significant. Nevertheless, care should be taken when deciding on the container sizes to be used for these types of experiments. One can refer to Johnstone (2010) for a more detailed explanation of the relationship between the PWF and the bulk characteristic of a granular material.

The effect of the PWF on the contact forces on the system boundaries also showed an interesting, but expected behaviour. As the PWF increased the normal contact force on the bottom wall decreased significantly, whereas the normal contact force on the side wall also decreased, but to a much lesser extend (Figure C.20). The reason for this decrease in the normal contact forces

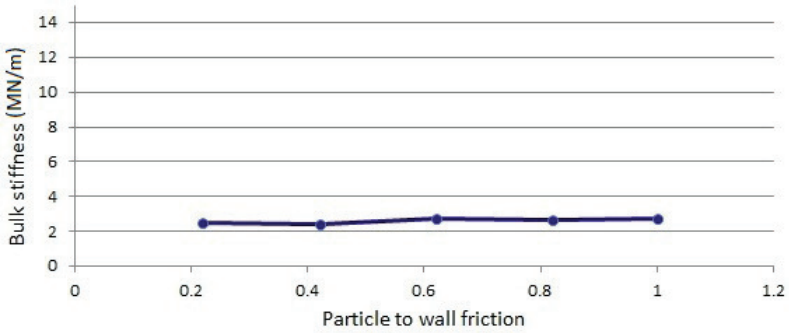

Figure C.19: The effect of the particle to wall friction on the bulk stiffness

lies in the fact that the shear contact forces actually increased, as shown in Figure C.21. The side walls were therefore able to carry more of the vertical load usually carried by the bottom wall, while the bottom wall resisted more of the outward movement, normally constraint by the side walls.

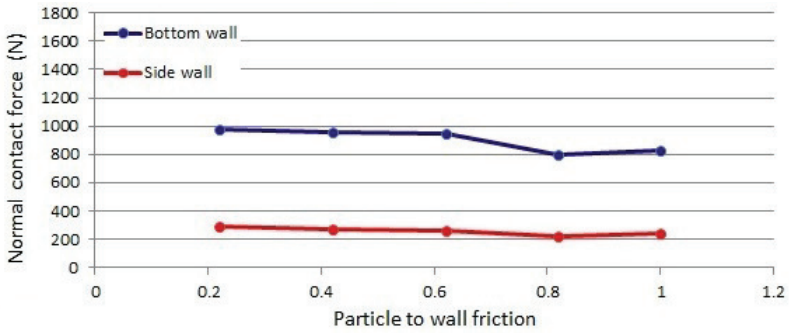

Figure C.20: The effect of the particle to wall friction on the normal contact forces on bottom and side walls

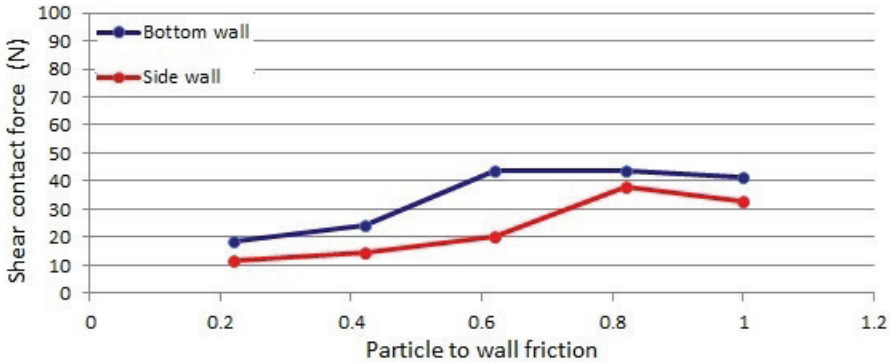

Figure C.21: The effect of the particle to wall friction on the shear contact forces on bottom and side walls

This ability of the bottom wall to be able to resist more of the outward particle sliding as the PWF increases was also made evident in the results from the angle of repose. As the PWF increased the maximum angle of repose that could be achieved also increased (Figure C.22), simply because the particles at the base of the granular pile were restraint in the lateral direction. This formed a very stable base onto which much steeper angles could be formed. The asymptotic behaviour displayed by the angle of repose as well as some of the other bulk responses, for PWF's higher than 0.6, can be attributed to the degree of mobilized friction, similar to what was observed with the PPF.

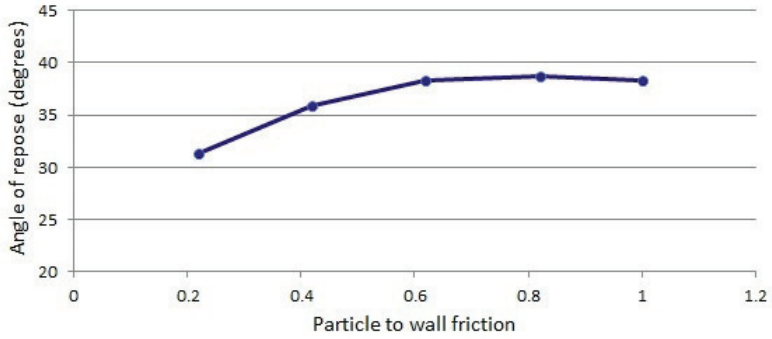

Figure C.22: The effect of the particle to wall friction on the angle of repose

C.5. Influence of the critical damping ratio (CDR)

The CDR influenced the porosity and bulk density in such a sense that the porosity increased as the damping coefficient increased (Figure C.23), while the bulk density decreased (Figure C.24). The decrease in the bulk density was simply related to the increase in the porosity, similar to all the previous cases, whereas the porosity would only change if there is a change in the voids volume (assuming the bulk volume remains constant).

One possible explanation for the change in the voids volume could be related to the time over which the particles loose their kinetic energy during settlement. For a small CDR the coefficient of restitution is high, thus the amount of kinetic energy lost during particle impacts are small. The particles within the bed would therefore be able to displace more before the packing becomes fully stabilized as compared to the case with a high damping coefficient, possibly resulting in a denser packing. On the other hand, if the CDR is high the rate of kinetic energy dissipation is also high and as a result the packing reaches steady state in a shorter period of time. The particles therefore do not have

sufficient time to form a very dense packing, since they would come to rest very quickly. This is only an assumption and should be studied in more detail during future research.

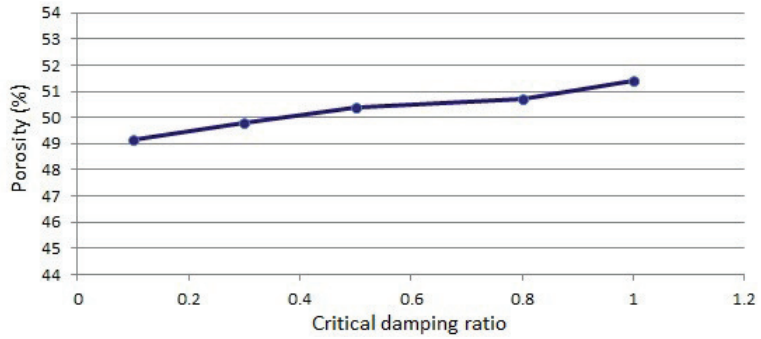

Figure C.23: The effect of the damping coefficient on the porosity

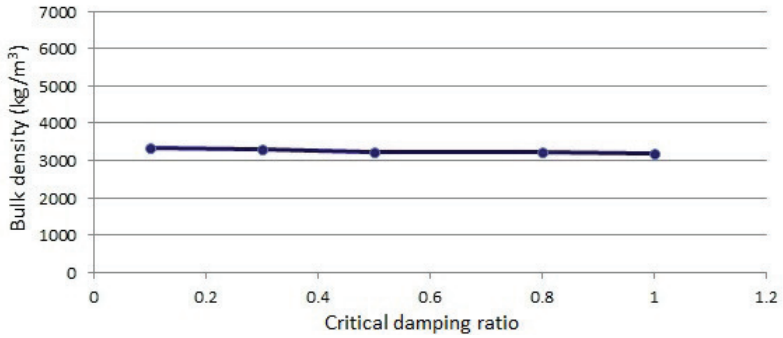

Figure C.24: The effect of the damping coefficient on the bulk density

The angle of repose displayed somewhat of a perculuar behaviour, since it was only affected for very low damping ratio's (Figure C.25). However, due to the complex nature of the CDR as well as a lack of sufficient knowledge on this particular micro property, this behaviour could not be explained and should therefore be studied in more detail during future research. On the contrary, the rest of the bulk responses were not significantly affected by the CDR (Figures C.26 to C.27).

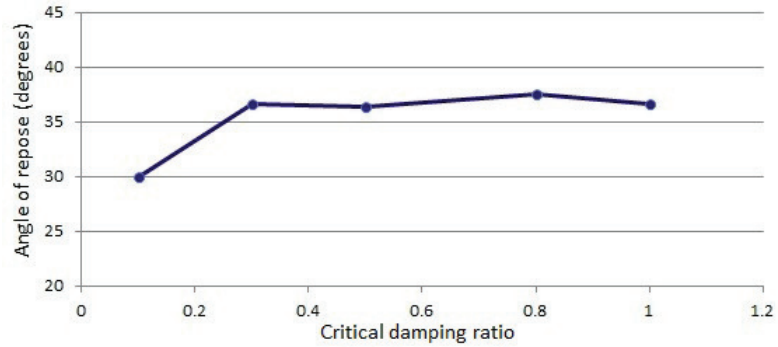

Figure C.25: The effect of the damping coefficient on the angle of repose

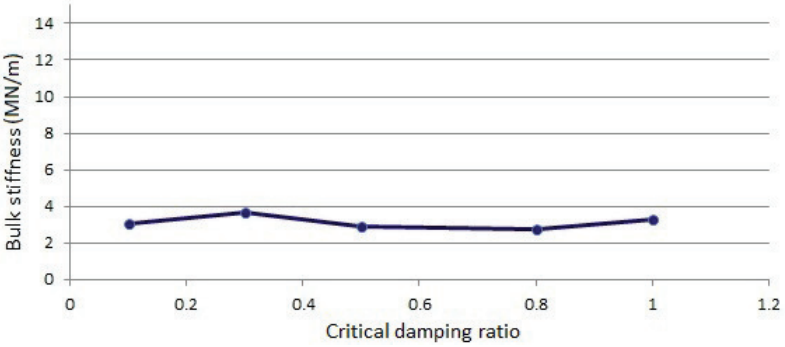

Figure C.26: The effect of the damping coefficient on the bulk stiffness

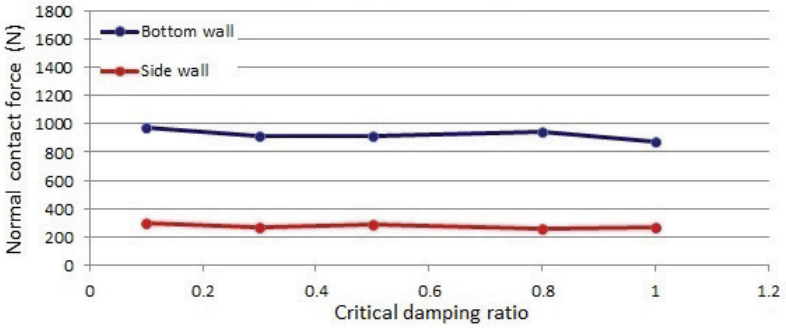

Figure C.27: The effect of the damping coefficient on the normal contact forces on bottom and side walls

C.6. Influence of the clump accuracy

Particle shape representation is a very important aspect to consider when performing DEM simulations. However, care should be taken when deciding on the degree to which the shape would be represented, since increasing the accuracy directly translates into an increase the computational time. It has been

suggested by Chung and Ooi (2006) and Hartl and Ooi (2008) that one can get away with a rather crude geometrical representation of the granular material and still obtain satisfactory results, since a very accurate representation does not necessarily lead to more accurate predictions of the bulk behavior.

This was confirmed by investigating the effect of the clump accuracy on the various bulk responses by repeating the simulations for the 3 groups shown in Figure C.28, where each group consisted out of the same 4 reference particles, but with varying degrees of accuracy (10, 35 and 75 spheres per clump).

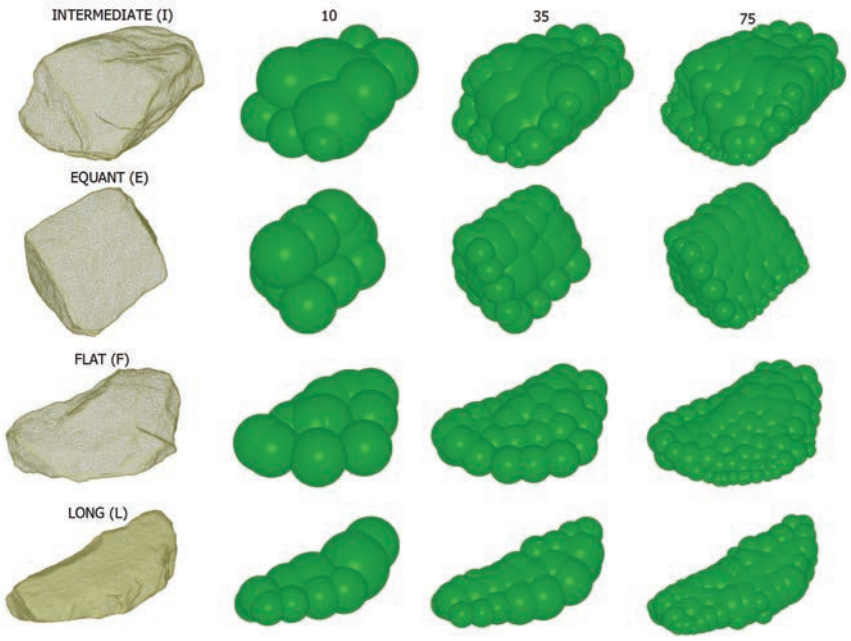

Figure C.28: Shape representation of rock particles using increasing number of spheres

The results showed that the clump accuracy had no effect on the bulk stiffness and angle of repose (Figures C.29 and C.30), but the rest of the bulk responses were indeed affected.

The effect on the porosity (Figure C.31) was expected since it depends largely on the voids volume, which in itself is dependent on the solid volume and therefore the individual volumes of all the particles. The volumes of the particle themselves on the other hand are based on the clump accuracy and as was discussed in Section 4.2, there are some volume errors associated with the reconstruction of the particles. Nevertheless, the magnitude of these errors would most likely approach an asymptotic value at some stage, after which there would be no more noticeable effect on the porosity, regardless of the clump accuracy.

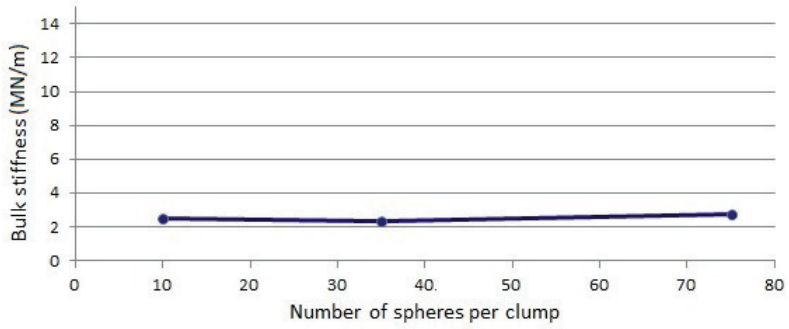

Figure C.29: The effect of the clump accuracy on the bulk stiffness

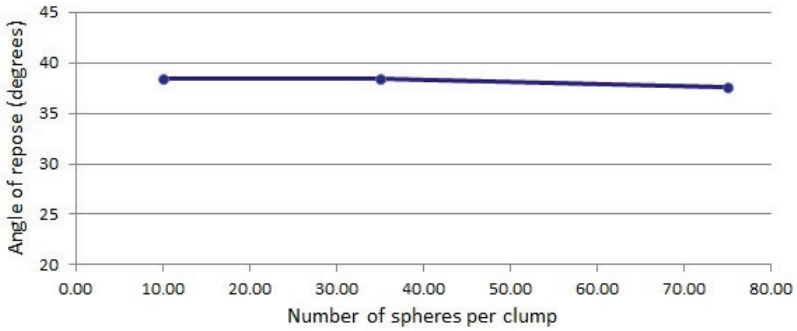

Figure C.30: The effect of the clump accuracy on the angle of repose

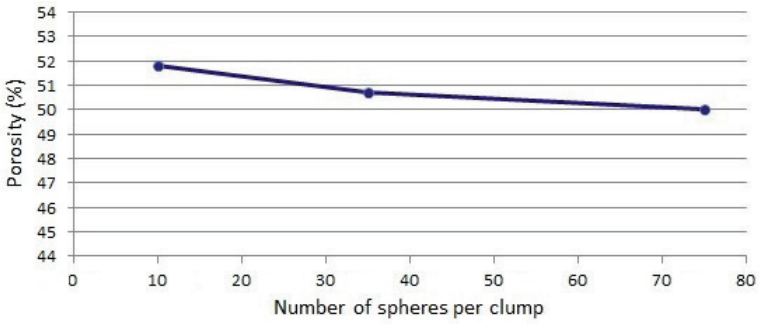

Figure C.31: The effect of the clump accuracy on the porosity

At first the significant influence of the clump accuracy on the bulk density (Figure C.32) and normal contact forces (Figure C.33) could not be explained until it was discovered that the clump logic implemented in the PFC3D code has some limitations. One of which is its inability to accurately compensate for the increased volume resulting from the numerous spherical overlaps associated with the reconstructed clumps.

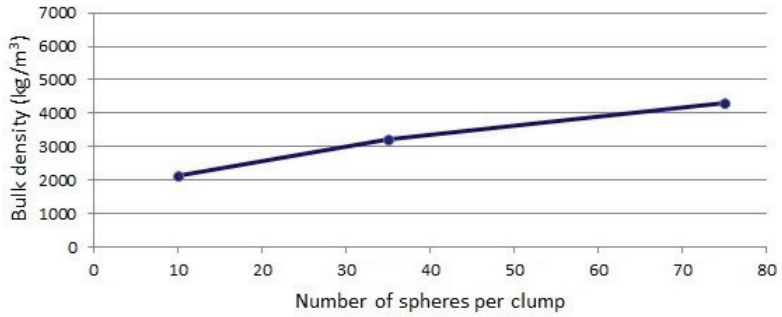

Figure C.32: The effect of the clump accuracy on the bulk density

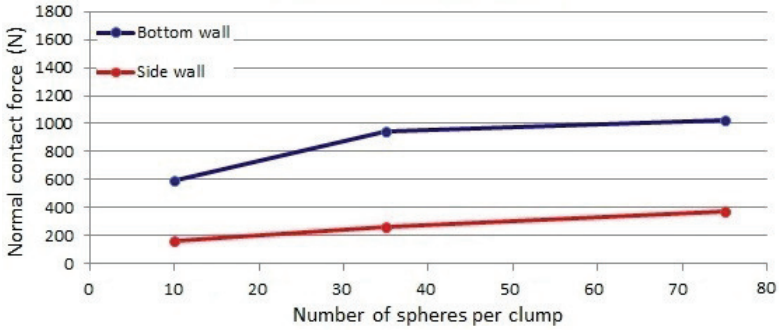

Figure C.33: The effect of the clump accuracy on the normal contact force on the bottom and side walls

The increased volume directly translates into an increased overall mass, when density is introduced, resulting in the increased bulk density and normal contact forces shown in Figures C.32 and C.33. To better understand this, one could refer to the simple scenario of two overlapping spheres. In such a case the total volume of the assembly should be the sum of the volumes of each individual sphere minus the lens volume, where the lens volume is the volume corresponding to the overlap. This is because the lens volume is already included in the total volume of one of the spheres and should therefore be subtracted from the other sphere to avoid over estimating the volume of the assembly. The PFC3D code does consider this in its calculations by removing the additional lens volumes when two spheres overlap, but not when several spherical overlaps are present. The only possible solution would therefore be to select a clump accuracy and vary the particle (sphere) density to compensate for the increased volume.

C.7. Influence of varying the shape and size distribution

Unlike the rest of the micro properties, which could be varied incrementally, the same process could not be implemented for the shape distribution. In order to achieve this one would have to use different clump templates from each representative group, however, since the number of combinations are to vast to actually quantify the influence of the shape distribution on the bulk responses investigated, it was decided to exclude it from this research. The same was also done for the size distribution.

C.8. Influence of varying multiple micro parameters simultaneously

The sensitivity study implemented investigated the effect of varying a single micro property independently, in order to illustrate each micro property's effect on the overall bulk behaviour. However, it did not investigate the effect of varying multiple parameters simultaneously, due to the time constraints associated with this research and should therefore form part of future research. This was done to some extent by Horn (2012), and the reader is referred to his works, although he used very simply clumps to represent the particles he used.

D. Tunnel experiments

In order to validate some of the observations made during the numerical procedures (specifically the ones corresponding to the tube removal process) a few simplified experimental procedures were devised, by altering the steel container used to determine the bulk properties of Section 3.2, as follow:

- For the horizontal tunnels, square sections were cut from any two opposite walls, after which two plywood boards were inserted, to act as temporary side walls (Figure D.1). The idea was that one could then simply drill the appropriate holes into the plywood walls, to support the reference tube at the desired location. Various experiments could therefore be performed and repeated for different sized tubes, by simply drilling larger holes into the plywood walls.

Figure D.1: Experimental setup used to study the formation of horizontal self-supporting tunnels in rock beds

- On the other hand, for the vertical tunnels a similar approach was implemented by modifying the bottom wall, as described above (Figure D.2). However, with this approach the reference tube would only be supported at the bottom and could therefore potentially shift sideways, as the rock particles are introduced. To prevent this, steel wires were connected to the top of the tube and the support frame and specific care was taken as the rock were poured into the container. Nevertheless, various experiments could one again be performed and repeated for different sized tubes, by simply drilling larger holes into the plywood board.

Figure D.2: Experimental setup used to study the formation of vertical self-supporting tunnels in rock beds

All the required experiments could therefore be performed by simply using the appropriate reference tubes and rock particles, as those implemented for the numerical procedures and it was assumed that the effect of the plywood boards on the final results are negiliable even though they have different sliding friction coefficients as compared to the steel walls.

In addition, an alternative study was also conducted by repeating the experiments with a applied compression force of 2500 N, to determine if the particles comprising the tunnels were affected in any way. The compression force was applied through the mechanism shown in Figure D.3, which consisted mainly out of a 2.5 m long square steel tube (known as the lever arm), two smaller 1.5 m square tubes, a compression plate and a set of free weights. The lever arm was connected to a wall such that it could pivot in the vertical direction and it was linked to the compression plate through the two 1.5 m tubes, with all the connections free to pivot in the appropriate direction such that pure vertical motion is achieved during compression. The applicable amount of free

weights, taking into consideration the weight of the compression mechanism, could then be added to the opposite end of the lever arm in order to produce the required compression force.

Finally, it should be noted that due to the time constraints associated with this research, the tunnels resulting from the excavation process could not be repeated experimentally.

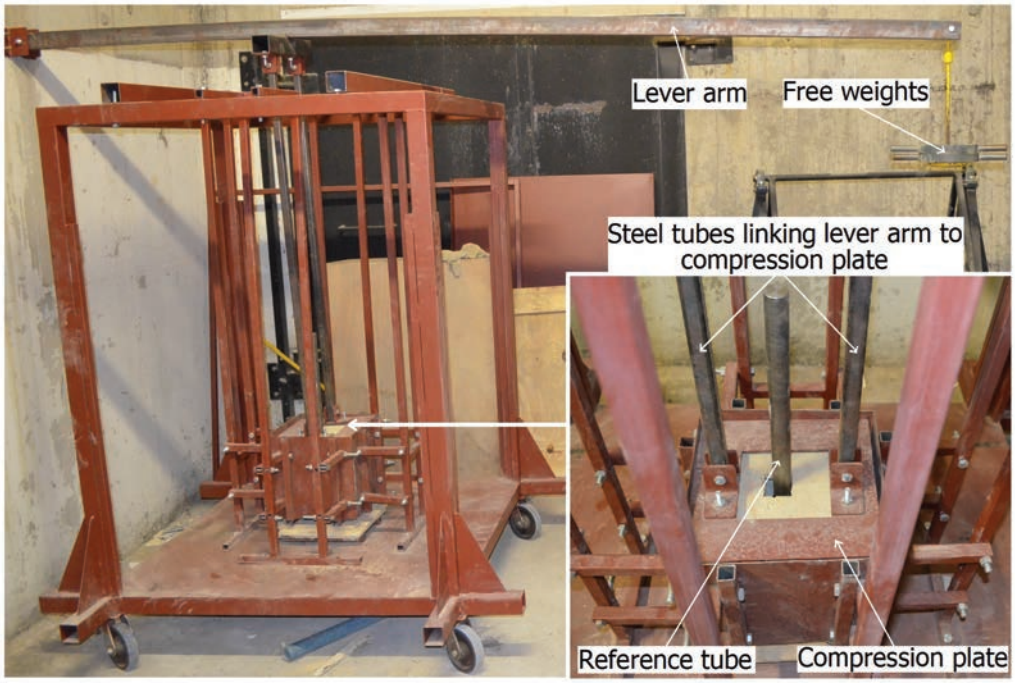

Figure D.3: Experimental setup used to study how an applied compression force affects the formation of self-supporting tunnels in rock beds

E. Additional tunnel results

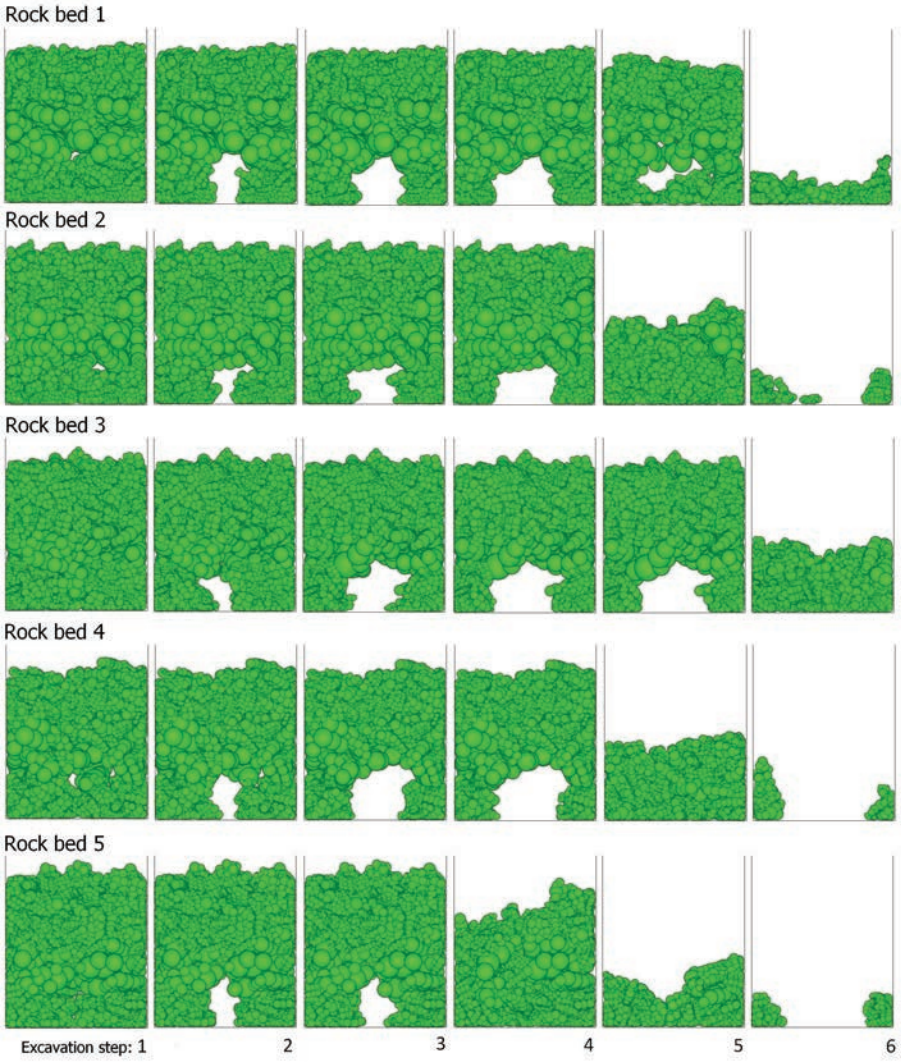

Figure E.1: Horizontal tunnels resulting from the consecutive steps of the excavation process for the proposed bed layout

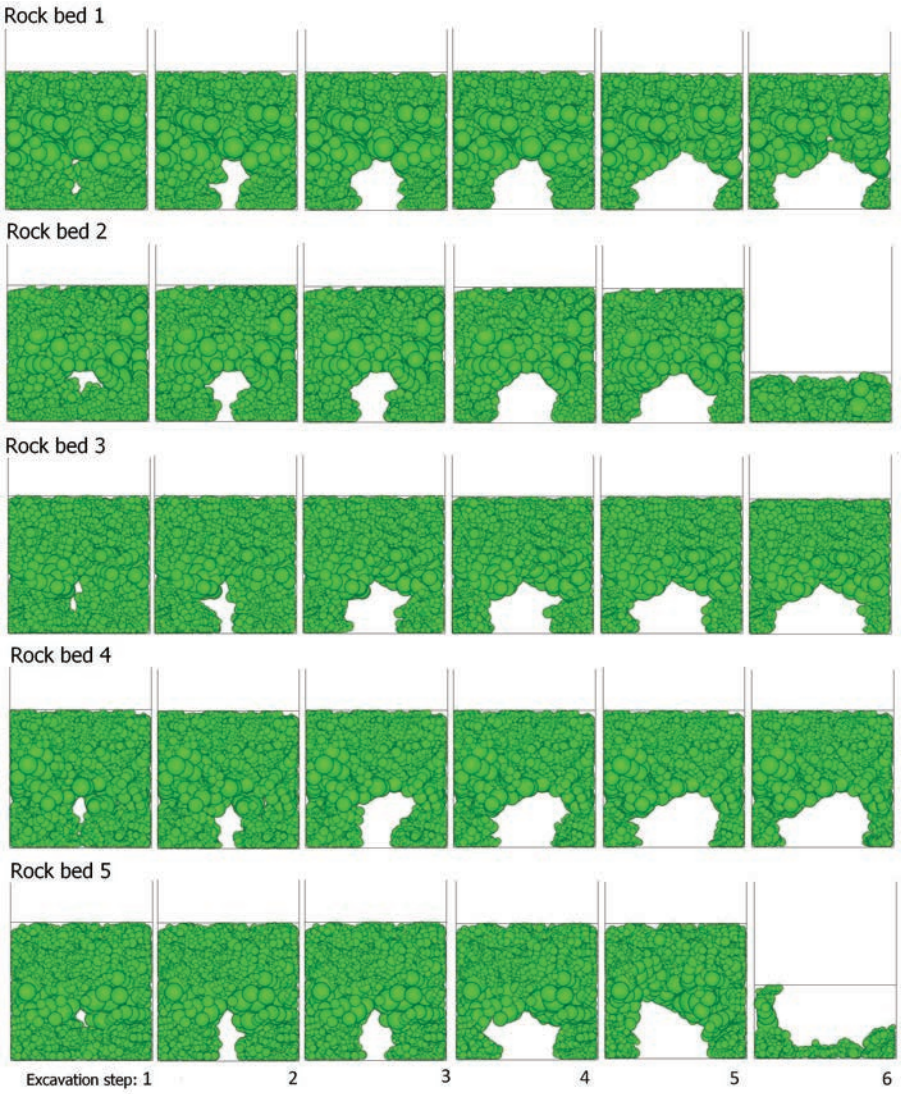

Figure E.2: Horizontal tunnels resulting from an applied compression force, during the consecutive steps of the excavation process for the proposed bed layout

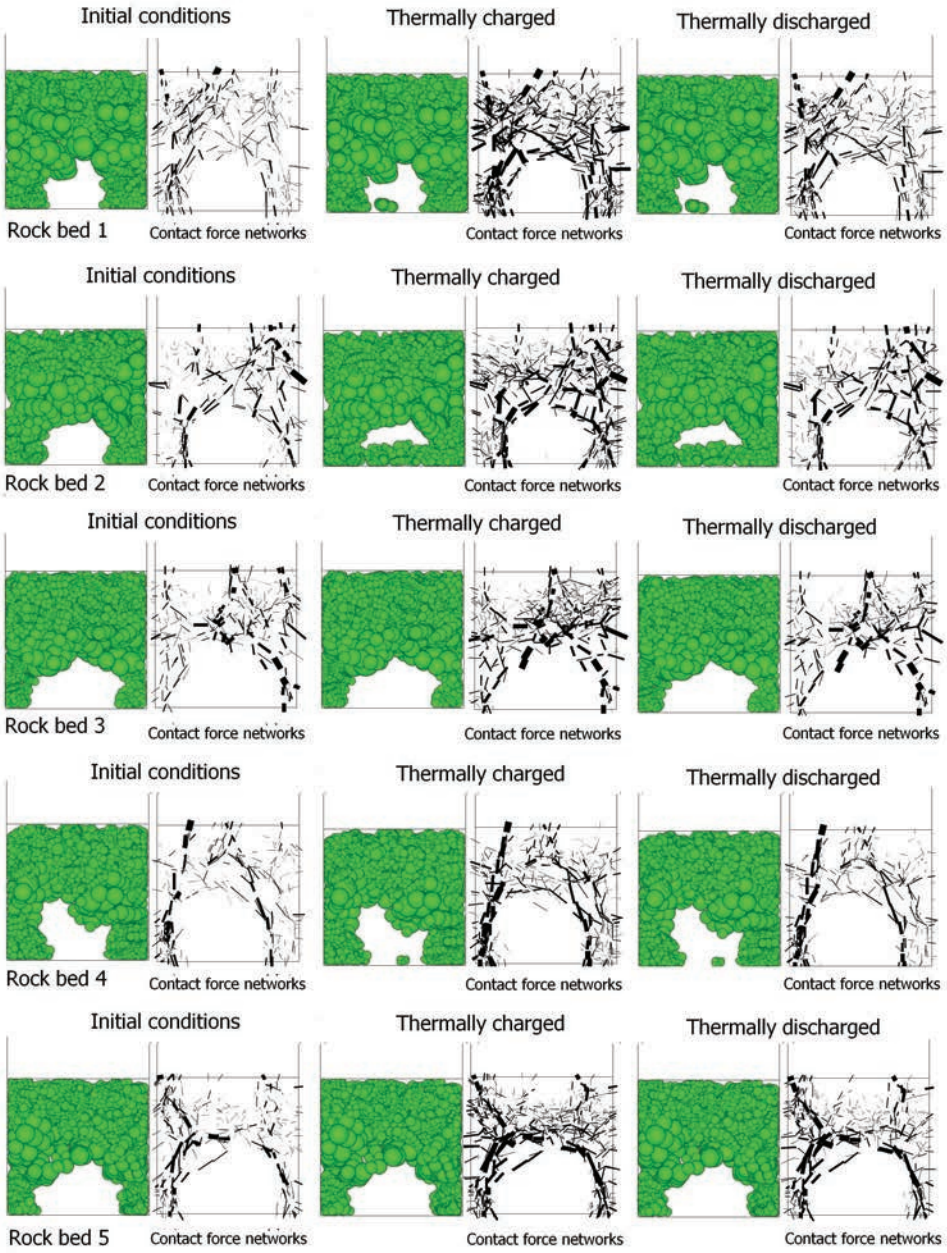

Figure E.3: The effect of thermal cycling on the stability of the horizontal tunnels for the proposed bed layout

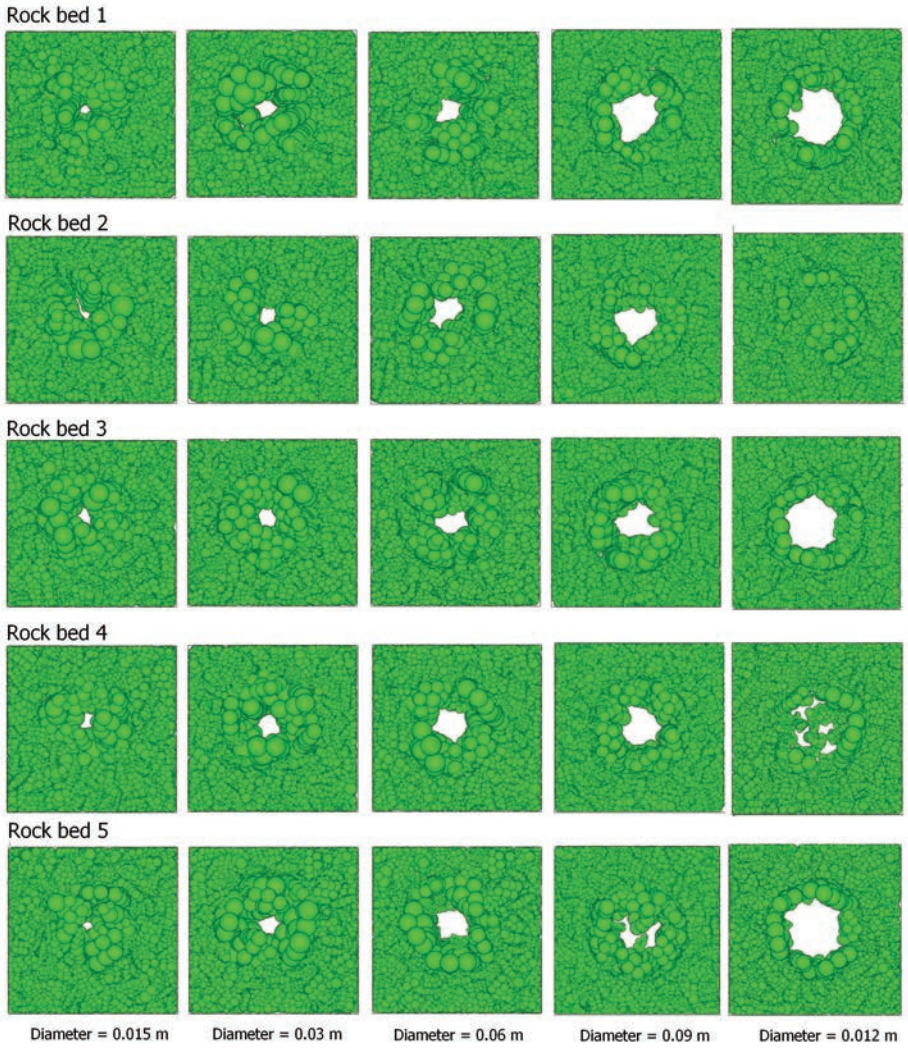

Figure E.4: Vertical tunnels resulting from the consecutive steps of the excavation process for the proposed bed layout

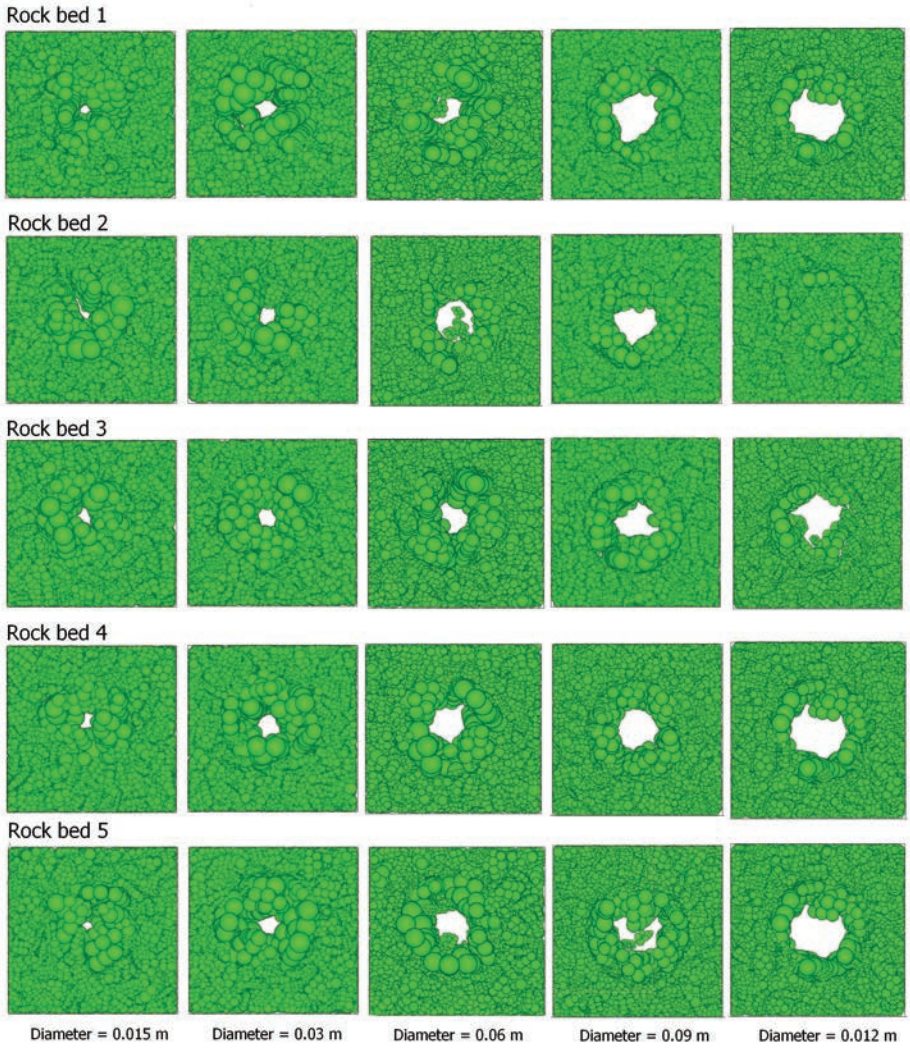

Figure E.5: Vertical tunnels resulting from an applied compression force, during the consecutive steps of the excavation process for the proposed bed layout

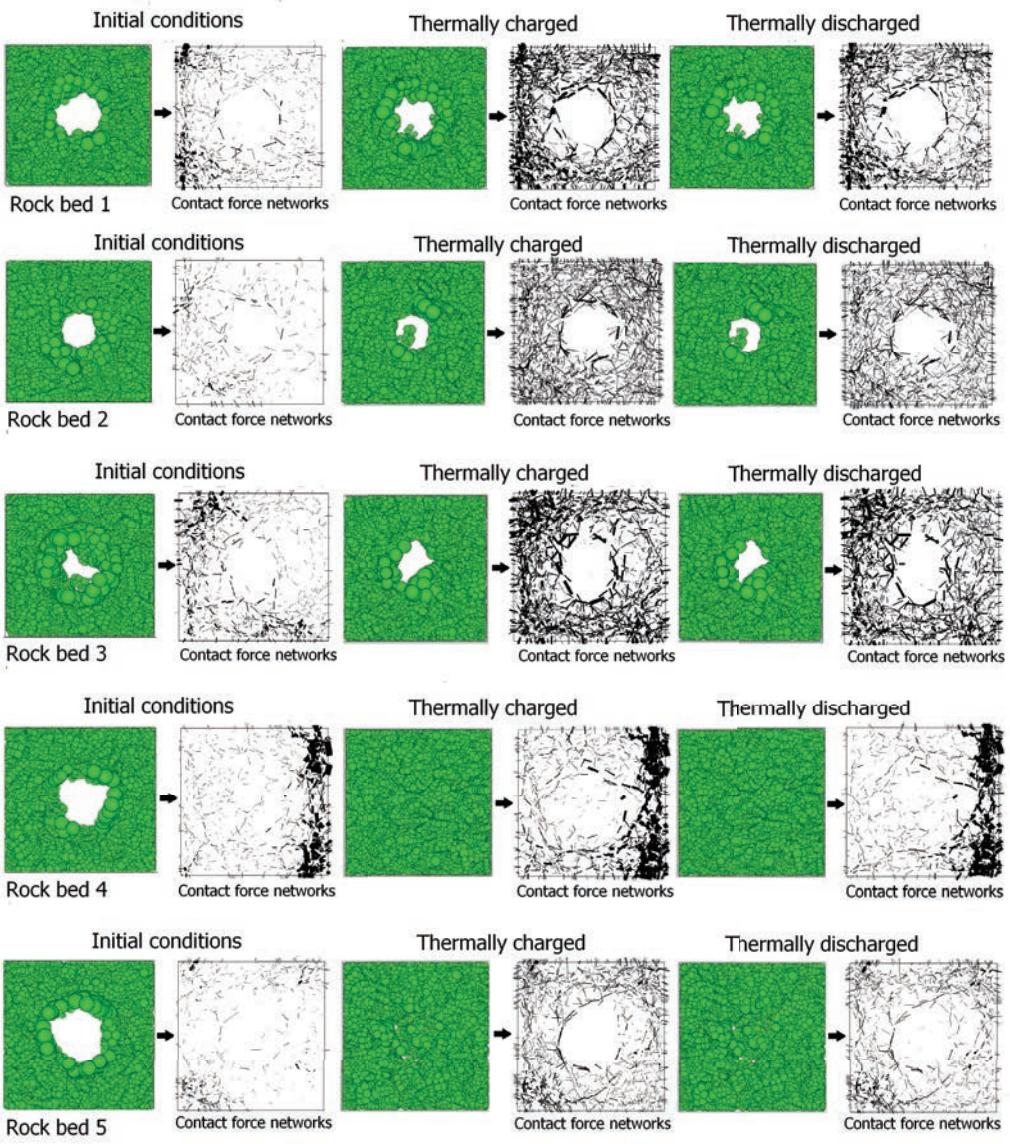

Figure E.6: The effect of thermal cycling on the stability of the vertical tunnels for the proposed bed layout

F. Thermal cycling simulations

To investigate the effect of thermally induced disturbances on the stability of the proposed tunnels, the DEM models had to be adapted to allow for the possible rearrangement of particles resulting from cyclic thermal expansion. This occurs during the charging and discharging of the rock bed, which typically correspond to the temperature profiles presented in Figure F.1.

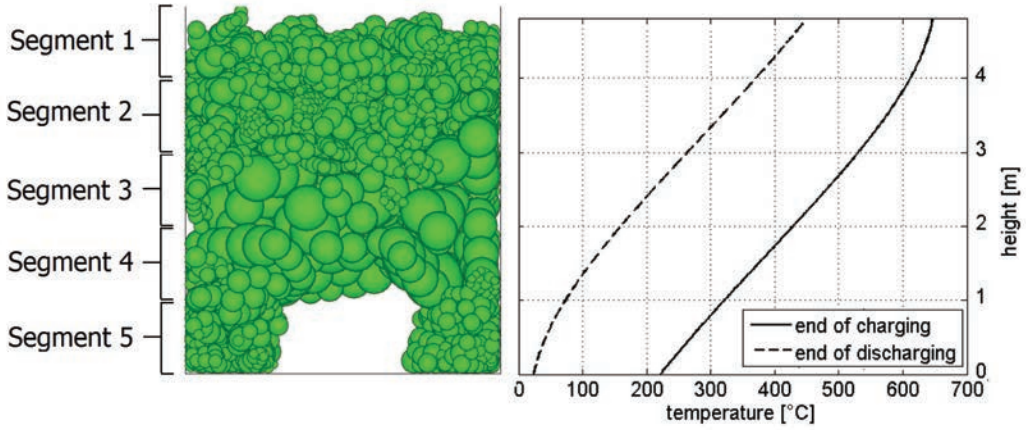

Figure F.1: Temperature profiles resulting from typical charging and discharging phases (Dreißigacker *et al.*, 2010)

To simulate these conditions with the DEM the model would first have to be divided into the appropriate number of vertical segments, after which the final temperature corresponding to each segment could be derived from the respective temperature profiles. Segment 1 for instance, would be at a temperature of approximately 640°C, after the charging phase and then decrease to a temperature of approximately 440°C, during the discharge phase. Nevertheless, once the final temperatures are known, the particles (clumps) located within each segment should be identified, such that their respective sphere radii could be altered as follows (Cutnell and Johnson, 2010)

$$\begin{aligned} V_{new} &= V_{ini}(1 + \alpha_T \triangle T) \\ \frac{4}{3}\Pi r_{new}^3 &= \frac{4}{3}\Pi r_{ini}^3(1 + \alpha_T \triangle T) \\ r_{new} &= r_{ini}(1 + \alpha_T \triangle T)^{\frac{1}{3}} \end{aligned} \tag{F.0.1}$$

where, V_{new}, is the new particle volume, V_{ini}, is the initial particle volume, r_{new}, is the new particle sphere radius, r_{ini}, is the initial particle sphere radius, $\triangle T$, is the change in temperature and, α_T, is the thermal expansion coefficient (a function of temperature). For simplicity a constant thermal expansion coefficient of 50 ($10^{-6}/°C$) was selected and corresponded to that of granite at approximately 650 °C (Fricker, 1991).

On the other hand, to resemble the charging and discharging phases more accurately the respective sphere radii were not increased in a single instance, but instead the following approach was implemented. During the charging phase the radii of the spheres corresponding to the clumps from segment 1 for example would be increased first and only after an appropriate amount of time passed, those corresponding to segment 2, would be increased. This then continues for the remainder of the segments until the entire bed is charged. In addition, the radii from each segment are also increased incrementally, until the final charging temperature is reached. During the discharge phase a similar approach would be implemented, but unlike the previous case the process starts at segment 5, moving upwards and the respective sphere radii are decreased as a results of a temperature decrease.

The models considered for this study were divided into 25 segments and 10 increments were used per segment to increase the radii to their final sizes. With the proposed method, a more accurate representation of a typical thermal cycling process was obtained. However, it should be noted that for practical reasons the simulated time between each consecutive step was fixed at 0.25 s, which meant that the models would be fully charged and discharged within only a few minutes. Since this is significantly less than the actual time required to perform the thermal cycling, the results obtained from the specified models should only be regarded as approximations.

List of References

Allen, K. (2010). *Performance characteristics of packed bed thermal energy storage for solar thermal power plants.* Master's thesis, Stellenbosch: University of Stellenbosch.

Allen, K., von Backström, T. and Kröger, D. (2012). Packed beds of rock for thermal storage. In: *Southern African Solar Energy Conference.*

Ataer, O. (2006). *Storage of thermal energy.* Elsevier.

Bai, H., Theuerkauf, J., Gillis, P. and Witt, P. (2009). A coupled DEM and CFD simulation of flow field and pressure drop in fixed bed reactor with randomly packed catalyst particles. *Industrial and Labor Relations Review Engineering Chemistry Research*, vol. 48, no. 8, pp. 4060–4074.

Chung, Y. and Ooi, J. (2006). Confined compression and rod penetration of a dense granular medium: Discrete element modelling and validation. *Modern Trends in Geomechanics*, vol. 106, pp. 223–239.

Chung, Y. and Ooi, J. (2007). Influence of discrete element model parameters on bulk behavior of a granular solid under confined compression. *Particulate Science and Technology*, vol. 26, no. 1, pp. 83–96.

Clark, D. (1999). The physics of granular materials.
Available at: `www.realizen.com/core/lit/pdfs/ncssm/mentorship_ppr.pdf`

Coetzee, C. and Els, D. (2009). Calibration of granular material parameters for dem modelling and numerical verification by blade-granular material interaction. *Journal of Terramechanics*, vol. 46, no. 1, pp. 15–26.

Coetzee, C., Els, D. and Dymond, G. (2010). Discrete element parameter calibration and the modelling of dragline bucket filling. *Journal of Terramechanics*, vol. 47, no. 1, pp. 33–44.

Cogency (2012). ASG Software.
Available at: `www.cogency.co.za`

Csizmadia, B. and Keppler, I. (2003). *Mechanics of granular materials arching theories and experiments.* Elsevier.

Cundall, P. and Strack, O. (1979). A discrete numerical model for granular assemblies. *Geotechnique*, vol. 29, no. 1, pp. 47–65.

Curry, P., Favier, J. and LaRoche, R. (2009). A systematic approach to DEM material model calibration.
Available at: `http://apps.aiche.org/proceedings/Abstract.aspxPaperID=165536`

Cutnell, J. and Johnson, K. (2010). *Introduction to Physics: International Student Version*. Wiley.

Di Felice, R. and Scapinello, C. (2010). On the interaction between a fixed bed of solid material and the confining column wall: the janssen approach. *Granular Matter*, vol. 12, no. 1, pp. 49–55.

Donze, F., Richefeu, V. and Magnier, S. (2009). Advances in discrete element method applied to soil, rock and concrete mechanics. *Electronic Journal of Geotechnical Engineering*, vol. 1, pp. 1–44.

Dreißigacker, V., Müller-Steinhagen, H. and Zunft, S. (2010). Thermo-mechanical analysis of packed beds for large-scale storage of high temperature heat. *Heat and mass transfer*, vol. 46, no. 10, pp. 1199–1207.

du Plessis, J. and Woudberg, S. (2008). Pore-scale derivation of the Ergun equation to enhance its adaptability and generalization. *Chemical Engineering Science*, vol. 63, no. 9, pp. 2576–2586.

Dymond, G. (2007). *Creation, optimization and verification of a three dimensional numerical model to simulate a dragline bucket during the digging cycle using modern DEM software*. Master's thesis, Stellenbosch: University of Stellenbosch.

Eppinger, T., Seidler, K. and Kraume, M. (2011). DEM-CFD simulations of fixed bed reactors with small tube to particle diameter ratios. *Chemical Engineering Journal*, vol. 166, no. 1, pp. 324–331.

Ergun, S. (1952). Fluid flow through packed columns. *Chem. Eng. Pro*, vol. 48, pp. 89–94.

Fortin, J., Hjiaj, M. and De Saxcle, G. (2002). An improved discrete element method based on a variational formulation of the frictional contact law. *Computers and Geotechnics*, vol. 29, no. 8, pp. 609–640.

Frenning, G. (2008). An efficient finite/discrete element procedure for simulating compression of 3D particle assemblies. *Computer Methods in Applied Mechanics and Engineering*, vol. 197, no. 49, pp. 4266–4272.

Fricker, H. (1991). High-temperature heat storage using natural rock. *Solar energy materials*, vol. 24, no. 1, pp. 249–254.

Garg, H. (1987). *Advances in Solar Energy Technology: Volume 1: Collection and Storage Systems*, vol. 1. Springer.

Garg, H., Mullick, S. and Bhargava, A. (1985). *Solar thermal energy storage*, vol. 1. Springer.

Groger, T. and Katterfeld, A. (2006). On the numerical calibration of discrete element models for the simulation of bulk solids. *Computer Aided Chemical Engineering*, vol. 21, no. A, p. 533.

Hanley, K., O'Sullivan, C., Oliveira, J., Cronin, K. and Byrne, E. (2011). Application of taguchi methods to DEM calibration of bonded agglomerates. *Powder Technology*, vol. 210, no. 3, pp. 230–240.

Hartl, J. and Ooi, J. (2008). Experiments and simulations of direct shear tests: porosity, contact friction and bulk friction. *Granular Matter*, vol. 10, no. 4, pp. 263–271.

Head, K. (1989). *Soil technicians' handbook*. Pentech Press.

Hollands, K., Sullivan, H. and Shewen, E. (1984). Flow uniformity in rock beds. *Solar energy*, vol. 32, no. 3, pp. 343–348.

Horabik, J. and Rusinek, R. (2002). Pressure ratio of cereal grains determined in a uniaxial compression test. *International agrophysics*, vol. 16, no. 1, pp. 23–28.

Horn, E. (2012). *The calibration of material properties for use in discrete element models*. Master's thesis, Stellenbosch: Stellenbosch University.

Ileleji, K. and Zhou, B. (2008). The angle of repose of bulk corn stover particles. *Powder Technology*, vol. 187, no. 2, pp. 110–118.

Imre, B., Räbsamen, S. and Springman, S. (2008). A coefficient of restitution of rock materials. *Computers and Biomedical Research Geosciences*, vol. 34, no. 4, pp. 339–350.

Itasca (2003). *Particle flow code in 3 dimensions user's guide.* Minneapolis: Mill Place.

Johnstone, M. (2010). *Calibration of DEM models for granular materials using bulk physical tests*. Ph.D. thesis, University of Edinburgh.

Kröger, D.G. (2011 April). Solar Thermal Energy Research Group. Blog. Available at: `http://blogs.sun.ac.za`

Kruggel-Emden, H., Rickelt, S., Wirtz, S. and Scherer, V. (2008). A study on the validity of the multi-sphere Discrete Element Method. *Powder Technology*, vol. 188, no. 2, pp. 153–165.

Latham, J., Munjiza, A., Garcia, X., Xiang, J. and Guises, R. (2008). Three-dimensional particle shape acquisition and use of shape library for DEM and FEM/DEM simulation. *Minerals Engineering*, vol. 21, no. 11, pp. 797–805.

Luting, S. (2011 July). Multi scale mechanics. Available at: `www.msm.ctw.utwente.nl`

Malone, K. and Xu, B. (2008). Determination of contact parameters for discrete element method simulations of granular systems. *Particuology*, vol. 6, no. 6, pp. 521–528.

Mio, H., Akashi, M., Shimosaka, A., Shirakawa, Y., Hidaka, J. and Matsuzaki, S. (2009). Speed-up of computing time for numerical analysis of particle charging process by using discrete element method. *Chemical Engineering Science*, vol. 64, no. 5, pp. 1019–1026.

Muthuswamy, M. and Tordesillas, A. (2006). How do interparticle contact friction, packing density and degree of polydispersity affect force propagation in particulate assemblies? *Journal of Statistical Mechanics: Theory and Experiment*, vol. 2006, no. 09, p. P09003.

Nave, C. (2012). Hyperphysics.
Available at: `http://hyperphysics.phy-astr.gsu.edu/hbase//frict2.html`

NextEngine (2000). 3D Scanner HD.
Available at: `www.nextengine.com`

Nield, D. and Bejan, A. (2006). *Convection in porous media*. Springer.

Ookawara, S., Kuroki, M., Street, D. and Ogawa, K. (2007). High-fidelity DEM-CFD modeling of packed bed reactors for process intensification. In: *Proceedings of European Congress of Chemical Engineering (ECCE-6), Copenhagen*.

Peters, J., Muthuswamy, M., Wibowo, J. and Tordesillas, A. (2005). Characterization of force chains in granular material. *Physical review E*, vol. 72, no. 4, p. 041307.

Quimby, T.B. (2012). A beginner's guide to structural engineering.
Available at: `http://www.bgstructuralengineering.com/`

Sagara, K. and Nakahara, N. (1991). Thermal performance and pressure drop of rock beds with large storage materials. *Solar Energy*, vol. 47, no. 3, pp. 157–163.

Sanderson, T. and Cunningham, G. (1995*a*). Packed bed thermal storage systems. *Applied energy*, vol. 51, no. 1, pp. 51–67.

Sanderson, T. and Cunningham, G. (1995*b*). Performance and efficient design of packed bed thermal storage systems. part 1. *Applied energy*, vol. 50, no. 2, pp. 119–132.

Schmidt, F. and Willmott, A. (1981). *Thermal energy storage and regeneration*, vol. 1.

Shelef, L. and Mohsenin, N. (1969). Effect of moisture content on mechanical properties of shelled corn. *Cereal Chemistry*, vol. 46, pp. 242–253.

Singh, R., Saini, R. and Saini, J. (2006). Nusselt number and friction factor correlations for packed bed solar energy storage system having large sized elements of different shapes. *Solar energy*, vol. 80, no. 7, pp. 760–771.

SRCC (2012). Solar Design Manual.
Available at: `www.solar-rating.org`

STERG (2012). Solar Thermal Energy Research Group.
Available at: `http://blogs.sun.ac.za/sterg/`

Teufelsbauer, H., Hübl, J. and Wu, W. (2009). A revision of the linear-dashpot model applied in PFC. *Contemporary Engineering Sciences*, vol. 2, pp. 165–178.

Thornton, C. (2000). Numerical simulations of deviatoric shear deformation of granular media. *Geotechnique*, vol. 50, p. 43.

Tien, H. (1996). *A literature study of the arching effects*. Ph.D. thesis, Massachusetts Institute of Technology.

Torab, H. and Beasley, D. (1987). Optimization of a packed bed thermal energy storage unit. *J. Sol. Energy Eng. (United States)*, vol. 109, no. 3, p. 1.

Vigneau, E., Loisel, C., Devaux, M. and Cantoni, P. (2000). Number of particles for the determination of size distribution from microscopic images. *Powder Technology*, vol. 107, no. 3, pp. 243–250.

Wu, C., Ferng, Y., Chieng, C. and Liu, C. (2010). Investigating the advantages and disadvantages of realistic approach and porous approach for closely packed pebbles in cfd simulation. *Nuclear Engineering and design*, vol. 240, no. 5, pp. 1151–1159.

Zavottoni, S., Barbato, M., Pedretti, A. and Zanganeh, G. (2011). CFD simulations of a pebble bed thermal energy storage system accounting for porosity variations effects. In: *SolarPACES*.

Zhanping You, P. and Dai, Q. (2006). Update on the Discrete Element Method in engineering education. *Session ENG*, vol. 206, p. 112.

Zhou, Y., Xu, B., Yu, A. and Zulli, P. (2002). An experimental and numerical study of the angle of repose of coarse spheres. *Powder technology*, vol. 125, no. 1, pp. 45–54.